To the Graduate Council:

I am submitting herewith a thesis written by Jared Michael Haynes entitled "An Investigation on the Use of Computational Fluid Dynamics to Simulate the Turbulent Phenomena from a Melt-Blowing Die." I have examined the final electronic copy of this thesis for form and content and recommend that it be accepted in partial fulfillment of the requirements for the degree of Master of Science, with a major in Aerospace Engineering.

Robert E. Bond
Major Professor

We have read this thesis
and recommend its acceptance:

Mancil W. Milligan

Rao V. Arimilli

Accepted for the Council:

Anne Mayhew
Vice Chancellor and
Dean of Graduate Studies

(Original signatures are on file with official student records.)

AN INVESTIGATION ON THE USE OF COMPUTATIONAL FLUID DYNAMICS TO SIMULATE THE TURBULENT PHENOMENA FROM A MELT-BLOWING DIE

A Thesis

Presented for the

Master of Science

Degree

The University of Tennessee, Knoxville

Jared Michael Haynes

August 2006

DEDICATION

This thesis is dedicated to my father,

Raymond E. Haynes,

for the invaluable educational opportunities he has provided me,

and to my wife,

Rebecca Christine Haynes,

for her support and patience during my undergraduate and graduate studies.

ACKNOWLEDGMENTS

I would like to thank my major professor, Dr. Robert Bond, for his tremendous help with the progress of this research, both educationally and financially. This thesis would not exist without his support. I would also like to thank my advising professor, Dr. Mancil Milligan, for his guidance through this thesis, and through my entire college career at the University of Tennessee. His reputation as a teacher is far out-matched by his abilities as one. In addition, I would like to express thanks to Dr. Rao Arimilli for the interest he has shown in my research and for his recommendation for my graduate assistantship. The professor to whom I owe my deepest gratitude is Dr. Evans Lyne. His consultation gave me the encouragement I needed to continue achieving my goals in college.

I want to give special thanks to Eric Grald from Fluent Inc. His willingness to share information made a significant impact on the progress of this study.

I am very grateful to Shawn Ericson, the former Network Administrator of the computational computer lab. His assistance with software troubleshooting was extremely valuable to my research.

Finally, I must thank all of my friends and family for their encouragement and support during this phase of my life. I especially appreciate my wife and my father. They played the most important role of helping me see the light at the end of the tunnel.

ABSTRACT

A computational investigation was performed to investigate the capabilities and limitations of the "large eddy simulation" (LES) turbulence model for a two-dimensional, melt-blowing flow field. For computational ease, the simulations were performed with incompressible and isothermal conditions. The internal flow channels of the melt-blowing die were modeled with a steady-state, k-Epsilon turbulence model. Velocity profiles were extracted from the channel exits and implemented as the inlet boundary conditions for the LES simulation of the free flow region. For parametric study, the simulations were carried out using two different jet angles of 30º and 60º. Both time-averaged and time-dependent data were recorded for analysis. Time-averaged results were used to determine if LES produced a realistic average flow field. Time-dependent results were used to determine if LES captured the large, vortex structures that dominate the motion of melt-blown fibers. Finally, a separate LES run was conducted to compare the average flow field with experimental measurements.

The time-averaged velocity plots indicated that the 60º jets produced a higher centerline velocity than the 30º jets. The 60º jets also produced more frequent velocity fluctuations than the 30º jets beyond the one-inch downstream position from the die. The LES model predicted a mean flow field that compared well with experimental data in regions close to the die (less than 2-3 cm). However, the model became much less accurate further downstream. Overall, the LES model seemed to expand the jet profile away from the centerline much sooner than shown by experiments. An animation of the

velocity field indicated that significant errors were caused by the boundary conditions. The flow field was filled with unorganized, vortex structures, which often traveled in pairs. The lack of numerical information beyond the boundaries caused these vortex pairs to separate in an unrealistic manner.

TABLE OF CONTENTS

CHAPTER PAGE

I. INTRODUCTION 1

Objectives 3

II. LITERATURE REVIEW 5

III. SOFTWARE PACKAGE 9

Boundary Conditions 10

Pressure Inlet....10

Velocity Inlet 12

Pressure Outlet....13

Wall....13

Turbulence Modeling....14

K-Epsilon 14

Large Eddy Simulation 16

IV. COMPUTATIONAL PROCEDURE 20

Preliminary LES Trial....21

LES With 2-Inch Channels 24

Channel Study....33

Solution Independence....34

2-Inch-Long Flow Domain 37

4-Inch-Long Flow Domain 40

Analysis of Results 42
Profile Optimization....43
Order of Discretization Scheme....44
Near-Wall Mesh Refinement....44
Turbulence Intensity 52
LES With Removed Channels 54
Mesh Setup....56
Pre-Run Setup 56
Execution of LES....58
Time-Averaged Data....60
Time-Dependent Data....61
CFD Comparison With Experimental Results....61
Mesh Setup....62
Pre-Run Setup 62
Execution of LES....66
V. RESULTS 67
LES With Removed Channels 67
Time-Averaged Results 67
30° Model 68
60° Model 74
Comparison Between 30° and 60° Models....79

Time-Dependent Results....79
30° Model....82
60° Model....86
Comparison Between 30° and 60° Models....94
CFD Comparison With Experimental Measurements....99
Animations of Velocity Contours....106
VI. CONCLUSIONS AND RECOMMENDATIONS....109
Conclusions....109
Recommendations....110
LIST OF REFERENCES....112
APPENDIX A: BATCH MODE COMMANDS....116
APPENDIX B: VELOCITY PROFILE DATA....118
VITA....124

LIST OF FIGURES

FIGURE		PAGE
4.1	Geometric layout of the channel exits with dimensions given to illustrate the difference between die face outset in Grald [6] and the simplified flush die face.	22
4.2	Geometric layout of the grid boundaries to contrast the truncated domain from Grald [6] with the simplified rectangular domain used for comparison. Boundaries are abbreviated as: pressure inlet (PI), pressure outlet (PO), and wall (W).	23
4.3	Comparison between the temperature contours from Grald [6] and a simulation performed with matching conditions.	25
4.4	Geometric layout of the computational grid used for the 2-inch channel run.	26
4.5	Magnified view of mesh spacing near the channel exits from the geometric configuration in Figure 4.4.	28
4.6	Centerline velocity distribution calculated by the LES model inside the 2-inch channel from Figure 4.4.	31
4.7	Comparison between the laminar, k-epsilon, and LES solutions for centerline velocity inside the 2-inch channel from Figure 4.4.	32
4.8	Geometric layout of the 2-inch-long flow domain, which was used to obtain a steady-state, k-epsilon velocity profile inside the channel.	35
4.9	Magnified view of mesh spacing near the channel exit from the geometric configuration in Figure 4.8.	36
4.10	Geometric layout of the 4-inch-long flow domain, which was used to obtain a steady-state, k-epsilon velocity profile inside the channel.	38
4.11	Velocity profiles solved with a steady-state, k-epsilon model with various initial “guesses” of the y-velocity flow field using the computational domain from Figure 4-8.	39

4.12 Velocity profiles solved with a steady-state, k-epsilon model with various initial "guesses" of the y-velocity flow field using the computational domain from Figure 4-10. 41

4.13 Velocity profile comparison of first-order and second-order discretization schemes using the steady k-epsilon model and the computational domain from Figure 4.10. 45

4.14 Magnified view of the refined mesh spacing near the channel exit from the geometric configuration in Figure 4.10. 50

4.15 Velocity profile comparison between the original and refined grid using standard wall treatment (SWT). 51

4.16 Velocity profile comparison between the enhanced wall treatment (EWT) and the standard wall treatment (SWT), using the refined grid. 53

4.17 Velocity profile comparison with different values of inlet turbulence intensity *I*, using enhanced wall treatment and a refined grid. 55

4.18 Magnified view of the mesh spacing near the channel exits of a new geometric configuration. The channels, which are oriented at with a 30 included angle, were removed to accommodate the new velocity inlets (VI). 57

4.19 Geometric layout of the computational domain with point monitors represented by circles with cross hairs and line monitors represented by dashed lines. 59

4.20 Geometric layout of the melt-blown die used in laboratory experiments at the University of Tennessee. 63

4.21 Magnified view of the mesh spacing near the channel exits for the geometric configuration in Figure 4.20. 64

4.22 Geometric layout of the computational domain used to simulate the flow field generated by the die geometry in Figure 4.20. 65

5.1 Time-averaged centerline velocity with a 30° included angle between channels. 69

5.2 Time-averaged velocity profiles located at different positions downstream of the channel exit planes, which are oriented with a 30° included angle. 70

5.3 Contours of time-averaged velocity magnitude with a 30° included angle between channels. Each contour line represents a change in velocity of 3.4 m/s. 72

5.4 Magnified contours of time-averaged velocity magnitude with a 30° included angle between channels. Each contour line represents a change in velocity of 1.4 m/s. 73

5.5 Time-averaged centerline velocity with a 60° included angle between channels. 75

5.6 Time-averaged velocity profiles located at different positions downstream of the channel exit planes, which are oriented with a 60° included angle. 76

5.7 Contours of time-averaged velocity magnitude with a 60° included angle between channels. Each contour line represents a change in velocity of 3.4 m/s. 77

5.8 Magnified contours of time-averaged velocity magnitude with a 60° included angle between channels. Each contour line represents a change in velocity of 1.2 m/s. 78

5.9 Comparison of time-averaged centerline velocity for the 30° and 60° models. 80

5.10 Comparison of time-averaged velocity profiles at 2.54 cm (1") downstream of the channel exits for the 30° and 60° models. 81

5.11 Time-dependent velocity at 2.54 cm (1") downstream of the channel exits for the 30° model, shown with 0.2 total seconds of run time. 83

5.12 Time-dependent velocity at 5.08 cm (2") downstream of the channel exits for the 30° model, shown with 0.2 total seconds of run time. 84

5.13 Time-dependent velocity at 7.62 cm (3") downstream of the channel exits for the 30° model, shown with 0.2 total seconds of run time. 85

5.14 Time-dependent velocity at 2.54 cm (1") downstream of the channel exits for the 30° model, shown with 0.05 total seconds of run time. 87

5.15 Contour of instantaneous velocity after a run time of 1.01 seconds for the 30° model. 88

5.16 Time-dependent velocity at 2.54 cm (1") downstream of the channel exits for the 60° model, shown with 0.2 total seconds of run time. 89

5.17 Time-dependent velocity at 5.08 cm (2") downstream of the channel exits for the 60° model, shown with 0.2 total seconds of run time. 91

5.18 Time-dependent velocity at 7.62 cm (3") downstream of the channel exits for the 60° model, shown with 0.2 total seconds of run time. 92

5.19 Time-dependent velocity at 2.54 cm (1") downstream of the channel exits for the 60° model, shown with 0.05 total seconds of run time. 93

5.20 Time-dependent relative intensity at 2.54 cm (1") downstream of the channel exits for the 30° model, shown with 0.2 total seconds of run time. 96

5.21 Time-dependent relative intensity at 2.54 cm (1") downstream of the channel exits for the 60° model, shown with 0.2 total seconds of run time. 97

5.22 Comparison of centerline velocity between a time-averaged LES solution and experimental measurements. Matching velocities are located at 1.78 cm downstream of the channel exits 100

5.23 Comparison of centerline velocity between a time-averaged LES solution and experimental measurements. Velocities were non-dimensionalized with respect to the matching value of 58 m/s located at 1.78 cm in Figure 5.18. 101

5.24 Comparison of velocity profiles in the 0.254 cm (0.1") downstream position, between a time-averaged LES solution and experimental measurements. Velocities were normalized with respect to their maximum values. 102

5.25 Comparison of velocity profiles in the 1.27 cm (0.5") downstream position, between a time-averaged LES solution and experimental measurements. Velocities were normalized with respect to their maximum values. 103

5.26 Comparison of velocity profiles in the 2.54 cm (1") downstream position, between a time-averaged LES solution and experimental measurements. Velocities were normalized with respect to their maximum values. 104

5.27 Comparison of velocity profiles in the 5.08 cm (2") downstream position, between a time-averaged LES solution and experimental measurements. Velocities were normalized with respect to their maximum values. 105

5.28 Schematic diagram of the flow domain illustrating the undesired impact that the boundary conditions have on vortex pairs, as observed in animations of the velocity contours.....108

LIST OF SYMBOLS AND ABBREVIATIONS

English Symbols

A	cross-sectional area of boundary
CFD	computational fluid dynamics
$C_{1\varepsilon}$	first empirical constant for ε equation
$C_{2\varepsilon}$	second empirical constant for ε equation
C_s	Smagorinsky constant
C_μ	empirical constant for μ_t equation
DNS	direct numerical simulation
D	computational domain
D_h	hydraulic diameter
d	distance between a node and the nearest wall
de	width of the die wall between jets
dg	gap width between channel walls
dl	length of the channel
ds	outset distance of die face
E	empirical constant from logarithmic law for mean velocity
f	frequency of velocity fluctuations
G	filtering function for large eddy simulation
G_k	generation of turbulence kinetic energy

I	turbulence intensity
k	turbulence kinetic energy
LES	large eddy simulation
L_s	mixing length
ℓ_μ	blending function from boundary layer equations
M	Mach number
PI	pressure inlet
PO	pressure outlet
p_o	stagnation pressure
p_{op}	operating pressure
p_s	static pressure
RANS	Reynolds-Averaged Navier-Stokes
R	specific gas constant
Re_{D_h}	Reynolds number based on hydraulic diameter
Re_t	turbulent Reynolds number
RI	relative intensity of velocity fluctuations
SGS	sub-grid scale
S_{ij}	rate-of-strain tensor for resolved scales of motion
S_k	user-defined source term of turbulence kinetic energy
S_ε	user-defined source term of turbulence dissipation rate

St	Strouhal number
t	time
T_o	stagnation temperature
T_s	static temperature
U	fluid velocity from law-of-the-wall
u	velocity magnitude
u_x, u_i	x-component of velocity vector
u_y, u_j	y-component of velocity vector
V	computational volume
V_i	initialized "guess" of y-velocity flow field
W	wall
x	cartesian coordinate transverse to the general flow direction
y	cartesian coordinate parallel to the general flow direction
y^*	dimensionless position from wall for k-epsilon boundary layer
y^+	dimensionless position from wall for large eddy simulation
y_p	distance from wall to point P inside a boundary layer

Greek Symbols

β	angle of sidewalls relative to die face
γ	ratio of specific heats
ε	turbulence dissipation rate

κ	von Kármán constant
μ	viscosity
μ_t	turbulent "eddy" viscosity
υ	dynamic viscosity
ϕ	generic node variable
θ	included angle between convergent jets
ρ	density
σ_{ij}	stress tensor due to molecular viscosity
σ_k	empirical constant for k equation
σ_ε	empirical constant for ε equation
τ_{ij}	sub-grid scale stress tensor
τ_w	shear stress at a wall

Superscripts

-	time mean
~	filtered variable
′	differentiation; turbulent fluctuation
*	dimensionless variable
+	law-of-the-wall variable

CHAPTER I

INTRODUCTION

Melt-blowing is a process in which high-velocity streams of air impinge upon molten strands of polymer to produce very fine filaments. In this process, polymer pellets are heated and extruded through a small orifice located between two converging air jets. The momentum of the high-velocity jets transports the molten polymer to a collection drum. The resulting nonwoven fabrics are used for high-performance filters, medical garments, and insulating materials.

Most of the airflows involved in nonwoven fabric manufacturing are highly turbulent. Although the time-averaged flow field information is very valuable for many applications, such as the fiber-cooling rate, the time-dependent, unsteady character of the flow field plays an important role in determining the uniformity of the fiber lay-down process. The presence of turbulence causes numerous undesired effects such as entanglement between fibers near the head of the die [1]. These defects in fiber quality, known to cause the web defect "shot" [2], are the motivating factor to investigate the turbulent structures at hand. A majority of our knowledge of the melt-blowing velocity field comes from experimental studies. In these studies, a cylindrical-impact Pitot tube is often used to measure average velocities at different distances from the die. Other techniques, such as laser Doppler velocimetry and hot wire anemometry, can provide all three of the vector components of the velocity field. Unfortunately, these techniques present difficulties in making measurements very close to the die [1].

Apart from the difficulty of making measurements for all components of the velocity field and in the region close to the die, experimental setups must be changed manually for testing different die geometries. This testing is performed in order to predict effects that different die designs have on the mean flow field and on the turbulence fluctuation at the die centerline. These two factors affect the efficiency of the melt-blowing process [3]. A high mean air velocity in the centerline is desirable because high air velocity provides high drag on the fiber, and, thus, rapid fiber attenuation [4]. In contrast, turbulence viscosity fluctuations should be as small as possible to avoid instabilities in the formation of the polymer thread [1]. Unfortunately, this type of testing requires a considerable time commitment along with substantial manufacturing costs. One of the motivations of using computational fluid dynamics (CFD) to investigate the flow field below a dual jet is to test different jet geometries without the time and financial commitment of actually manufacturing these structures.

Most CFD codes presently used for high-Reynolds-number flows are based on Reynold-Averaged Navier-Stokes (RANS) equations together with a turbulence model. Although RANS correctly predicts the mean flow in many cases, it often fails when facing more complex flows. Moreover, RANS is not appropriate when unsteady flow features dominate the flow [5], [6]. On the other hand, direct numerical simulation (DNS), in which all flow scales are properly resolved, is usually too computationally expensive for most practical engineering flow problems. A promising alternative model is called “large eddy simulation” (LES) [7], in which only large-scale motions are resolved explicitly, while the effect of the small, unresolved eddies are modeled with a

sub-grid turbulence model. The origin of LES comes from meteorology, where the modeling of large-scale motion is used to predict weather patterns and to simulate the turbulent phenomena between tall city buildings. Today, LES is applied to numerous complex flows with a good degree of success.

In the present study, a computational investigation is conducted in which LES is used to model the large-scale turbulent structures that dominate a melt-blowing flow field. This investigation is performed using FLUENT, a world-renowned supplier of CFD software. As far as the melt-blowing process is concerned, this software is capable of modeling three-dimensional eddy structures as well as a multiphase model of the molten polymer. However, such complexities are not considered in the present study. Instead, a two-dimensional LES model is used to simulate the turbulence of two converging jets, for an incompressible and isothermal condition. Only the airflow characteristics are studied; therefore, the presence of a molten fiber is not included in the model.

Objectives

The following is a list of the major objectives that were addressed during this research:

- use an incompressible, isothermal, LES model to simulate the vortical structures caused by converging jets

- examine the time-averaged velocity field for jets converged at angles of 30° and 60°.
- examine the time-dependent, centerline velocity fluctuations for jets converged at angles of 30° and 60°.
- compare the normalized, mean velocity field between the LES solution and experimental measurements

CHAPTER II

LITERATURE REVIEW

The melt-blowing process has been studied experimentally since the 1950's. However, with the constant evolution of computing capabilities, CFD has become a valuable tool in the recent research of this topic. For many practical turbulent flows, the Reynolds-Averaged Navier-Stokes (RANS) method has proven to be a useful tool. RANS simulations have shown good results in standard applications, such as turbulent channel flows. For the particular case of a melt-blowing die, Krutka et al., [1] used a k-epsilon RANS model to investigate the different merging zones of the converging jets. In their study, they found that there are three distinct merging zones after the jets left the die face. The first zone, which was immediately below the die, exhibited two separate jets from each air slot. In the second zone, the jets began to merge together, but there were still two separate local maxima of velocity. Finally, in the third zone, the two jets completely merged together into a single jet. As a verification study, Hatcher [5] was able to reproduce these results using the same RANS model. Unfortunately, when applied to more complex or unsteady flows, the RANS models have demonstrated significant limitations. Moin et al., [8] had difficulties in predicting flow separations because the turbulence model was not able to take complex vortical motions into account. Both Hatcher [5] and Grald [6] experienced time-dependency problems with the RANS method, and were unable to reproduce any realistic turbulent unsteadiness in their

simulations. Not only were the RANS methods unable to capture unsteady, vortex structures, but also they resulted in overly dissipative average flow fields [6].

The most detailed analysis of turbulent flows has been performed using Direct Numerical Simulations (DNS), with a very fine mesh to resolve even the smallest scales of motion associated with the physical situation. DNS has been successfully used in the past few years to study transitional and turbulent physics in various simple flow problems [9]. Unfortunately, the grid requirements to resolve all the scales of turbulent motion were too computationally expensive to apply DNS to all but the simplest, practical engineering flows.

Recently, Large Eddy Simulation (LES) has become the effective intermediate approach between DNS and RANS. The idea behind the development of LES was to resolve only the large-scale, turbulent structures and to model the small-scale movement with a Sub-Grid Scale (SGS) model. LES has proven to simulate flow features that cannot be handled with RANS, such as significant flow unsteadiness and vortex-acoustic couplings [10]. In the past few years, several studies have been performed to determine the accuracy and limitations of the LES model for free shear flows [11], [12], [13], [14]. In 2001, Balaras et al., [15] examined the effect of initial conditions and the size of the computational box on the turbulent statistics and structures in free shear flows. Their findings indicated that both the initial conditions and size of the computational domain had a substantial effect on the shape and evolution of the large eddy structures. Other studies have been conducted to investigate the performance of LES in wall-bounded flows. Unlike in free shear flows, where the dependency of the SGS model was shown to

be weak, the dynamics of wall-bounded flows seemed to rely heavily on the small-scale motions near the wall [10], [16]. These studies have shown that the grid resolution plays a significant role in predicting shear stresses in the near-wall region [14], [17], [18]. In fact, Alin et al., [17] concluded that better SGS models were required to predict drag forces in high-Reynolds-number flows. These issues increased the development of new techniques, which are aimed to combine the LES and RANS methods.

In the most recent research, the concept of a hybrid RANS/LES method has been studied extensively [8], [19], [20], [21]. In the development of the RANS/LES method, practical engineering flows were broken up into simple and complex regions. The RANS method was used to model simple flow regions, while the LES method solved the more complex flow regions. Recently, this hybrid method has been applied to turbo jet engines [8]. In this type of modeling, the RANS model was applied to the compressor and turbine, where flow remained mostly attached to the blades. On the other hand, LES was used to model flow in the combustor, which was characterized by detached flow, chemical reactions, and fuel sprays.

It seems that the LES or hybrid RANS/LES models are suitable to simulate the free shear, turbulent flow downstream of a melt-blown die. Grald [6], an employee of FLUENT Inc., demonstrated how FLUENT software was capable of using LES to capture significant flow features in the melt-blown fabric manufacturing process. In his report, several graphical results were presented to illustrate the vortex structures that were caused by the convergent jet geometry. Unfortunately, Grald made no attempt to validate his results with experimental data. Moreover, virtually no other investigation of this kind

could be located from literature in the public domain. This lack of research is the motivation behind the present study, in which an LES model is used for parametric studies as well as comparisons to experimental measurements.

CHAPTER III

SOFTWARE PACKAGE

Fluent Inc. is known as one of the world-leading producers of computational fluid dynamics (CFD) software. This type of software enables engineers and designers to simulate fluid flow, heat and mass transfer, and the related phenomena of turbulent, reacting, and multiphase flow. The CFD package used in this investigation includes two programs: GAMBIT 2.2 and FLUENT 6.2. GAMBIT provides all the necessary tools to create the geometry of the simulation model, while FLUENT performs all the computational and post-processing tasks.

FLUENT has several components to deal with various aspects of fluid flow. Some components of particular importance to this study include the boundary conditions. With any CFD simulation, it is crucial to implement boundary conditions that resemble the nature of the physical flow being modeled. Second, and equally important to this study, are the calculation procedures used to model turbulence. In this case, FLUENT offers several choices for turbulence modeling. Therefore, the user must investigate which models are appropriate to obtain the desired results in the simulation.

This chapter provides brief explanations of the boundaries and turbulence models that were used throughout this investigation. The calculation procedures are included where appropriate, to supplement the descriptions.

Boundary Conditions

This section provides a brief description of each boundary condition utilized in the present study. It is important to choose boundary types that are relevant to the physical situations that are being modeled. If a poor choice of boundary type is used, the solutions may converge to incorrect or non-physical results, if they converge at all. FLUENT offers a description and the calculation procedure at each of its boundary types so that the user can make an intelligent choice before modeling a flow [22]. The boundary types used in this study include pressure inlets, velocity inlets, pressure outlets, and walls.

Pressure Inlet

Pressure inlet boundary conditions are used to define the stagnation pressure at flow inlets, along with all other scalar properties of the flow. They are useful when the inlet pressure is known but the flow rate and/or velocity is not known. This situation arises in many practical situations, and a melt-blowing die is an example where pressure is the controlled, independent variable. Pressure inlets are suitable for both incompressible and compressible flows, but the calculation procedures are different. For incompressible flow, the stagnation pressure p_o and static pressure p_s are related using a simple form of Bernoulli's Equation:

$$p_o = p_s + \frac{1}{2}\rho u^2 \qquad 3.1$$

where ρ is the density, u is the velocity magnitude. Using the resulting velocity magnitude calculated from Equation 3.1 and the direction vector assigned by the user, the velocity components ($\vec{u}_x$, $\vec{u}_y$) can be calculated. The inlet mass flow rate $\dot{m}$ can then be computed as:

$$\dot{m} = \int \rho \vec{u} \cdot d\vec{A} \qquad 3.2$$

For incompressible flows, density at the inlet plane is kept constant and the stagnation temperature is equal to static temperature.

When modeling compressible flows, the isentropic relations for an ideal gas are applied to relate total pressure, static pressure and velocity at a pressure inlet boundary. First, the Mach number is calculated using Equation 3.3, with γ as the ratio of specific heats (c_p / c_v).

$$\frac{p_o}{p_s} = \left(1 + \frac{\gamma - 1}{2} M^2\right)^{\gamma/(\gamma-1)} \qquad 3.3$$

The velocity magnitude of the fluid at the inlet plane is calculated from the Mach number by Equation 3.4.

$$M = \frac{u}{\sqrt{\gamma RT_s}} \tag{3.4}$$

Then the velocity components are derived from the direction vector entered by the user. For compressible flow, the density at the inlet plane is defined by the ideal gas law in the form:

$$\rho = \frac{p_s}{RT_s} \tag{3.5}$$

where static temperature T_s is computed from the user's input of stagnation temperature T_o in Equation 3.6.

$$\frac{T_o}{T_s} = 1 + \frac{\gamma - 1}{2} M^2 \tag{3.6}$$

The mass flow rate is calculated as shown in Equation 3.2.

Velocity Inlet

Velocity inlet boundary conditions are used to define the flow velocity, along with all relevant scalar properties of the flow, at flow inlets. The stagnation properties of the flow are not fixed, so they will rise to whatever value is necessary to provide the

prescribed velocity distribution. This boundary condition is intended for incompressible flows, and its use in compressible flows may lead to a nonphysical result because it allows stagnation conditions to float to any level. The mass flow rate of the cell faces adjacent to the velocity inlet is calculated using Equation 3.2. The density and temperature at the inlet plane are kept constant.

Pressure Outlet

Pressure outlet boundary conditions require the specification of a static pressure at the outlet boundary. All other flow quantities are extrapolated from the interior. The value of the specified static pressure is used only while the flow is subsonic. If the flow becomes locally supersonic, the specified pressure will be ignored, and instead will be extrapolated from the cells neighboring the boundary. A set of "backflow" conditions, such as stagnation temperature and turbulence intensity, is also specified for flow entering the computational domain through the pressure outlet.

Wall

Wall boundary conditions are used to bind fluids with a solid region. The user is asked to specify several different variables such as wall movement, thermal conditions, shear conditions, and wall roughness. The default settings state that the wall is stationary; no form of energy is transferred through the face of a wall; a no-slip condition is applied to the fluid cell adjacent to a wall; and the wall surface is perfectly smooth.

Turbulence Modeling

It is an unfortunate fact that no single turbulence model is universally appropriate for all classes of fluid flow problems. The choice of turbulence model depends on considerations such as the physics encompassed in the flow, the level of accuracy required, the available computational resources, and the amount of time available for the simulation. To make the most appropriate choice of model for an application, one must understand the capabilities and limitations of the various options.

The purpose of this section is to give an overview of the turbulence models used in this investigation. For mean turbulent quantities, the k-epsilon model is fairly accurate and does not require extensive computational resources. However, to capture the unsteady, vortex phenomenon that occurs in turbulent flow with large-scale structures, the large eddy simulation is better. Although this method requires much more computational effort and time, it provides a better modeling tool for the purposes of this study.

K-Epsilon

The k-ε model is a semi-empirical, two-equation model based on transport equations for turbulence kinetic energy k and its dissipation rate ε [23]. These equations exist under the assumption that the flow is fully turbulent and that effects of molecular viscosity are negligible. The model transport equation for k is an exact derivation of the

momentum equation, while the transport equation for ε is based more on physical reasoning. In FLUENT, k and ε are calculated from the following equations:

$$\frac{\partial}{\partial t}(\rho k)+\frac{\partial}{\partial x_i}(\rho k u_i)=\frac{\partial}{\partial x_j}\left[\left(\mu+\frac{\mu_t}{\sigma_k}\right)\frac{\partial k}{\partial x_j}\right]+G_k-\rho\varepsilon+S_k \qquad 3.7$$

$$\frac{\partial}{\partial t}(\rho \varepsilon)+\frac{\partial}{\partial x_i}(\rho \varepsilon u_i)=\frac{\partial}{\partial x_j}\left[\left(\mu+\frac{\mu_t}{\sigma_\varepsilon}\right)\frac{\partial \varepsilon}{\partial x_j}\right]+C_{1\varepsilon}G_k\frac{\varepsilon}{k}-\rho C_{2\varepsilon}\frac{\varepsilon^2}{k}+S_\varepsilon \qquad 3.8$$

In these equations, G_k represents the generation of turbulence kinetic energy due to the mean velocity gradients, and μ_t is the turbulent "eddy" viscosity. These two variables are calculated from the equations:

$$G_k=-\rho\overline{u_i'u_j'}\frac{\partial u_j}{\partial x_i} \qquad 3.9$$

$$\mu_t=\rho C_\mu\frac{k^2}{\varepsilon} \qquad 3.10$$

The five empirical constants embedded in these relations have the following default values:

$$C_{1\varepsilon}=1.44 \qquad C_{2\varepsilon}=1.92 \qquad C_\mu=0.09 \qquad \sigma_k=1.00 \qquad \sigma_\varepsilon=1.30$$

Although this model works reasonably well for most wall-bounded flows, it is known to be overly dissipative with free-flowing turbulent flows. When computational resources aren't a limiting factor and a more accurate depiction of turbulent unsteadiness is desired, FLUENT offers the Large Eddy Simulation model.

Large Eddy Simulation

A common conclusion of the self-similarity theory, proposed by Andrei Kolmogorov in 1941, is that large eddies are dependent on flow geometry, while smaller eddies are self-similar and have a universal behavior. For this reason, the current practice in computational analysis of turbulent flows involves solving only the large eddies explicitly and using a universal model for the smaller eddies. This type of analysis is called Large Eddy Simulation (LES). LES provides an approach in which large eddies are resolved in a time-dependent simulation using filtered Navier-Stokes equations. The filter is essentially a mathematical manipulation of the exact Navier-Stokes equations to remove the eddies that are smaller than the size of the filter, which is usually taken as the mesh size. As with other modeling approaches, the filtering process creates an additional sub-grid scale stress term, which is modeled using a sub-grid scale (SGS) model. The most commonly used SGS model is the Dynamic Smagorinsky-Lilly model [24], which compensates for the unresolved turbulent scales through the addition of an "eddy viscosity" into the governing equations.

FLUENT filters a node variable $\phi(x')$ with a filter function G as

$$\widetilde{\phi}(x) = \int_D \phi(x')G(x,x')dx' \tag{3.11}$$

where D is the fluid domain. The filter function $G(x,x')$ is defined as

$$G(x,x')\begin{cases} 1/V & \text{for } x' \in V \\ 0 & \text{for } x' \notin V \end{cases} \tag{3.12}$$

Thus the filtering operation resembles finite-volume discretization as

$$\widetilde{\phi}(x) = \frac{1}{V}\int_V \phi(x')dx' \qquad x' \in V \tag{3.13}$$

The filtered continuity and momentum equations then become

$$\frac{\partial \rho}{\partial t} + \frac{\partial}{\partial x_i}(\rho \widetilde{u}_i) = 0 \tag{3.14}$$

$$\frac{\partial}{\partial t}(\rho \widetilde{u}_i) + \frac{\partial}{\partial x_j}(\rho \widetilde{u}_i \widetilde{u}_j) = -\frac{\partial \widetilde{p}}{\partial x_i} - \frac{\partial \tau_{ij}}{\partial x_j} + \frac{\partial}{\partial x_j}\left(\mu \frac{\partial \sigma_{ij}}{\partial x_j}\right) \tag{3.15}$$

where the SGS stress τ_{ij} is defined as

$$\tau_{ij} \equiv \rho\overline{u_i u_j} - \rho\tilde{u}_i\tilde{u}_j \tag{3.16}$$

and the stress tensor due to molecular viscosity σ_{ij} is defined by

$$\sigma_{ij} \equiv \left[\mu\left(\frac{\partial\tilde{u}_i}{\partial x_j} + \frac{\partial\tilde{u}_j}{\partial x_i}\right)\right] - \frac{2}{3}\mu\frac{\partial\tilde{u}_l}{\partial x_l}\delta_{ij} \tag{3.17}$$

The SGS stresses are unknown and require modeling. FLUENT calculates these stresses from

$$\tau_{ij} - \frac{1}{3}\tau_{kk}\delta_{ij} = -2\mu_t\tilde{S}_{ij} \tag{3.18}$$

where μ_t is the SGS turbulent "eddy" viscosity, and S_{ij} is the rate-of-strain tensor for the resolved scale defined by

$$\tilde{S}_{ij} \equiv \frac{1}{2}\left(\frac{\partial\tilde{u}_i}{\partial x_j} + \frac{\partial\tilde{u}_j}{\partial x_i}\right) \tag{3.19}$$

Using the Smagorinsky-Lilly model, the turbulent viscosity is modeled by

$$\mu_t = \rho L_s^2\sqrt{2\tilde{S}_{ij}\tilde{S}_{ij}} \tag{3.20}$$

In this equation, L_s is the mixing length, and is computed using

$$L_s = \min\left(\kappa d, C_s V^{1/3}\right) \tag{3.21}$$

where κ is the von the volume of the cell, and C_s is the Smagorinsky constant. By default, FLUENT uses a value of 0.1 for the Smagorinsky constant. However, since this value is not universal for all flows, the constant C_s can be dynamically computed based on the information provided by the resolved scales of motion. This method of computing C_s, created by Lilly [24], is called the Dynamic Smagorinsky-Lilly Model.

CHAPTER IV

COMPUTATIONAL PROCEDURE

This chapter describes the steps that were required to develop an adequate LES model for simulating the turbulent flow of two convergent jets. This chapter is broken into five major sections. The first three sections contain the preliminary steps of the computational tests entitled: (1) Preliminary LES Trial, (2) LES With 2-Inch Channels, and (3) Channel Study. The first section discusses an attempt to repeat the results of a previous study, "Performance Analysis of Melt-blown Dies Using Computational Fluid Dynamics," which was published by Eric Grald of FLUENT Inc [6]. The second and third sections discuss the evolution of the computational model as it was applied to the typical geometry and operating conditions used at the University of Tennessee. These sections discuss the problems that were encountered with LES and include supplemental research to support the changes made during this process. The last two sections contain the final procedures for this investigation that yielded results. These sections are: (4) LES With Removed Channels, and (5) CFD Comparison With Experimental Measurements. It should be noted that in this chapter and all following chapters, all uses of the term "velocity" refer to a velocity *magnitude*, unless specifically stated otherwise.

Preliminary LES Trial

In order to gain confidence with FLUENT, an attempt was made to reproduce the results obtained by Eric Grald [6] from his paper entitled "Performance Analysis of Melt-Blown Dies Using Computational Fluid Dynamics." In his report, Grald demonstrated how the LES model could be used to capture the unsteady, turbulent phenomenon that is associated with melt-blown dies. The model geometry and procedure in his report was very similar to the expected geometry and procedure of this study. Exact numerical results from the report were not available for comparison, nor were they necessary. Instead, graphical comparisons were made using temperature contour plots produced in FLUENT.

The geometry used in Grald's report was replicated with only a few, minor deviations to simplify the meshing procedure. As shown in Figure 4.1, the die exit face was created flush with the sidewalls. In contrast, Grald's die face had an outset distance of 0.0127 cm beyond the sidewalls. Secondly, the flow domain was created as a perfect rectangle, whereas Grald used a truncated flow domain so that the domain width increased linearly with the downstream position. A comparison between the two grids is shown in Figure 4.2, where each boundary is labeled with pressure inlet (PI), pressure outlet (PO), or wall (W). All other settings in FLUENT were set to match Grald's simulation exactly.

The LES model was allowed to run for 100,000 time steps, with each time step equaling one microsecond. This allowed time for the simulation results to become

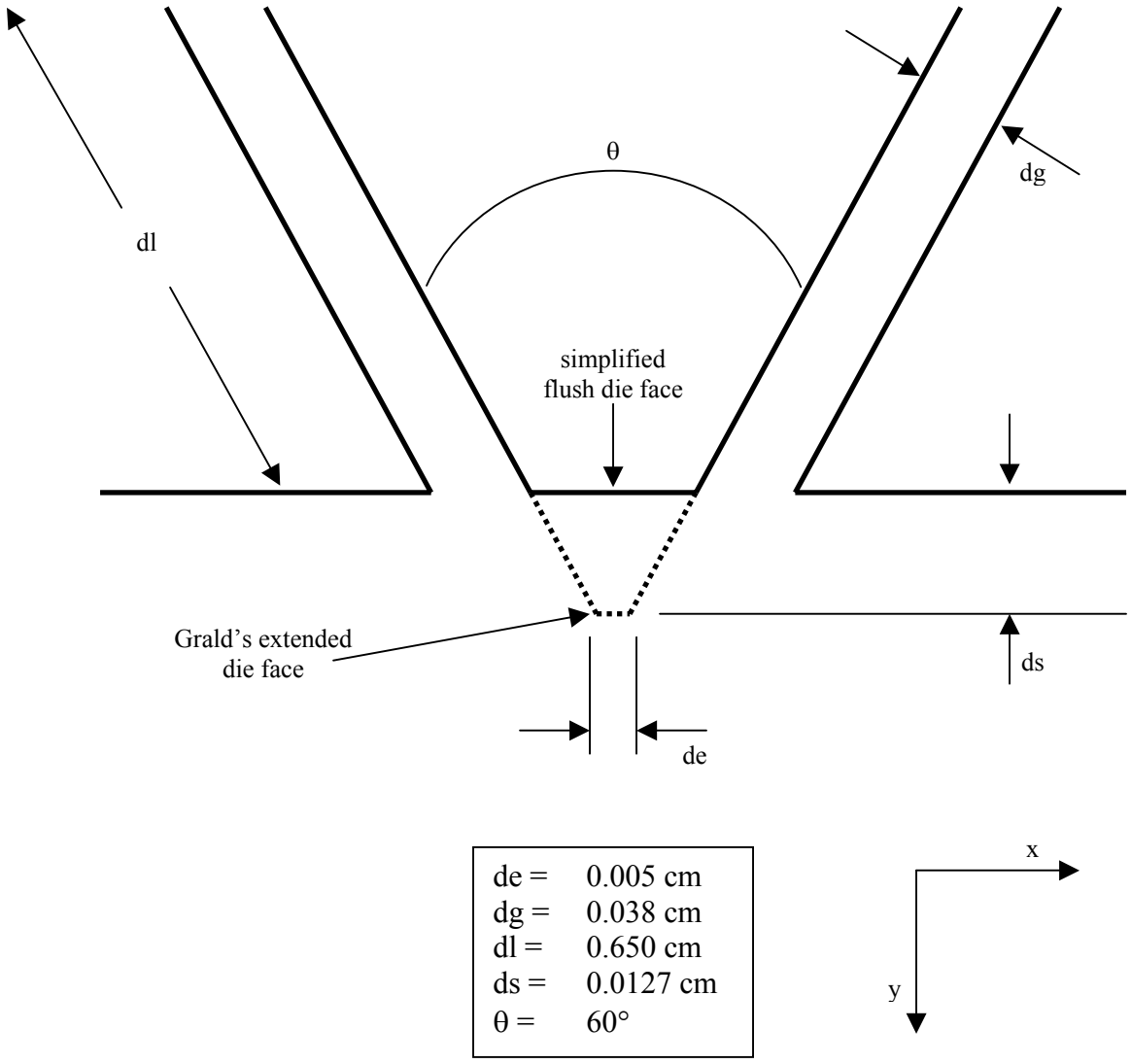


Figure 4.1 Geometric layout of the channel exits with dimensions given to illustrate the difference between die face outset in Grald [6] and the simplified flush die face.

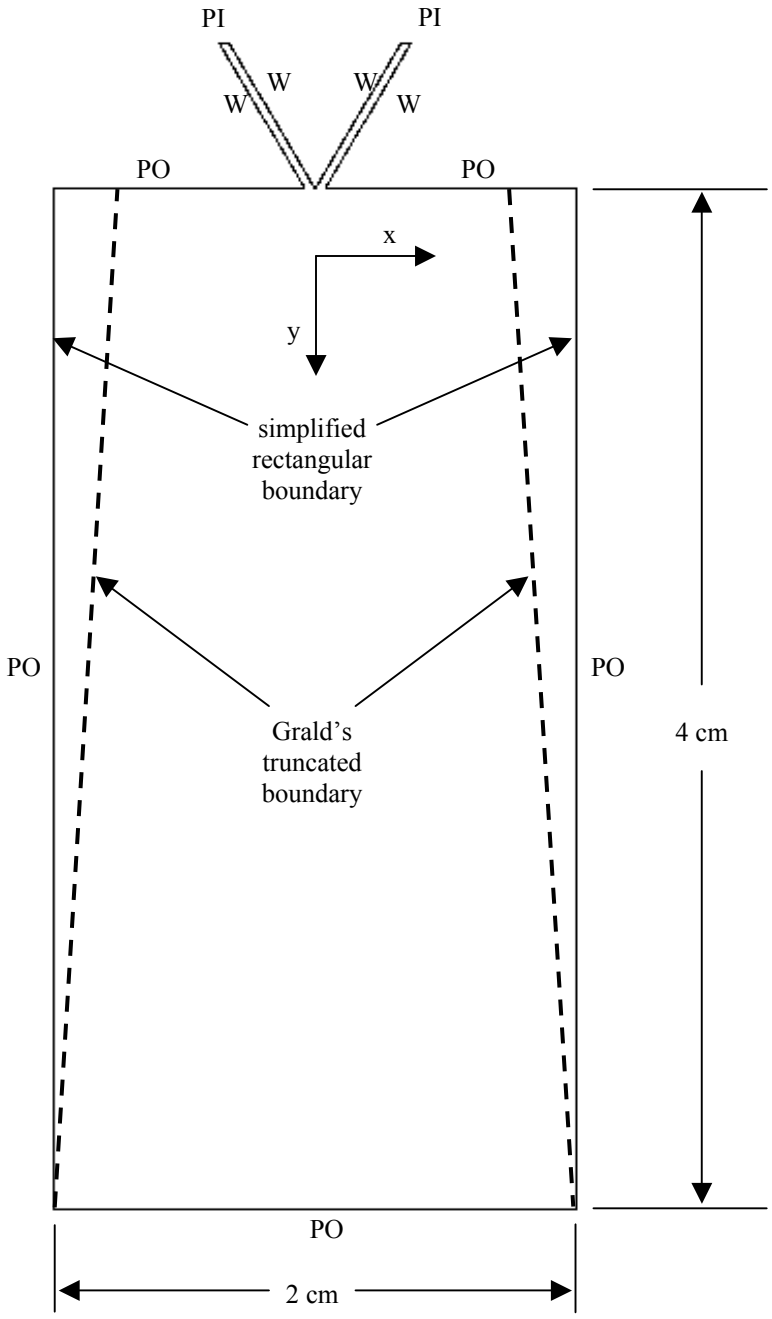
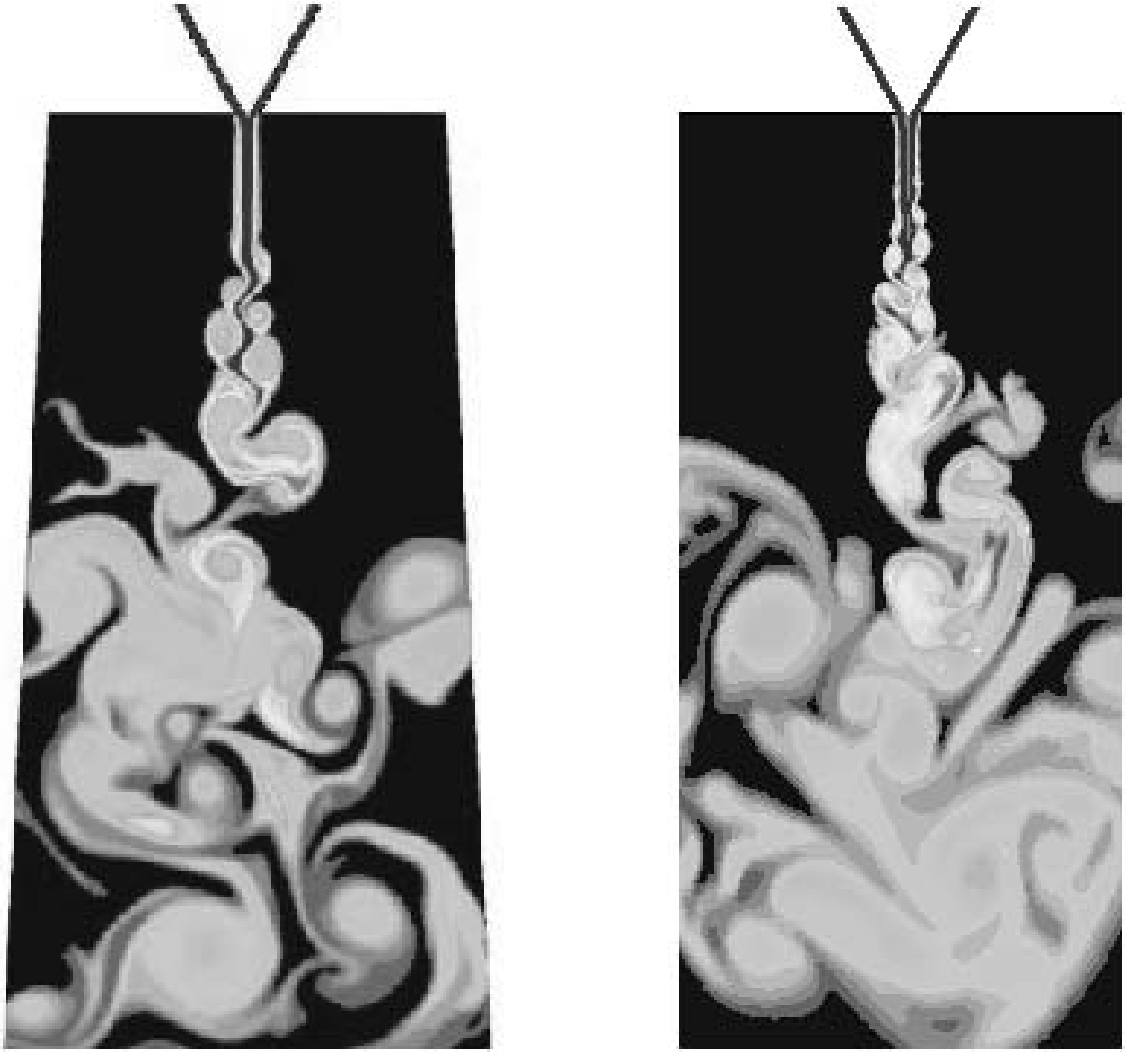


Figure 4.2 Geometric layout of the grid boundaries to contrast the truncated domain from Grald [6] with the simplified rectangular domain used for comparison. Boundaries are abbreviated as: pressure inlet (PI), pressure outlet (PO), and wall (W).

independent of the initial, numerical transients, and for the flow to reach a statistically steady, turbulent state. As shown in Figure 4.3, the reproduced temperature contour showed vortices forming closer to the die exit than in Grald's results. Further downstream, the swirling nature and sizes of the vortex structures was comparable between the two contours. For the purpose of this study, it was neither necessary nor possible to achieve Grald's results exactly for some random snapshot of time. The random, sporadically located vortices were enough to indicate that the LES model was capable of producing the turbulent phenomenon present in the flow. Therefore, it seemed that the FLUENT model was set up properly, and that the software could be applied to the current study with some confidence.

LES With 2-Inch Channels

At the University of Tennessee, several different experimental configurations for the melt-blown die geometry have been used in past research [2], [4]. Some of the attachments were even adjustable so that the channel widths could be changed to the user's preference. For this initial computational study, the geometry of the air channels was created using dimensions that were typical of those used in industry. Specifically, the channels were given a total length of two inches, a width of 0.013 inches, and an included angle of 30°. The downstream flow domain consisted of a rectangular shape with a width of 0.75 inches and a length of 1.5 inches. An illustration of the channels and the flow domain is shown in Figure 4.4. Inside the channels, the mesh was spaced evenly



Grald's temperature contour

Reproduced temperature contour

Figure 4.3 Comparison between the temperature contours from Grald [6] and a simulation performed with matching conditions.

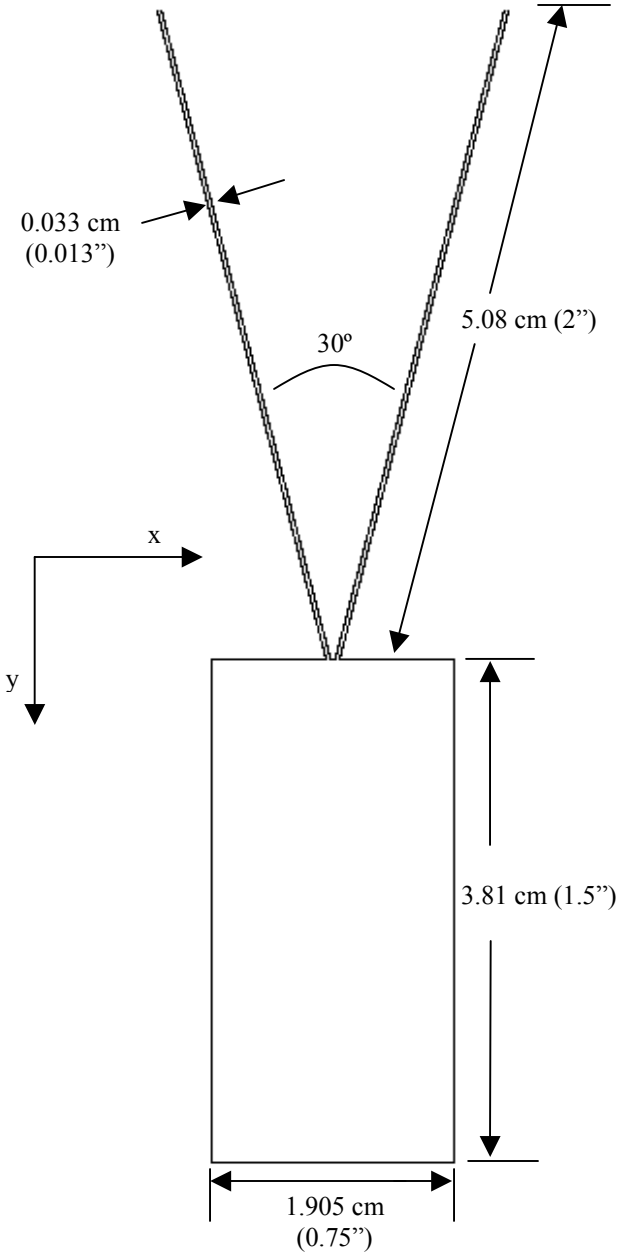


Figure 4.4 Geometric layout of the computational grid used for the 2-inch channel run.

such that ten cells spanned the width of the channel exit plane. The mesh of the flow domain was spaced to provide a smooth transition at the channel exit, however, each consecutive node spacing increased by 5% in the x-directions and 0.5% in the y-directions toward the pressure outlets. A magnified view of the mesh spacing at the channel exits is shown in Figure 4.5. The completely meshed geometry consisted of 89,000 nodes in all, with 30,000 nodes located inside the channels and 59,000 nodes located in the flow domain.

In the previous section, the inlet boundary conditions were set to simulate typical pressures and temperatures of air in the melt-blowing process. However, while this computational study was being performed, melt-blowing experiments at the University of Tennessee were being conducted at room temperature. An attempt was made to match these conditions in FLUENT for future comparisons between the CFD results and the laboratory measurements. Since the air was being blown at room temperature, the effects of temperature gradient were reduced significantly. Because of the computational effort involved, it was beneficial to turn off the energy equation completely, instead of specifying the inlet boundary temperature to be 298 K. To further simplify the calculations in FLUENT, the inlet pressure boundary was set to 2 psig, which was low enough to maintain incompressible flow inside the channels. This eliminated the need to calculate density from the ideal gas law, allowing it to be held constant at 1.225 kg/m^3.

Once the boundary conditions were set, the steady k-epsilon model was used to provide an initial flow field for the LES model. After approximately 800 iterations, the k-epsilon model converged to a steady solution, and the LES model was set to run for

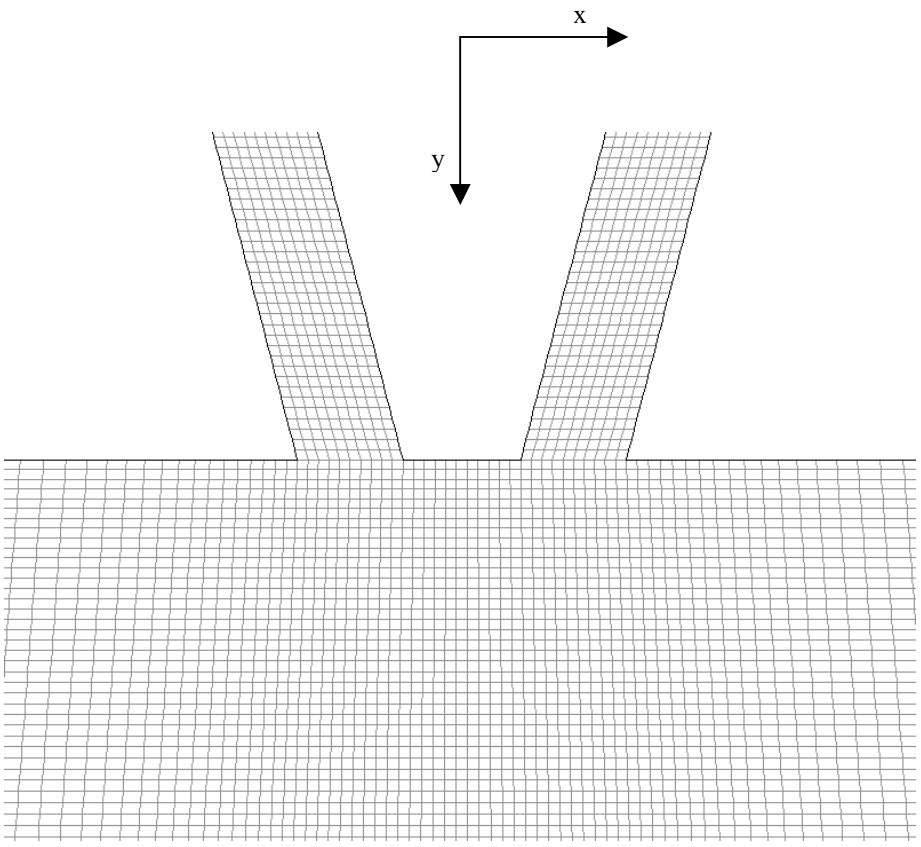


Figure 4.5 Magnified view of mesh spacing near the channel exits from the geometric configuration in Figure 4.4.

100,000 time steps of one microsecond each in batch mode (APPENDIX A). The choice of time step size was the result of several trials in which the iterations required for convergence were monitored between each step of time. Based on the recommendations from FLUENT [25], the time step was adjusted until FLUENT's calculations required 5-10 iterations to converge between each step.

During the calculation time, which spanned many days, there were several discussions with the research committee on how to make the mesh more efficient. Particularly, there seemed to be a lot of wasted computation inside the channels, which contained approximately one-third of the total number of nodes. It was concluded that if the flow became fully developed inside the channel, there was no need to keep the length of channel downstream of the fully developed location. It was decided to use these excess nodes for a longer flow domain, where the results are of more interest. To calculate the velocity required for turbulence inside a two-dimensional channel, the Reynolds number was calculated based on the concept of hydraulic diameter. According to White [5], the Reynolds number for flow between parallel plates is calculated as

$$\mathrm{Re}_{D_h} = \frac{\rho u_{av} D_h}{\mu} \qquad 4.1$$

where ρ is the density, u_{av} is the average velocity, μ is the viscosity, and D_h is the hydraulic diameter (Equation 4.2).

$$D_h = 2(dg) \qquad 4.2$$

In Equation 4.2, *dg* represents the width of the channel or "gap width" for the 2-D slot. Typically, in circular pipe flow, the transition region between laminar and turbulent flow occurs between Reynolds numbers of 2000 and 4000. Assuming that the hydraulic diameter concept can be compared the pipe relation, the average velocity for fully turbulent flow in a channel can be calculated by inserting these Reynolds numbers into Equation 4.1. With a gap width of 0.0381 cm (0.015"), a density of 1.225 kg/m^3, and a viscosity of 1.789x10^{-5} kg/s-m, the transition between laminar and turbulent flow occurs between velocities of 38 m/s and 77 m/s.

After calculating the required velocity for turbulent flow, the LES model was stopped prematurely at 63000 time steps and the centerline velocity was analyzed from Figure 4.6. Approximating that the mean velocity was about 70-80% of the centerline velocity, the velocity values in Figure 4.6 indicated that the flow was turbulent. Unfortunately, the centerline velocity did not reach a fixed value, as expected from fully developed, turbulent flow. Instead, the centerline velocity continued to increase from the channel inlet to the channel exit. As a method of comparison, the same plot was created using the laminar model and the steady, k-epsilon model. Shown in Figure 4.7, the k-epsilon model calculated a fully developed flow inside the channel, while the LES model treated the channel flow similarly to the laminar model. Alin et al., [17] noted that poor velocity profiles resulted from unresolved scales of motion near the walls of a channel. The unresolved scales are modeled by SGS models, which were often inadequate. It

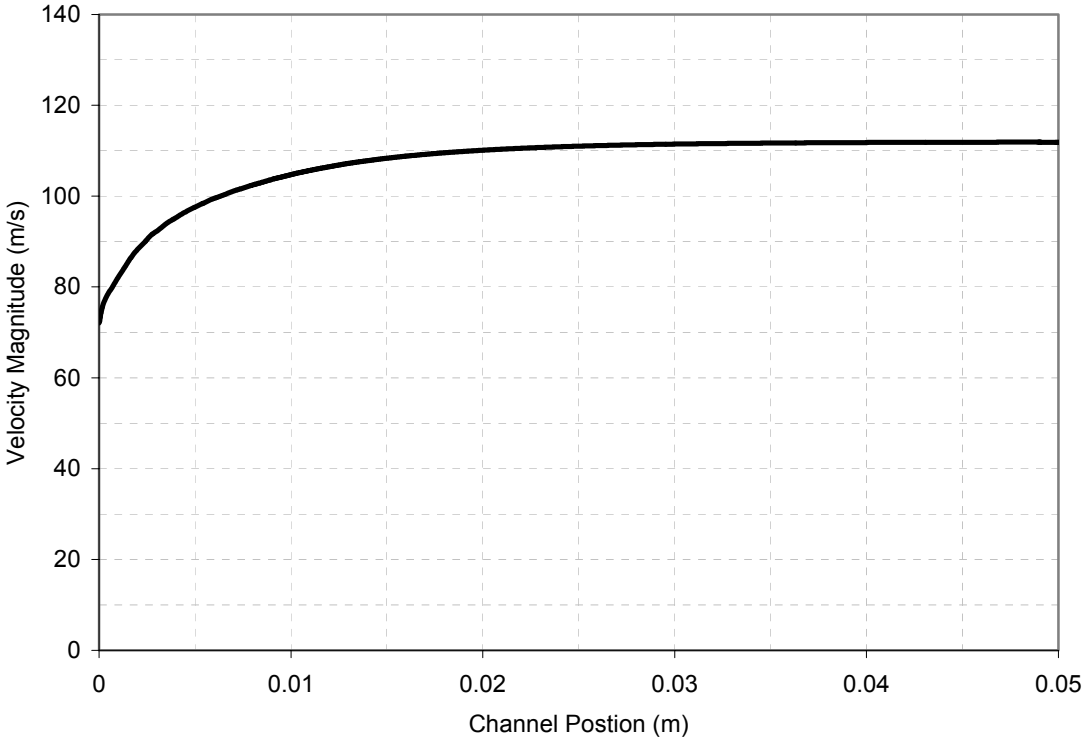


Figure 4.6 Centerline velocity distribution calculated by the LES model inside the 2-inch channel from Figure 4.4.

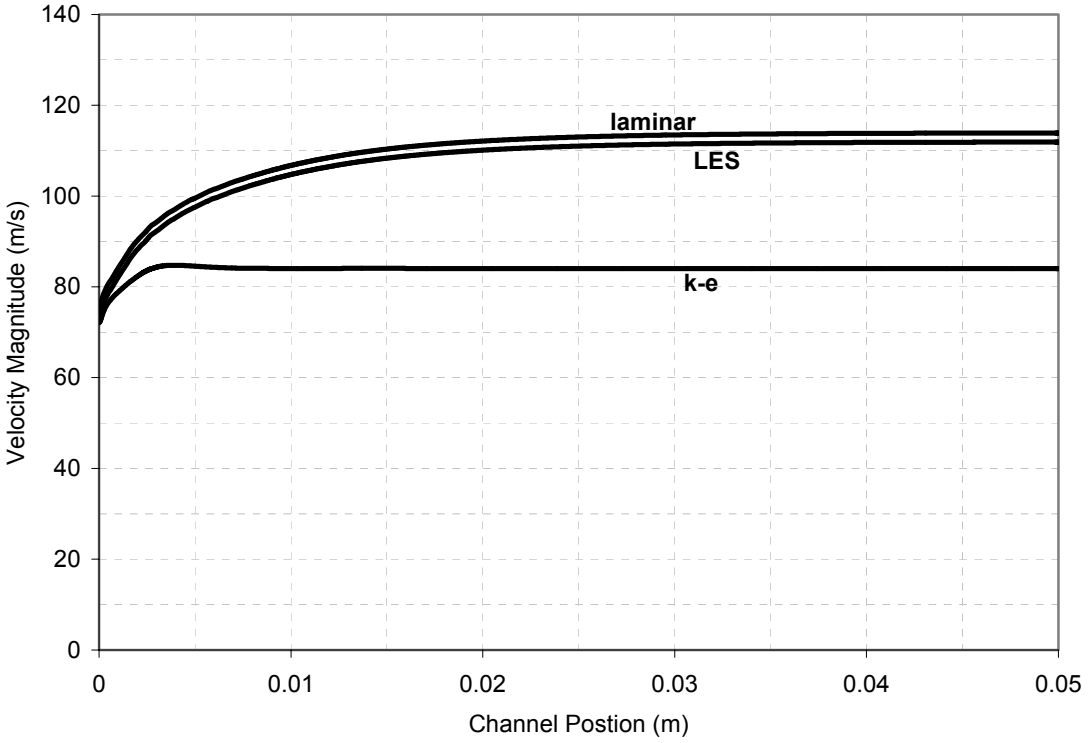


Figure 4.7 Comparison between the laminar, k-epsilon, and LES solutions for centerline velocity inside the 2-inch channel from Figure 4.4.

seemed possible that LES failed to capture these near-wall eddies; but without a separate, thorough investigation, it remained unclear why the LES model did not calculate a fully developed profile. In order to maintain progress in the current study, a new CFD strategy was formed in which the channels were to be removed entirely. In this case, the fully developed velocity profile from the k-epsilon solution would be placed at the channel exits using a velocity inlet boundary.

Channel Study

This section describes the sequential process that was used to obtain a reliable velocity profile for the channel exit. As mentioned in the last chapter, the channel flow did not resemble a fully developed profile when LES was used; thus, it appeared that LES was not an appropriate model to resolve the flow inside the narrow channel. The decided solution to this problem was to remove the channels from the meshed geometry and to replace the channel exit planes with two "velocity inlet" boundaries. This eliminated the problem and freed up more cells for use downstream. The values for the velocity inlet were extracted from a completely separate simulation, in which turbulent flow through a channel was solved with a steady, k-epsilon model.

Before blindly diving into the investigation of turbulent, channel flow, a procedure was created to achieve an acceptable velocity profile while simultaneously exploring the concept of "solution independence." In this case, the calculations were set up using four different initial "guesses" for the y-velocity flow field, in order to test the

solution's independence of the initial flow field. Secondly, this process was repeated using a larger flow domain to make sure that the exterior boundary conditions didn't have an undesirable affect on the upstream flow or the flow inside the channel. After conducting tests of solution independence, the chosen profile was optimized with a second-order upwind scheme and a near-wall mesh refinement. With the refined solution, an additional study was conducted to compare the effects of the inlet turbulence intensity.

Solution Independence

In order to gain confidence in the CFD solution of flow inside a channel, a parametric study was conducted to investigate the independence of the laminar and turbulent solutions to the initialized values of flow variables as well as the grid geometry. Using the domain and mesh geometry shown in Figure 4.8 and Figure 4.9 respectively, a set of four solutions was obtained by varying one flow variable before the iteration process began. In this case, "guesses" of the static pressure and y-velocity components were specified in order to initialize a simple, inviscid flow solution. The orientation of the geometry was such that the general flow moved in the y-direction. Therefore, in each of the four solutions, the initial values of static pressure and x-velocity were set to zero, while the initial "guesses" of y-velocity were specified as 10 m/s, 50 m/s, 100 m/s, and 150 m/s. The resulting inviscid solution was then used as the initial flow field for a laminar model. Likewise, the laminar solution was used as the initial flow field for the turbulent, k-epsilon model. After the flow field was solved for the inviscid, laminar, and

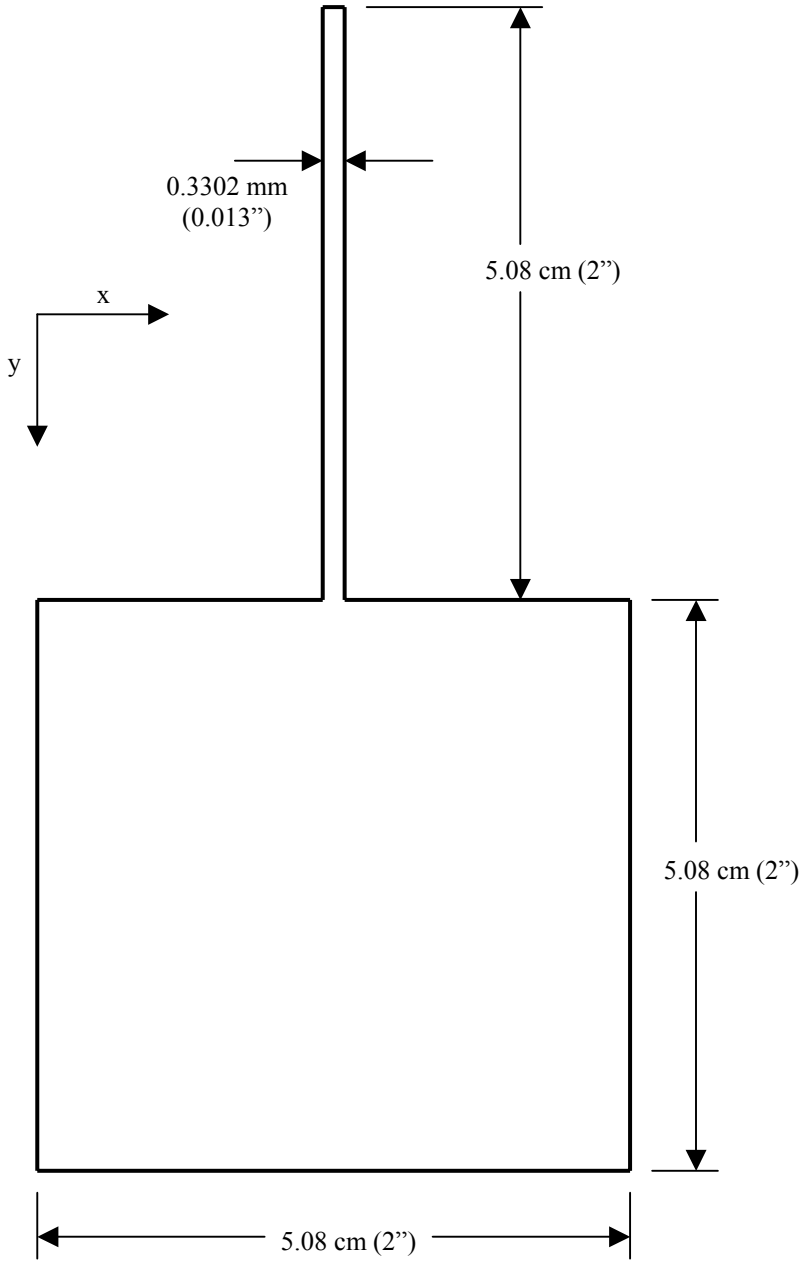


Figure 4.8 Geometric layout of the 2-inch-long flow domain, which was used to obtain a steady-state, k-epsilon velocity profile inside the channel.

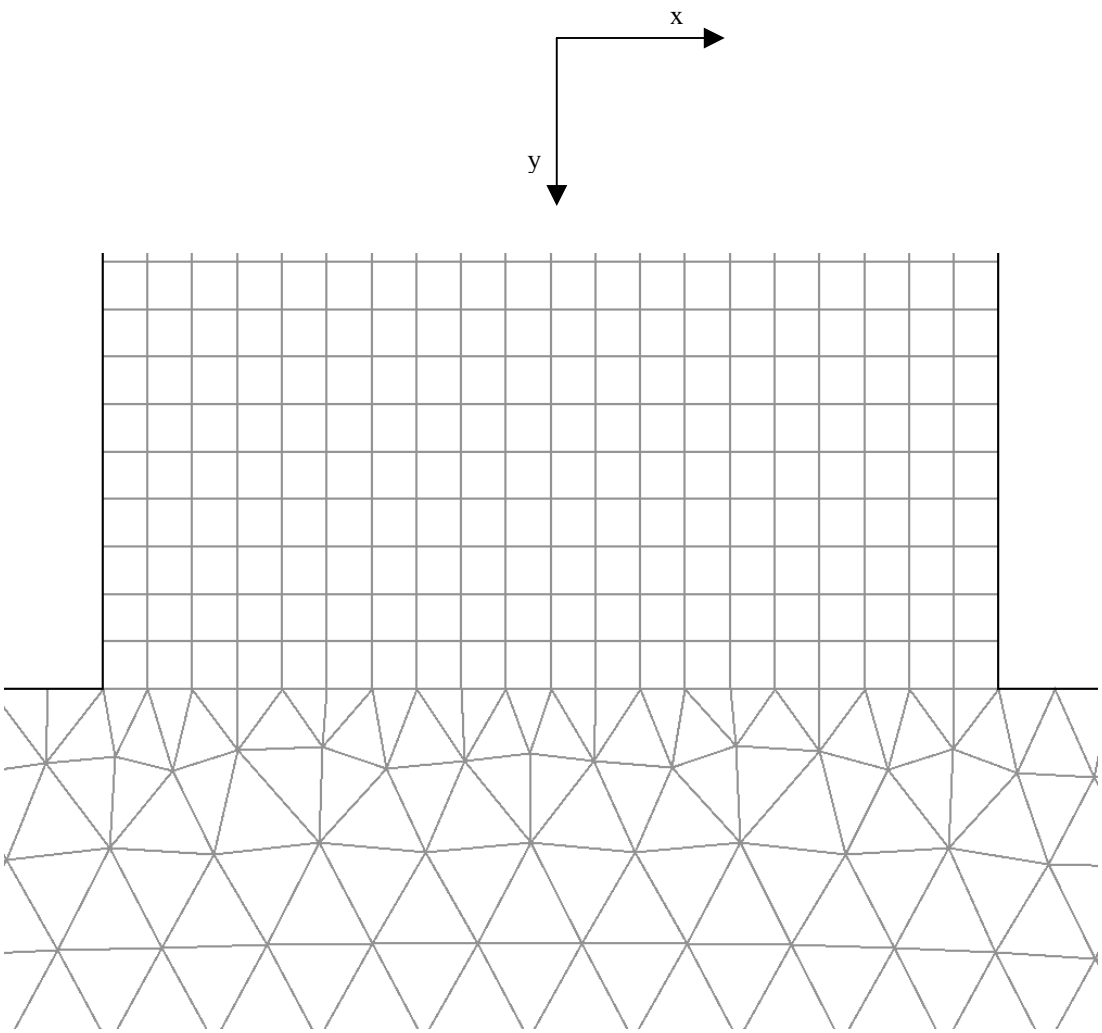


Figure 4.9 Magnified view of mesh spacing near the channel exit from the geometric configuration in Figure 4.8.

turbulent models, the entire process was repeated using the geometry from Figure 4.10. The flow domain size was doubled in the y-direction to ensure that the downstream boundary conditions didn't have an undesirable effect on the upstream velocity. For the sake of consistency, the spacing between the nodes was kept constant.

The solutions in this study were calculated with equations for incompressible flow, and the density was set to a constant 1.225 kg/m^3. The boundary condition at the channel entrance was set as a "pressure inlet," which required the stagnation pressure to be specified. The inlet stagnation pressure was set to the relatively low value of 2 psig to keep the flow Mach number below 0.3, where the incompressible equations remained valid. The boundary condition for the exterior of the flow domain was set as a "pressure outlet" with a static pressure of 0 psig. The energy equation was turned off during this investigation, which eliminated the need to specify a temperature at the boundaries.

The solutions were illustrated with plots of the velocity profile across the width of the channel, taken 0.1 inch upstream of the channel exit. This location was chosen because it was far enough upstream of the channel exit to avoid local effects of the corners, yet was far enough downstream of the channel inlet to obtain a fully developed profile.

2-Inch-Long Flow Domain

The velocity profiles for the k-epsilon model are shown in Figure 4.11. Even though the same pressure ratio was used in each case, the profiles indicated that the final solution was almost directly related to the input for the initialized flow field. With an

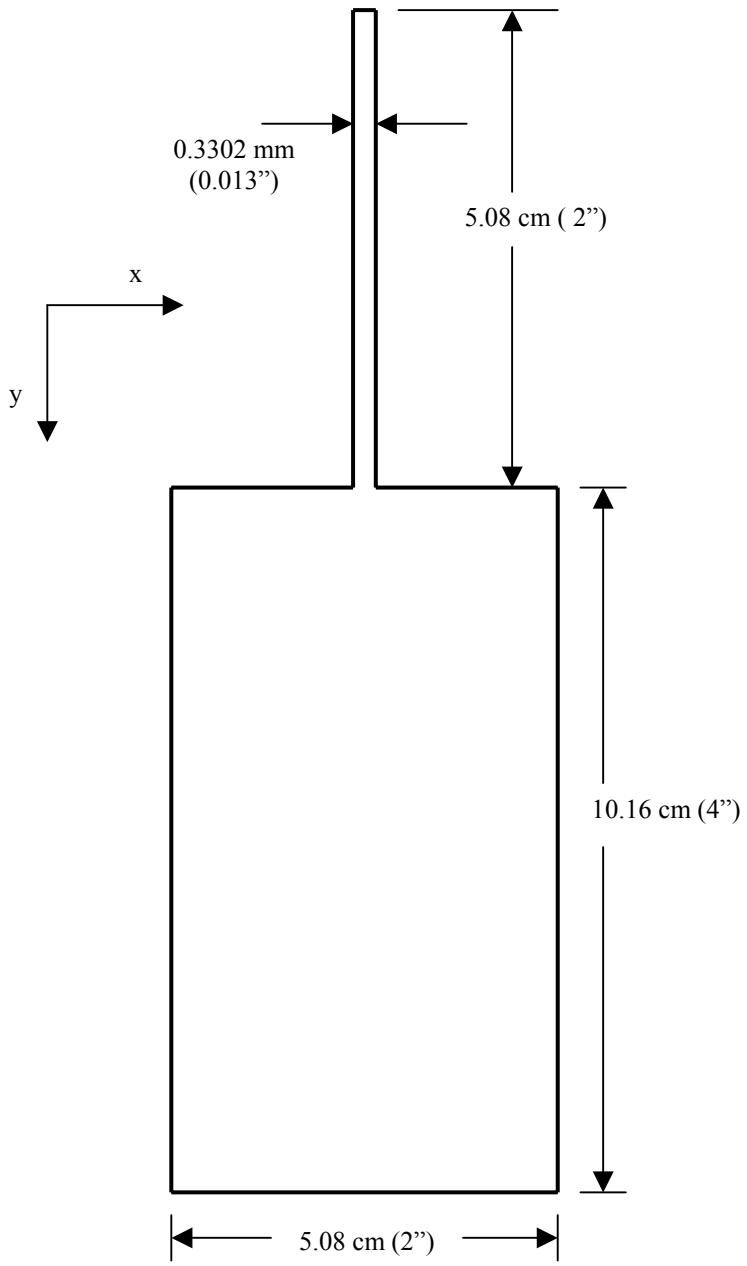


Figure 4.10 Geometric layout of the 4-inch-long flow domain, which was used to obtain a steady-state, k-epsilon velocity profile inside the channel.

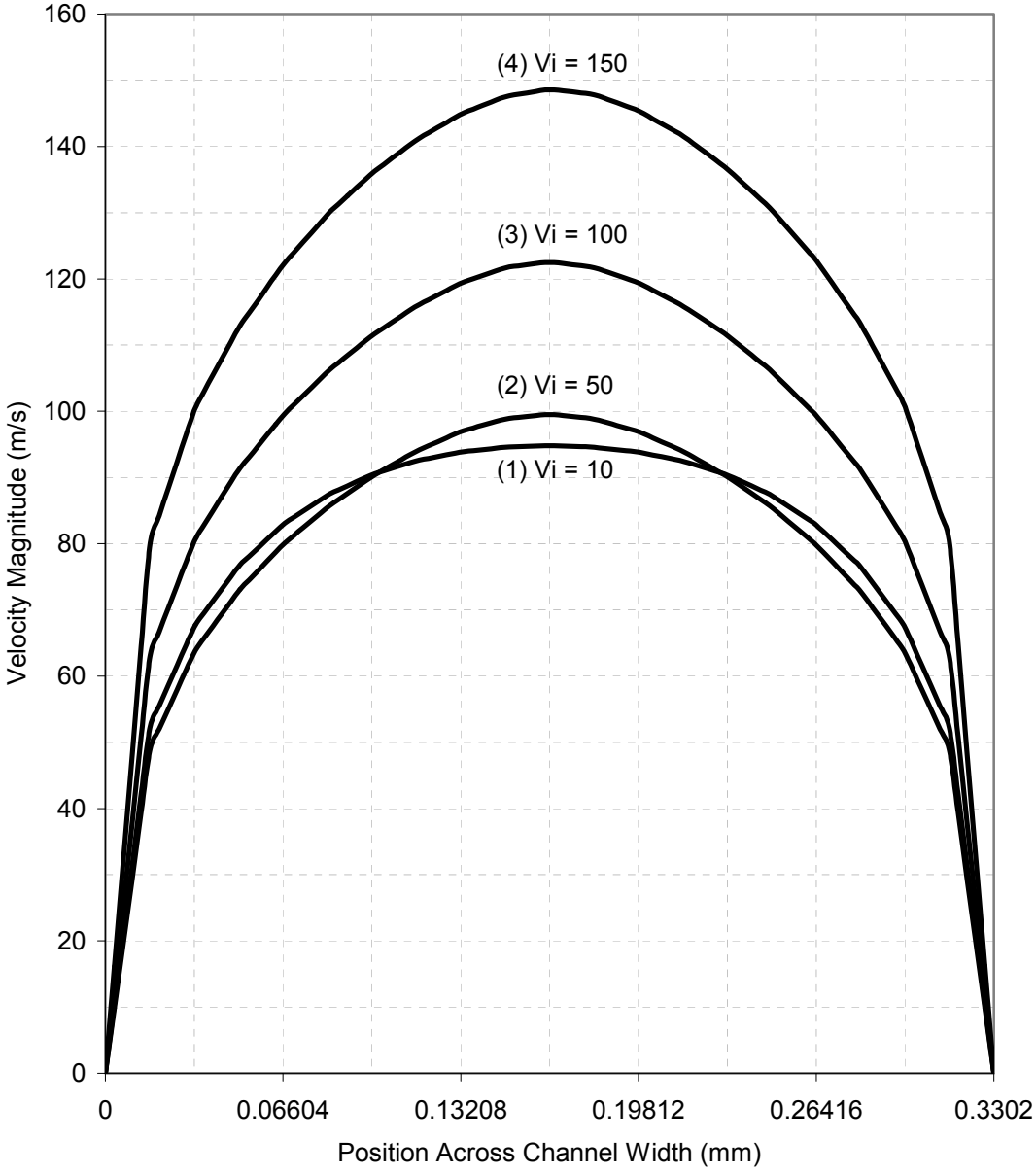


Figure 4.11 Velocity profiles solved with a steady-state, k-epsilon model with various initial "guesses" of the y-velocity flow field using the computational domain from Figure 4-8.

initial guess of V_i = 10 m/s, the first solution resulted in a flattened, parabolic shape, with a maximum velocity close to 95 m/s. The second, third, and fourth solution resulted in a similarly shaped profile, however they exhibited significantly higher values for velocity. In fact, it appeared that the maximum velocity increased in a linear fashion, which showed similarity to the linear increase of the initialized y-velocity. Before any further conclusions were made about the effect of an initial guess, the expansion region of the flow domain was extended by 2 inches in the downstream direction, and the procedure was repeated.

4-Inch-Long Flow Domain

The test performed on the geometry from Figure 4.8 was repeated for the geometry shown in Figure 4.10. In this case, the solutions seemed to suffer less influence from the initial flow field. As can be seen in Figure 4.12, the first three velocity profiles were difficult to distinguish from each other, which indicated that the solutions converged to a consistent result. The fourth model, which was initialized with the highest downstream y-velocity, calculated slightly higher results for velocity. This feature was similar to the trend of the results for the smaller geometry, in that the final velocity increased as the initialized y-velocity increased. Since there wasn't a closer agreement between the solutions of these two tests, a closer examination was needed before a velocity profile was selected for the LES model.

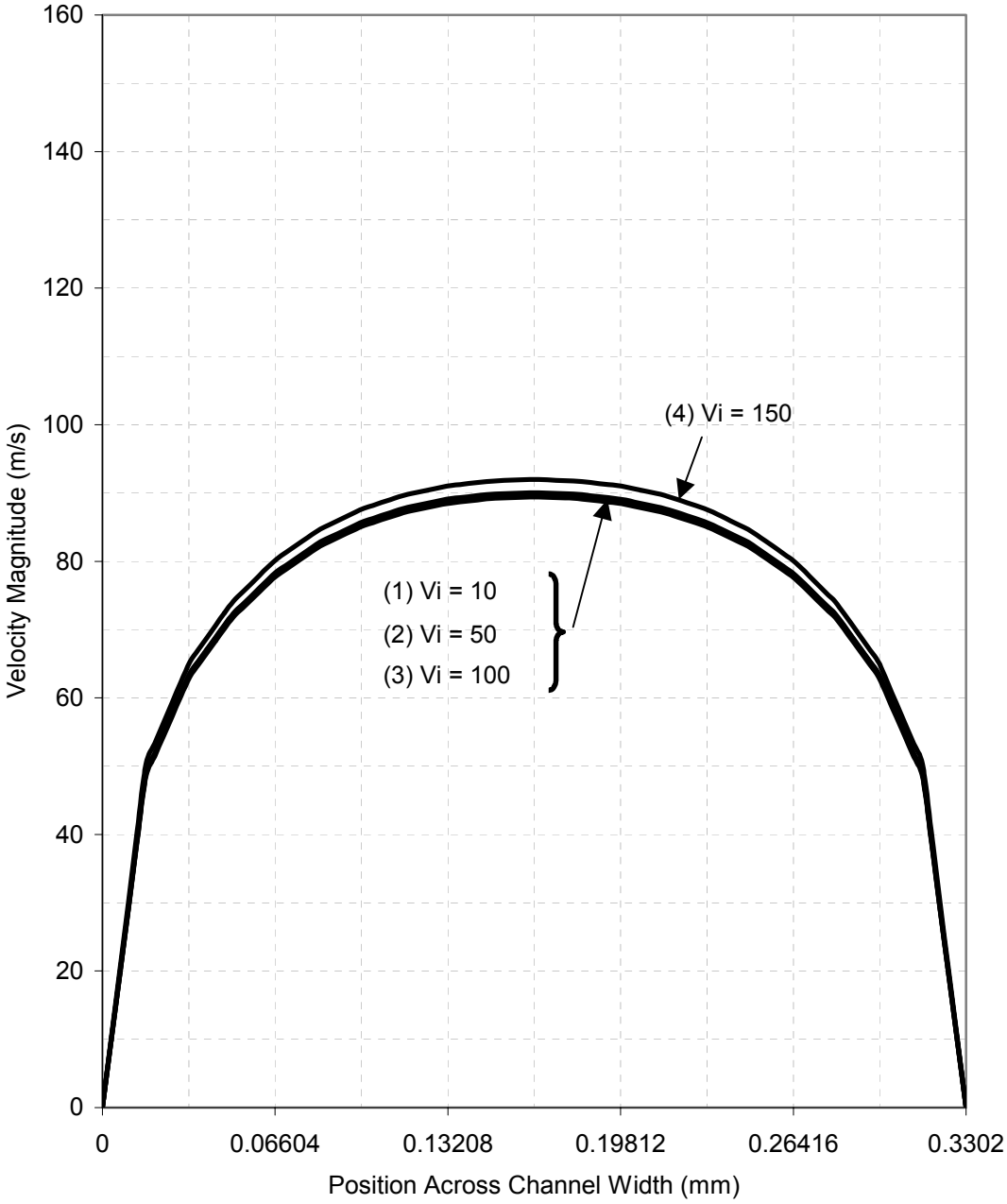


Figure 4.12 Velocity profiles solved with a steady-state, k-epsilon model with various initial "guesses" of the y-velocity flow field using the computational domain from Figure 4-10.

Analysis of Results

Physically, there should be only one solution for an incompressible, pressure-driven flow through a channel. The critical problem with the solutions in Figure 4.11 is that they differ by as much as 50%. This difference is unacceptable by any standards, and appears to be related to the initial flow variables. Since the final values of velocity increase directly with the initial guesses, it seems that the accuracy of the results becomes increasingly compromised once the initialized y-velocity surpasses some unknown, critical value. According to Figure 4.11, the linear trend begins with the second solution; therefore, the critical value for initialized y-velocity is less than V_i = 50 m/s. Since computational convergence is very sensitive to pressure gradients, it is possible that this critical value for initialized y-velocity only exists with the uniform, initial pressure of 0 psig. If the initial pressure field is increased uniformly, or with a user-defined-function, the behavior of the solution may be different.

When comparing the results in Figure 4.11 and Figure 4.12, another trend becomes evident. In both cases, the solution for velocity inside the channel increases as the initialized y-velocity increases. It also appears, from studying Figure 4.12, that this phenomenon becomes less evident for a larger domain size. From these facts, one can draw the conclusion that the solution has a higher sensitivity to the initial flow field when the domain geometry is smaller. Unfortunately, the exact cause of this relationship is unknown, and seems to conflict with two important facts. First, the boundary condition at the exterior of the domain only constrains the static pressure, while extrapolating other variables, such as velocity, from the interior. Second, most of the reduction in static

pressure occurs inside the channel, where the geometry remains the same in both tests. If the static pressure boundary is located somewhere inside the channel, it will produce larger pressure gradients to make up for the decreased length of flow. However, since the location of the static pressure boundary is located downstream of the channel exit, and nearly all of the pressure drop occurs inside the channel, the boundary condition should not cause the flow velocity to differ so greatly. Therefore, it remains unclear as to why the extension of the domain length reduces the sensitivity of the solution with respect to the initialized flow. Clearly, this phenomenon warrants its own investigation but exceeds the scope of this research. However, the velocity profiles in Figure 4.12 are repeatable, and therefore, determined sufficient for the purposes of this study.

Profile Optimization

The velocity profiles from Figure 4.12 had the consistency and desirable shape to be used for further analysis. Specifically, the first solution, with an initial flow y-velocity of V_i = 10 m/s, was chosen to continue the study.

Before implementing this velocity profile as the inlet boundary in the LES model, the results were optimized for the purpose of performing additional parametric studies as well as improving the accuracy of the profile shape. For the first improvement, the k-epsilon model was increased from the first-order upwind scheme to the second-order upwind scheme. The second improvement involved a near-wall mesh refinement.

Order of Discretization Scheme

In an attempt to increase the accuracy of the velocity profile, the default discretization scheme was increased from first-order to second-order. A comprehensive explanation of discretizations schemes is given in the FLUENT 6.2 User's Guide [22]. No other changes were made as the k-epsilon model re-calculated the flow solution. With the second-order scheme turned on, the new equations needed approximately fifty iterations to reach convergence. The second-order velocity profile, shown in Figure 4.13, did not deviate far from the original, first-order solution. The lower values of velocity indicated that the first-order scheme might have been a little under-diffusive with the overall momentum of the flow.

Near-Wall Mesh Refinement

Turbulent flows are significantly affected by the presence of walls, since the near-wall region is where the largest gradients of flow variables occur. The near-wall region is generally divided into three layers. Closest to the wall, there exists a thin viscous layer, where the flow is almost laminar, and viscous (molecular) shear dominates the flow. In the outermost layer, called the fully turbulent layer, the turbulent (eddy) shear dominates the flow. Finally, there is an overlap layer, known as a "buffer" region, where molecular viscosity and turbulence effects are equally important. There are two approaches to model flow in these regions near the wall. In one approach, the two viscosity-affected inner regions are modeled with semi-empirical wall functions. These functions provide a "link" between the wall and the fully turbulent region. In the second approach, the

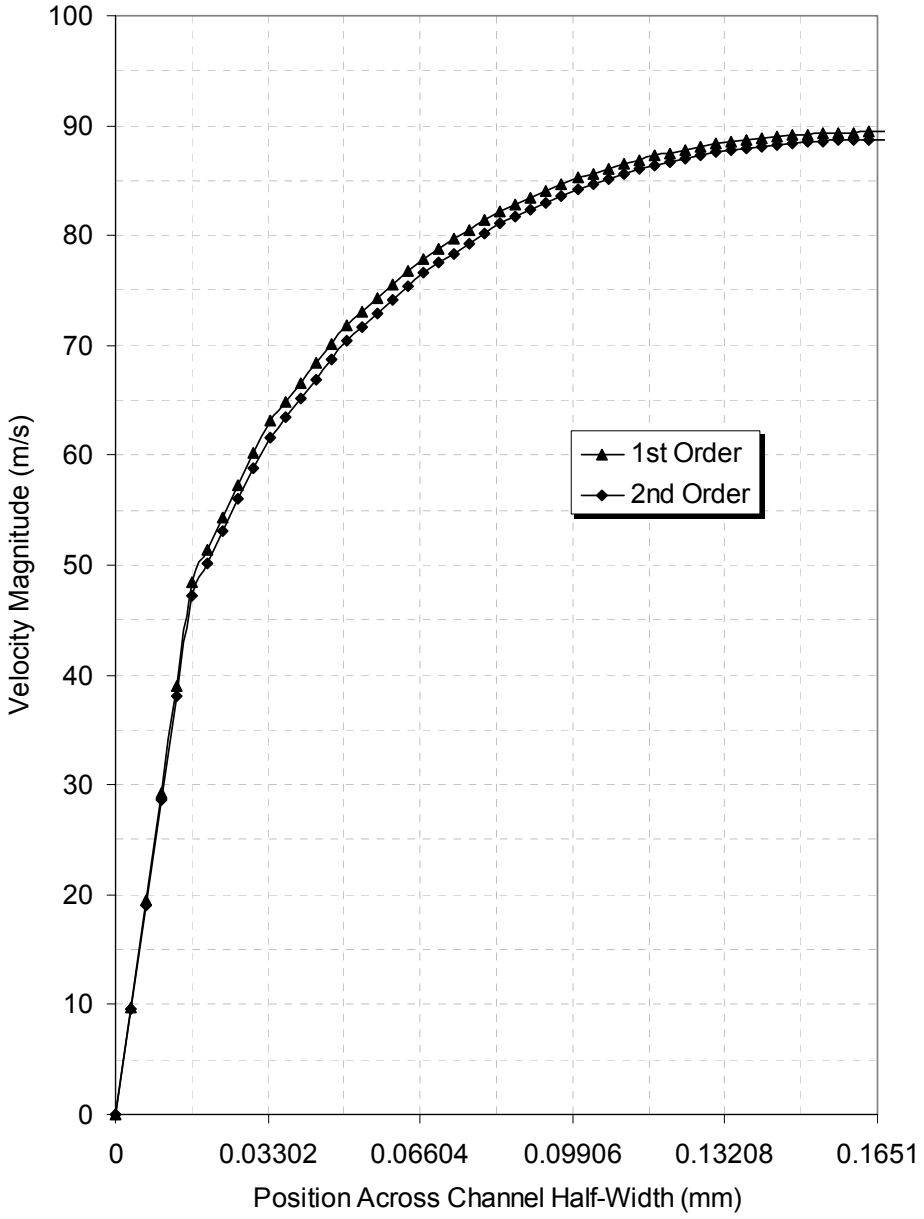


Figure 4.13 Velocity profile comparison of first-order and second-order discretization schemes using the steady k-epsilon model and the computational domain from Figure 4.10.

turbulence models are modified to allow the viscosity-affected region to be resolved with a fine mesh all the way to the wall.

The standard wall functions are set as the default method in FLUENT because they are computationally economical and reasonably accurate for high-Reynolds number flow simulations. Inside the viscous sublayer and the buffer region, the wall functions utilize the law-of-the-wall for mean velocity and formulas for near-wall turbulent quantities. The logarithmic law for mean velocity gives

$$U^* = \frac{1}{\kappa}\ln(Ey^*) \tag{4.3}$$

where

$$U^* = \frac{U_P C_\mu^{1/4} k_P^{1/2}}{\tau_\omega / \rho} \tag{4.4}$$

$$y^* = \frac{y_P C_\mu^{1/4} k_P^{1/2}}{\upsilon} \tag{4.5}$$

and κ is the von Kármán constant (0.4187), E is an empirical constant (9.793) [22], U_P is the mean velocity of the fluid at point P, k_P is the turbulence kinetic energy at point P, y_P is the perpendicular distance from point P to the wall, and υ is the dynamic viscosity of the fluid. Broken up into regions, the y^* values correspond to each layer as shown.

$0 < y^* < 5$	Inner Layer
$5 < y^* < 30$	Overlap Layer
$30 < y^* < 300$	Outer Layer

FLUENT uses the log-law for mean velocity when $y^* > 11.225$. If the mesh is such that $y^* < 11.225$ at the wall-adjacent cells, then FLUENT applies the laminar stress-strain relationship, written as

$$U^* = y^* \tag{4.6}$$

For the k-ϵ model, the k equation is solved in the entire domain including the wall-adjacent cells. The boundary condition for k at the wall is

$$\frac{\partial k}{\partial n} = 0 \tag{4.7}$$

where n is the local coordinate normal to the wall. This local equilibrium hypothesis is used to calculate the production of kinetic energy, G_k, and its dissipation rate, ϵ. With this assumption, the production of k is computed from

$$G_k = \tau_w \frac{\partial U}{\partial y} = \tau_w \frac{\tau_w}{\kappa \rho C_\mu^{1/4} k_P^{1/2} y_P} \tag{4.8}$$

and ϵ is computed from

$$\varepsilon_P = \frac{C_\mu^{3/4} k_P^{3/2}}{\kappa y_P} \tag{4.9}$$

If one wishes to completely resolve the flow all the way to the viscous inner layer, the Enhanced Wall Treatment can be employed along with a sufficiently fine mesh near the wall. The recommended mesh spacing for near-wall calculations is such that

$$y^+ \approx 1$$

where y^+ is defined as

$$y^+ \equiv \frac{\rho y \sqrt{\tau_w / \rho_w}}{\mu} \tag{4.10}$$

In this approach, the entire domain is divided into a viscosity-affected region and a fully turbulent region. These regions are separated based on a turbulent Reynolds number, Re_t, defined as

$$\mathrm{Re}_t \equiv \frac{\rho y_p \sqrt{k}}{\mu} \tag{4.11}$$

where y_p is the perpendicular distance to the nearest wall. In the fully turbulent region ($Re_t > 200$), the k-ϵ models are employed. In the viscosity-dominated near-wall region ($Re_t < 200$), the momentum equations and the k equation are retained, however, the turbulent viscosity, μ_t, is computed from

$$\mu_{t,2layer} = \rho C_\mu \ell_\mu \sqrt{k} \tag{4.12}$$

with

$$\ell_\mu = y\kappa C_\mu^{-3/4}\left(1 - e^{-\mathrm{Re}_t/70}\right) \tag{4.13}$$

Finally, the inner-layer turbulent viscosity is merged with the fully turbulent viscosity from the outer region using a blending function. The blending function simply provides a smooth transition for flow variables between the two regions, in case convergence is compromised.

In order to optimize the velocity profile from the previous section, the enhanced wall treatment was activated, and the near-wall mesh was refined to the suggested resolution ($y^+ = 1$). The mesh refinement process required about five repetitions since the values of y^+ had to be recalculated each time the mesh was altered. The final mesh, shown in Figure 4.14, was consistent with the resolution requirements given by FLUENT. In Figure 4.15, a comparison was made between the two grids, using only standard wall functions. The refined near-wall mesh caused a slight increase in the

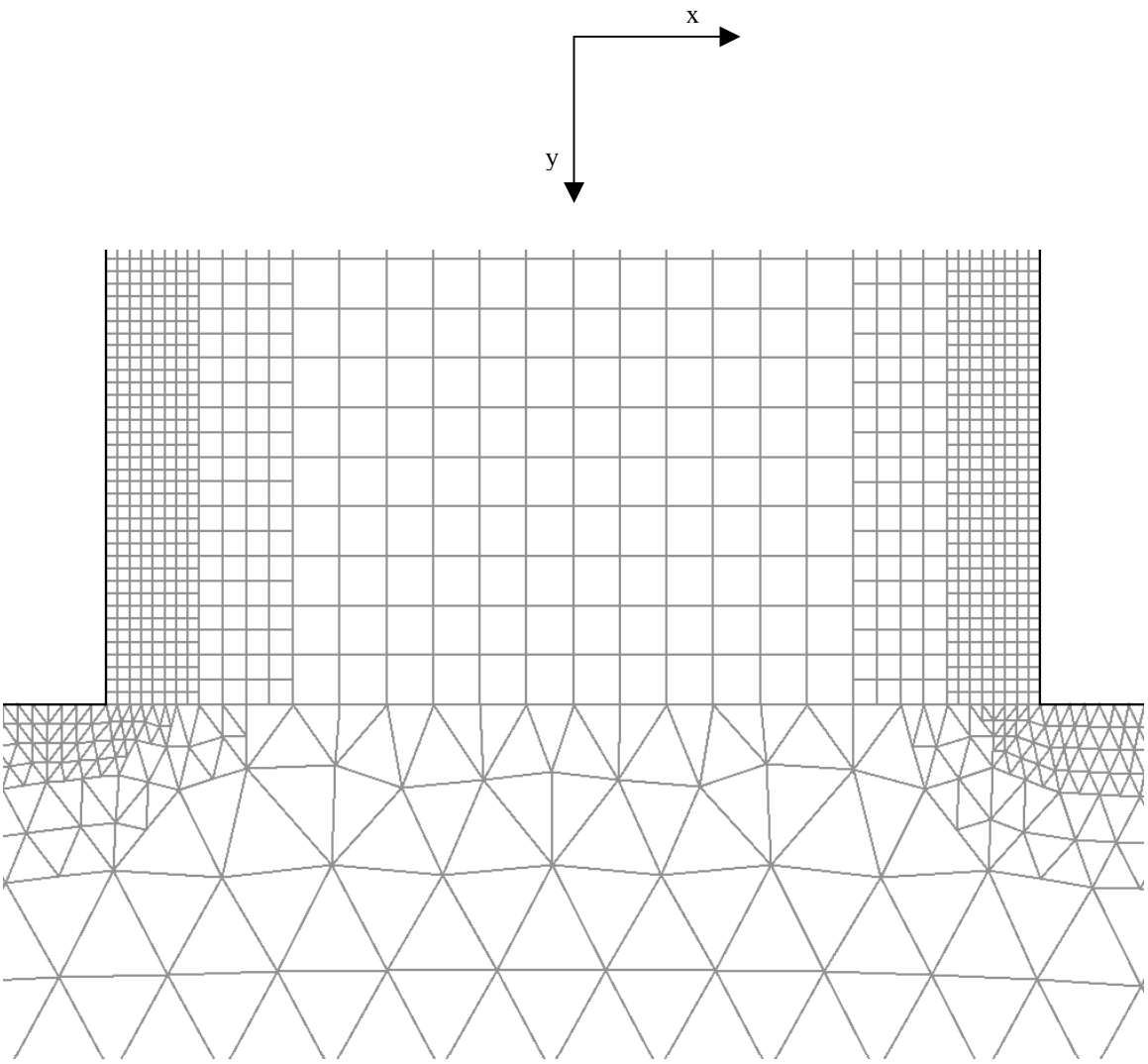


Figure 4.14 Magnified view of the refined mesh spacing near the channel exit from the geometric configuration in Figure 4.10.

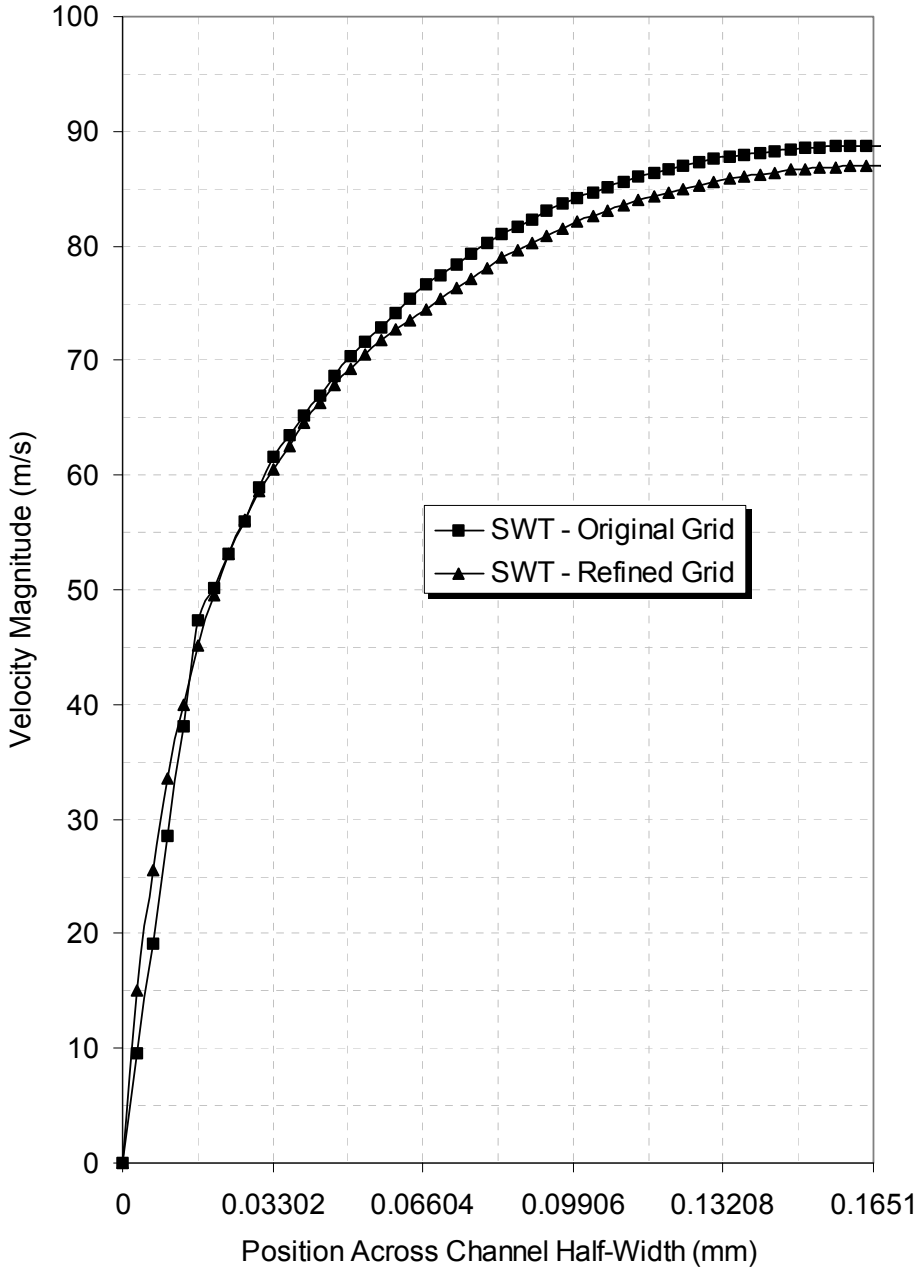


Figure 4.15 Velocity profile comparison between the original and refined grid using standard wall treatment (SWT).

velocity within the inner-viscous region; however, there was a small reduction in velocity outside the inner layer. In Figure 4.16, using the refined mesh, a comparison was made between the standard and enhanced wall treatments. In this case, the velocity from enhanced wall treatment was reduced in both the near-wall and the turbulent regions of the flow. It is likely that the enhanced wall treatment calculated higher shear stresses near the wall, which resulted in a flatter velocity profile. Overall, the near-wall mesh refinement resulted in a flattened velocity profile, with the centerline (max) velocity reduced by about 5 m/s from that calculated by the original grid.

As mentioned earlier, the standard wall functions were the default setting in FLUENT because of their low computational cost and industrial applicability. In this case, the addition of about 20,000 nodes did not affect computational time significantly. When the enhanced wall treatment was activated, the k-ε model converged in 5-10 iterations for each step of mesh refinement. The magnitude and shape of the velocity profile did not change significantly, regarding its use for the LES model. Nevertheless, the investigation of the enhanced wall treatment proved fruitful in that it uncovered more specifics on how FLUENT changes calculation procedures based on mesh spacing.

Turbulence Intensity

The turbulence intensity, I, is defined as the ratio of the root-mean-square of the velocity fluctuations, u', to the mean flow velocity, u_{av}. By default, FLUENT sets the turbulence intensity to 10%, which is generally considered high. In low-turbulence wind tunnels, the free-stream turbulence intensity may be as low as 0.1%. For internal flows,

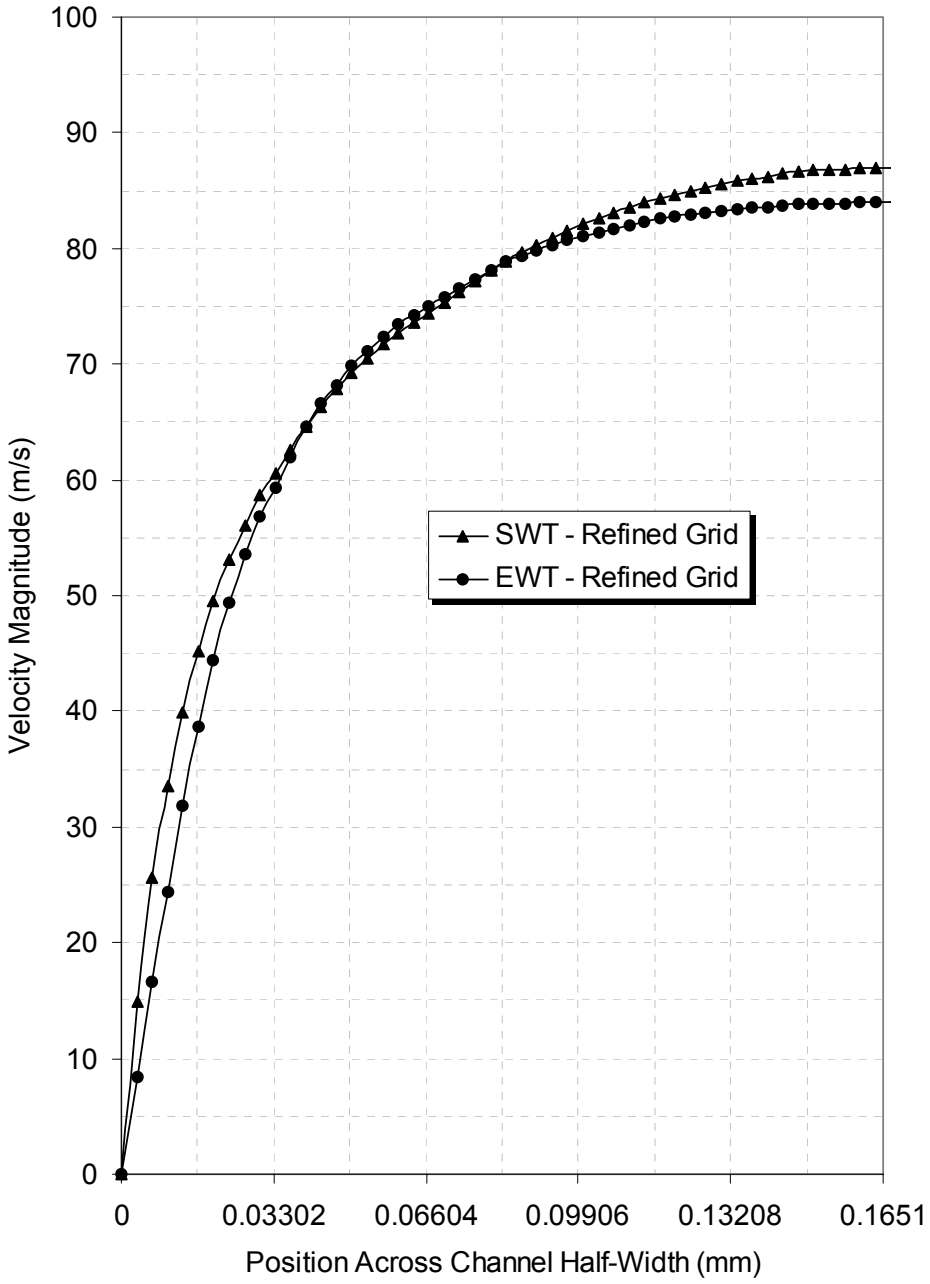


Figure 4.16 Velocity profile comparison between the enhanced wall treatment (EWT) and the standard wall treatment (SWT), using the refined grid.

the turbulence intensity at an inlet is totally dependent on the upstream history of the flow. In the case of the melt-blowing die, the turbulent fluctuations at the entrance of the channel, otherwise known as the air gap, is somewhat unknown.

The final goal of the channel study was to investigate the effect of turbulence intensity, which was a required input for the pressure boundaries. Because no experimental data was available for flow inside the melt-blowing channel, a short parametric study was performed to explore the effects of this unknown value. Using the k-e model with enhanced wall treatment, the turbulence intensity was reduced from 10% to 1%. Although the calculations required over fifty iterations to converge, the results, shown in Figure 4.17, indicated that the reduction in *I* made no visible changes to the flow inside the channel.

LES With Removed Channels

As mentioned previously, the geometry of the air channels was created with dimensions that were typical of those used in industry. Specifically, the channels were given an included angle of 30°. Many other attachments used in industry have an included angle of 60° between the air channels. For this reason, and the sake of comparison, all procedures from here forth were performed separately for a 30° model and a 60° model.

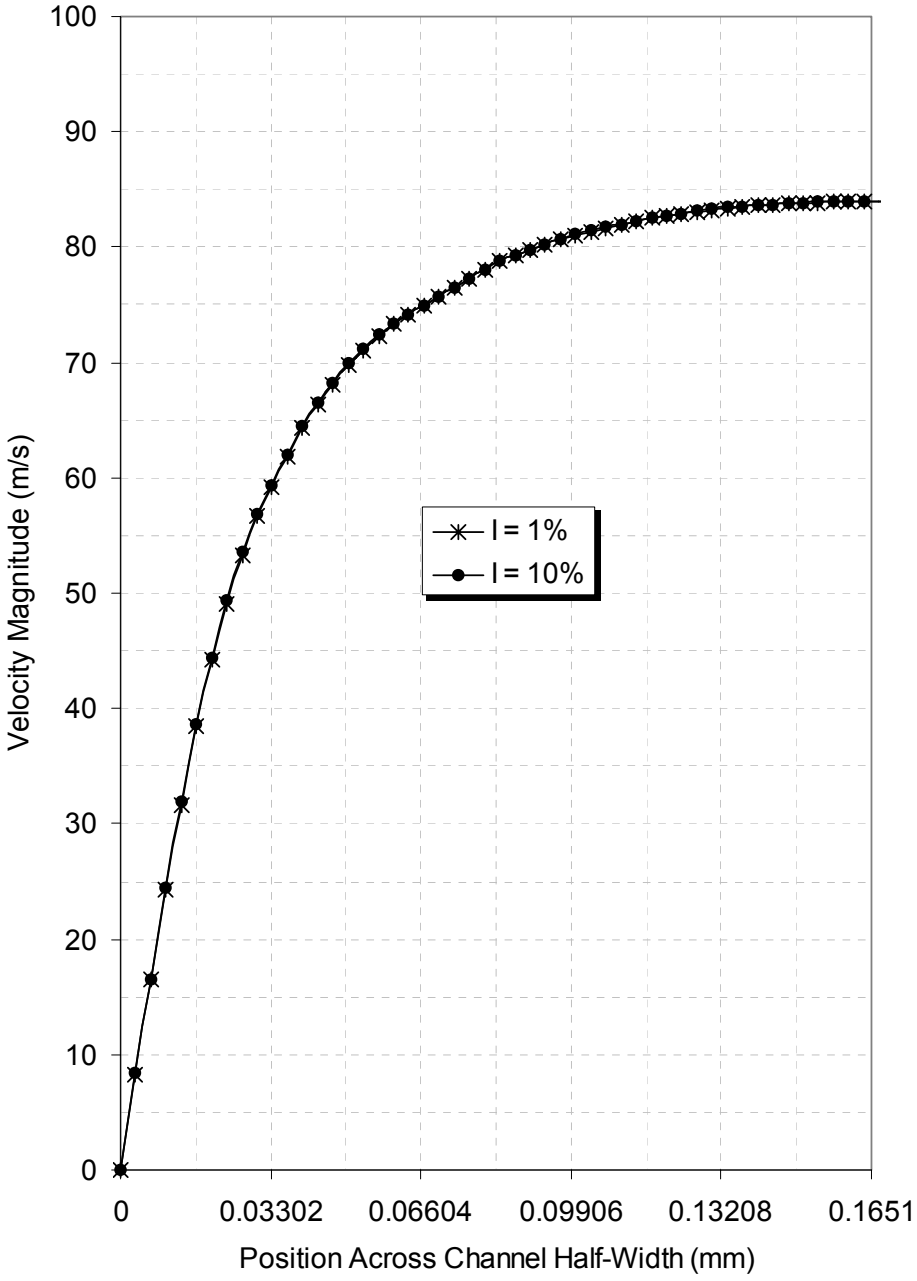


Figure 4.17 Velocity profile comparison with different values of inlet turbulence intensity *I*, using enhanced wall treatment and a refined grid.

Mesh Setup

After a reasonable velocity profile was obtained in the previous section, a new mesh was created to accommodate the new, velocity inlet condition. Although the velocity profile was meant to be placed at the channel exit plane, there was some concern that ignoring the physical corners at the channel exits could reduce the accuracy of the flow field. Therefore, a very small portion of the channel length was kept to account for the corner effect. The massive reduction in channel length permitted several other alterations to be made to the mesh with 2-inch channels. For instance, the dimensions of the flow domain were expanded to a width of two inches and a length of four inches. The mesh density was also increased such that twenty cells spanned the width of each channel exit plane. The mesh of the flow domain was created such that each consecutive node spacing increased by 5% in the y-direction and 0.5% in the x-direction toward the pressure outlets. At the wall boundaries, the mesh was refined in the same fashion as in Figure 4.14. A magnified view of the mesh spacing at the channel exits is shown in Figure 4.18. The completely meshed geometry consisted of approximately 160,000 nodes.

Pre-Run Setup

Before any iterations were performed on the final mesh set, several key locations in the grid were configured to collect velocity data during each run. Using FLUENT's "surface" feature, point monitors were created at even, one-inch intervals along the centerline of the flow domain. Another type of "surface" used to collect more continuous

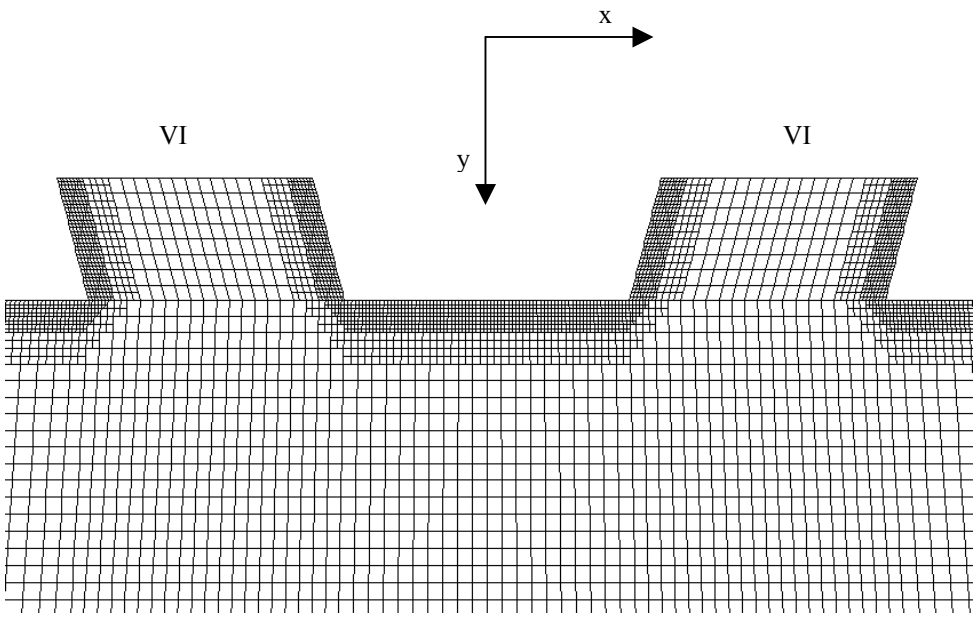


Figure 4.18 Magnified view of the mesh spacing near the channel exits of a new geometric configuration. The channels, which are oriented at with a 30 included angle, were removed to accommodate the new velocity inlets (VI).

data was the line monitor. In this case, a data-collection line, used to report values at each grid point, was created along the entire centerline of the flow domain parallel to the general direction of flow. Additional line monitors were placed at even, one-inch intervals perpendicular to the general direction of the flow (Figure 4.19).

After the mesh was set up properly for data collection, the boundary conditions and operating conditions were set up identically to those from the 2-inch channel model, with the exception of the velocity inlet boundary. For the velocity inlets, the final velocity profile obtained from the previous section was uploaded into FLUENT and placed at the two inlet planes (APPENDIX B). Since the profile contained only the velocity magnitude, the direction had to be manually inserted for each channel. The pressure outlet boundaries were set to a standard atmospheric condition of 0 psig. The wall boundaries did not require any user settings since there was no heat transfer in this model. In fact, the energy equation was turned off completely, eliminating the need to specify the temperature at any location. Since the effect of temperature gradient was reduced significantly, the density was held constant at a value of 1.225 kg/m^3.

Execution of LES

To reduce the overall calculation time, the LES model was initialized with a steady-state, k-epsilon solution. Once the LES model was turned on, an appropriate time step was determined using the method of trial-and-error. As mentioned previously, FLUENT recommended that each time step should require approximately 5-10 iterations to converge within the specified residual criterion. In this case, a time step of $1x10^{-5}$

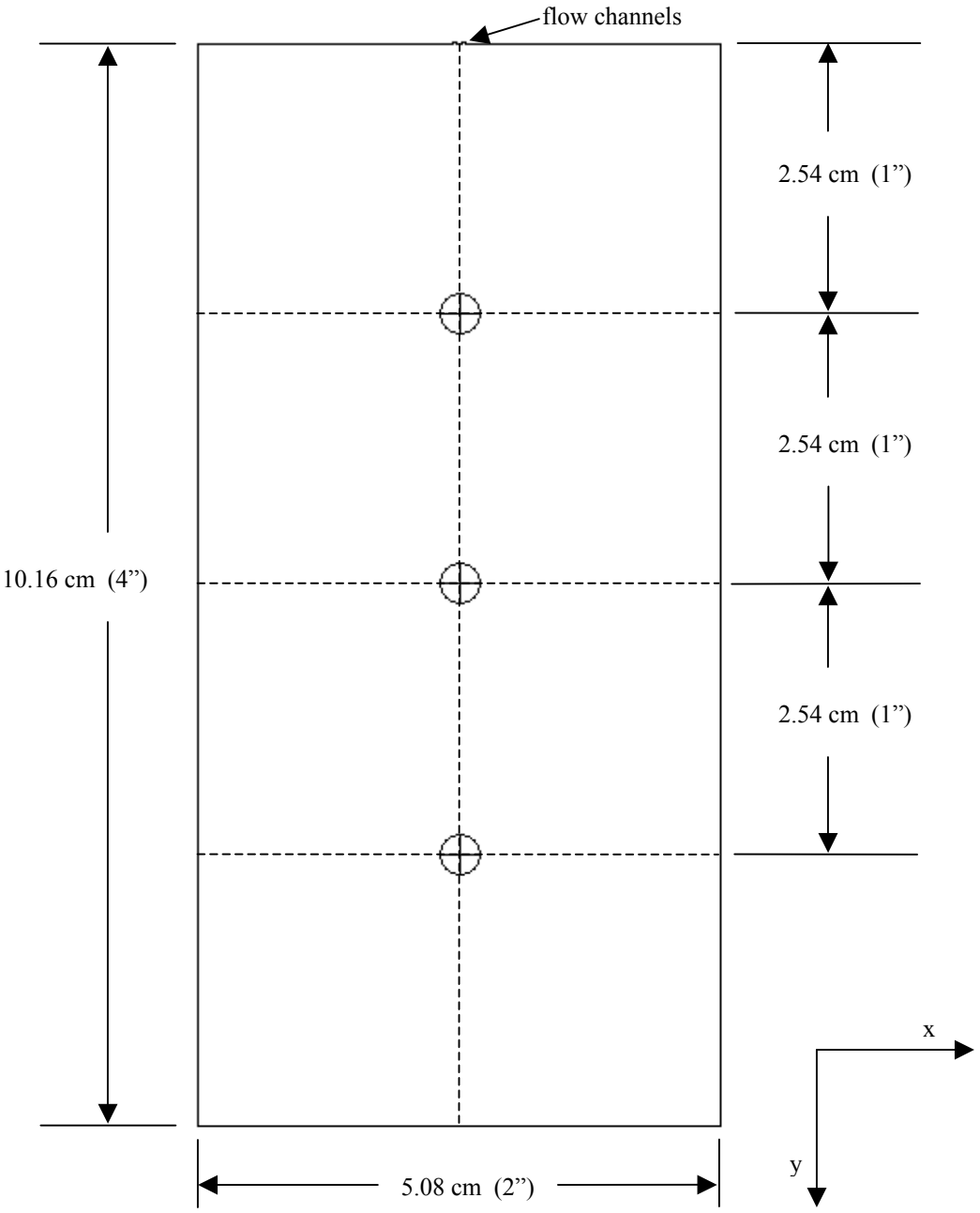


Figure 4.19 Geometric layout of the computational domain with point monitors represented by circles with cross hairs and line monitors represented by dashed lines.

seconds required 7-9 iterations each and was deemed appropriate. To begin the simulation, the command code was written to run the LES model for 20,000 time steps. This initial run allowed the flow to develop into statistically stable turbulence that was free of any numerical transients from the start-up. Once completed, FLUENT's "time-average data sampling" was employed, and the model was reset to run for an additional 80,000 time steps. During this longer simulation, FLUENT recorded time-averaged data as well as time-dependent data. These numerical recordings provided the raw data used in the post-processing portion of the study. FLUENT provided numerous post-processing capabilities; however, the graphical plotting options seemed less abundant than in most popular graphing software. For this reason, the raw data was exported to Microsoft Excel for higher quality plots.

Time-Averaged Data

The time-averaged data, which was recorded for 80,000 time steps, was utilized in three different ways. First, the average velocity was plotted along the length of the domain centerline. This provided a graphical representation of how quickly the flow decelerated after it left the converging channels. This also provided a clear comparison of any differences in flow momentum between the 30° and 60° included angles. For the second set of graphs, the average velocity was plotted along the line surfaces that were oriented perpendicularly to the flow. These velocity profiles were made to investigate how the flow expanded as it moved downstream. Finally, a contour of time-averaged velocity was created in FLUENT.

Time-Dependent Data

The time-dependent monitors were not activated during the first two LES runs due to the immense size of the files. This data was collected in a third simulation in which the LES solution at 100,000 time steps was continued for 20,000 additional time steps. Three point monitors, located at even intervals along the centerline of the flow domain, were used to record the time-dependent velocity data. These data were plotted in Excel to investigate any patterns in magnitude or frequency of vortices as they passed through the point monitors. For additional verification, velocity contours were saved throughout the third run to accompany the time plots. The objective was to match a vortex in the velocity contour with a spike in the velocity vs. time plot.

CFD Comparison With Experimental Measurements

During the computational research of this thesis, Nate McBee, a graduate student at the University of Tennessee, conducted laboratory experiments on a melt-blowing flow field. As a supplement for both research projects, a method was devised to compare the numerical solution and experimental measurements of an average velocity flow field. The plan was to use the velocity profiles from the previous section on a new numerical model that matched the die geometry from the laboratory. Since the actual melt-blowing apparatus was pressure-driven, the pressure valve was to be adjusted until the air velocity matched the numerical solution at a centerline position of one inch. By matching the

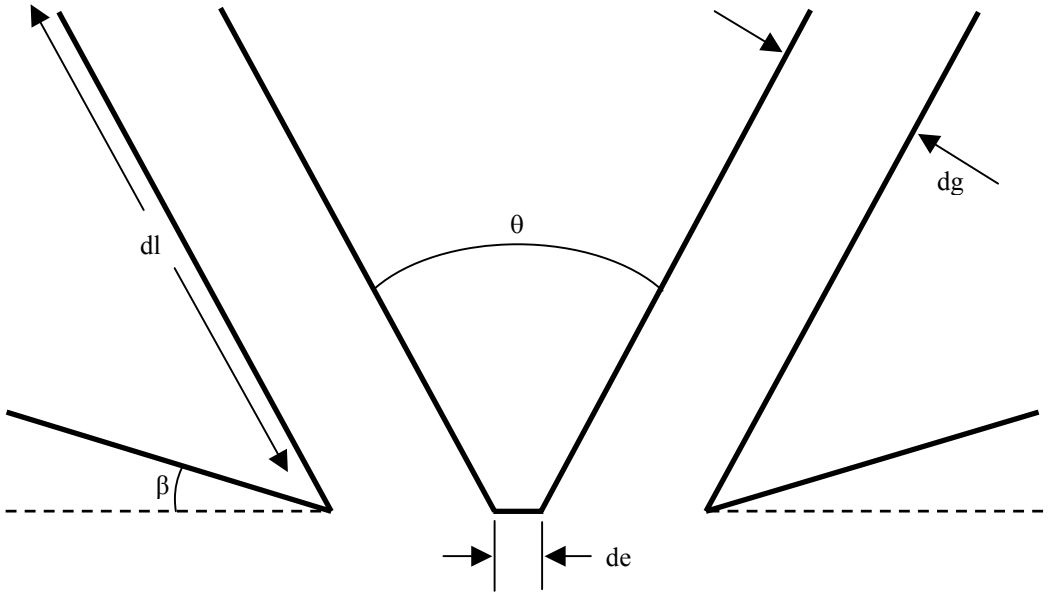
velocities at the same point in the flow domain, both sets of results would be suitable for comparison.

Mesh Setup

In the laboratory, the dimensions of the melt-blowing die were measured by Dr. M. W. Milligan, a professor at the University of Tennessee (Figure 4.20). These measurements were applied to a computational mesh in a fashion similar to the previous section. Specifically, the mesh was created with only a small length of channel for the placement of a velocity profile (Figure 4.21). The grid was refined near the walls to reduce numerical errors near those boundaries. At the face of the die, the grid points were spaced such that 20 cells spanned the width of the die face and 54 cells spanned the width of each channel exit plane. Outside these regions, the grid spaces were increased by increments of 5% along the angled sidewalls and 0.5% in the y-direction toward the pressure outlets. Overall, the mesh contained approximately 190,000 cells. Except for the regions added by the sloped walls, the dimensions of the flow domain were identical to those used in the previous section (Figure 4.22).

Pre-Run Setup

The model was setup for incompressible, isothermal conditions by eliminating the energy equation and setting the density to a constant value of 1.225 kg/m^3. The new mesh was given the same boundary types and velocity profiles that were used in the previous section. The pressure outlet boundaries were set to the standard atmospheric



de =	0.0381 cm (0.015”)
dg =	0.1016 cm (0.040”)
dl =	5.08 cm (2”)
θ =	60°
β =	10°

Figure 4.20 Geometric layout of the melt-blown die used in laboratory experiments at the University of Tennessee.

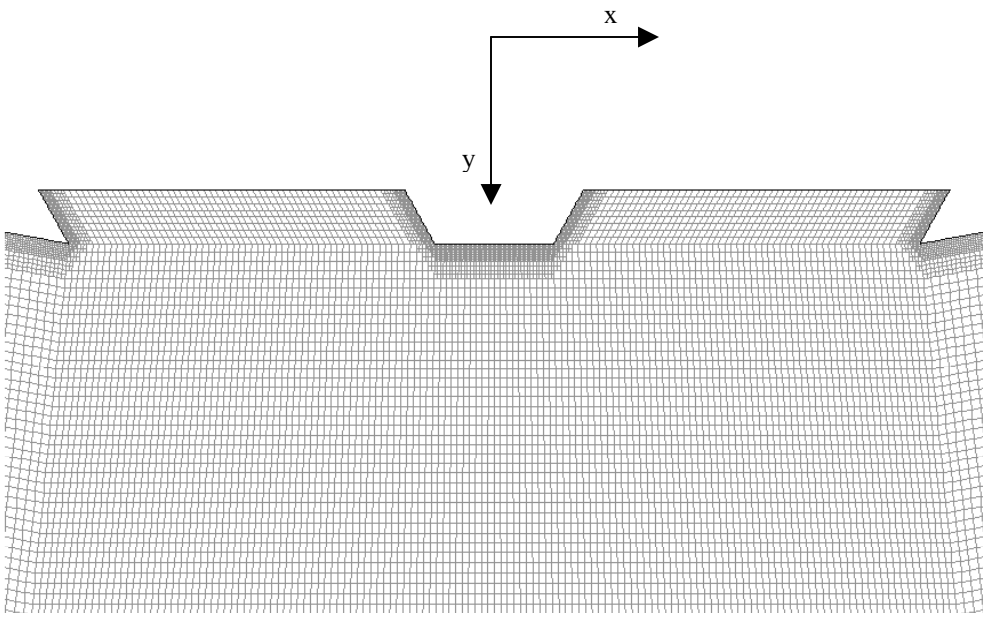


Figure 4.21 Magnified view of the mesh spacing near the channel exits for the geometric configuration in Figure 4.20.

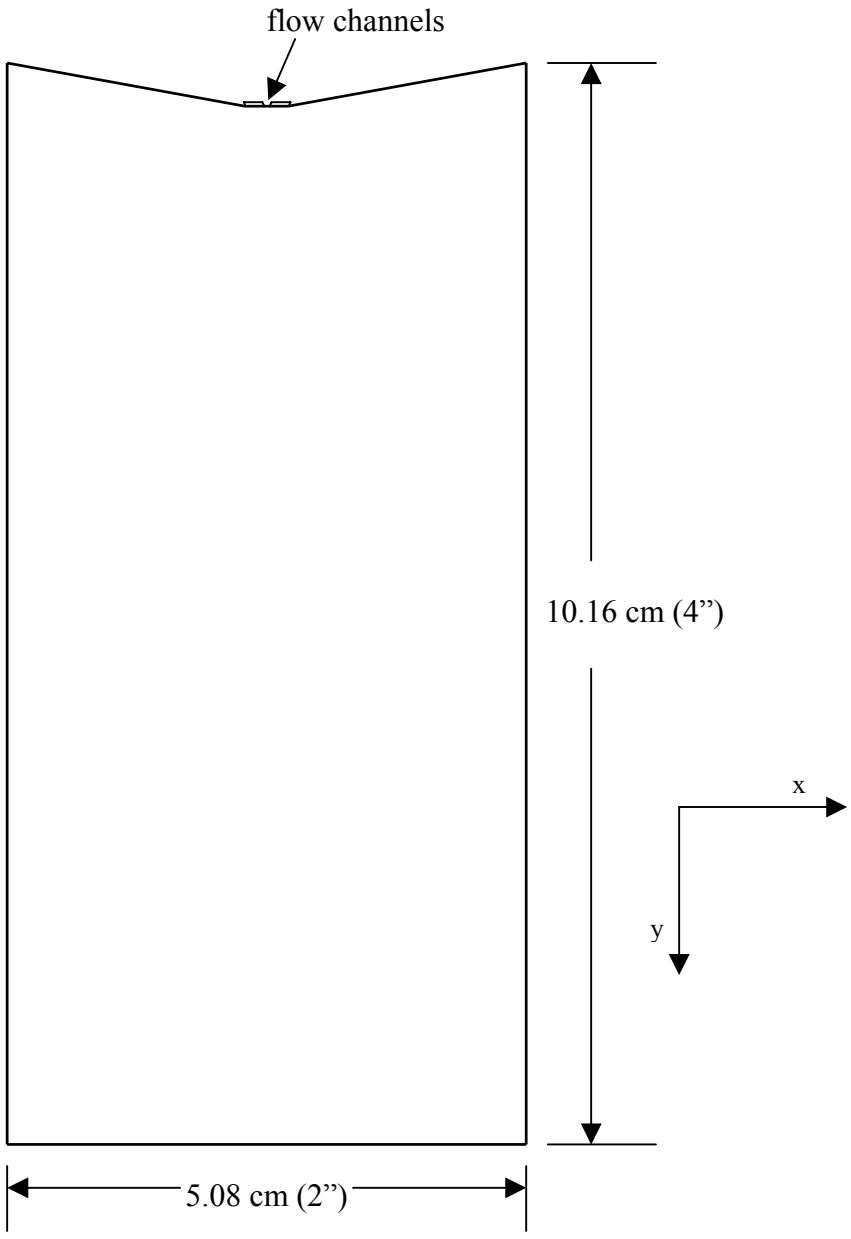


Figure 4.22 Geometric layout of the computational domain used to simulate the flow field generated by the die geometry in Figure 4.20.

condition of 0 psig. The wall boundaries did not require any user settings since there was no heating provided to the die. Due to the additional width of the channels, the velocity profiles were scaled to accommodate the extra space, while retaining the same non-dimensional profile.

Execution of LES

As performed previously, a steady-state, k-epsilon solution was used to initialize the flow field for the LES model. When the LES model was activated, the time-step was adjusted until the model required 5-10 iterations to reach convergence. In this case, the appropriate time-step was $1x10^{-6}$ seconds. The model was allowed to run for 20,000 time steps before activating the time-averaging feature so that numerical transients did not affect the averages. Once the averaging feature was turned on, the model ran for 80,000 additional time steps until the flow field reached statistically stable averages. Afterwards, the results were exported into Microsoft Excel for further study.

CHAPTER V

RESULTS

This chapter presents the results that were obtained for the fourth and fifth sections of chapter four entitled: (4) LES With Removed Channels and (5) CFD Comparison With Experimental Results. The first section compares the time-averaged and time-dependent velocity flow fields for two different jet angles of 30° and 60°. The second section compares a time-averaged, computational flow field with experimental measurements taken in a laboratory while running similar flow conditions. The third section of this chapter, "Animations of Velocity Contours," discusses movies that were made from sequences of velocity contours for the model geometries used in this section.

LES With Removed Channels

In this section the results were divided into two primary parts: (1) Time-Averaged Results and (2) Time-Dependent Results. In each part, the 30° model and 60° model were examined separately before making a comparison between the two.

Time-Averaged Results

The time-averaged results in this section were collected over the span of 80,000 time steps of $1x10^{-5}$ seconds each. FLUENT labeled this feature as "Data Sampling for

Time Statistics." As mentioned in the previous chapter, the sampling feature was activated after an initial computation of 20,000 time steps, which prevented numerical transients from entering into the averages.

30° Model

The mean centerline velocity for the 30° model was plotted in Figure 5.1. The velocity was zero at a position of 0 cm, which represented the no-slip wall boundary of the die face. Immediately downstream of the die wall, the velocity experienced a rapid acceleration to a peak value of 68 m/s, which occurred at a centerline position of 0.2 cm and was a 17 m/s decrease from the peak velocity at the channel exits. This peak position at 0.2 cm is where the two jets converged into each other. Beyond this point, the centerline velocity experienced a strong deceleration up to 4 cm in the downstream direction. After 4 cm, the centerline velocity approached a steady value of approximately 6 m/s. There was another indication of a slight deceleration beyond nine centimeters. However, the results in this region were less meaningful, due to the close proximity of the exit pressure boundary. In Figure 5.2, three velocity profiles were plotted at different positions in the downstream direction to illustrate the expansion of the flow. The center point (0 cm) in each of these profiles corresponded to the velocity plotted in Figure 5.1. These center velocity points matched up well with those from the previous figure. The line monitor that was positioned one inch (2.54 cm) into the flow domain recorded a smooth velocity profile with a peak, centerline value close to 13 m/s. The shape of this curve indicated that the two jets had fully merged by the time the flow traveled one inch

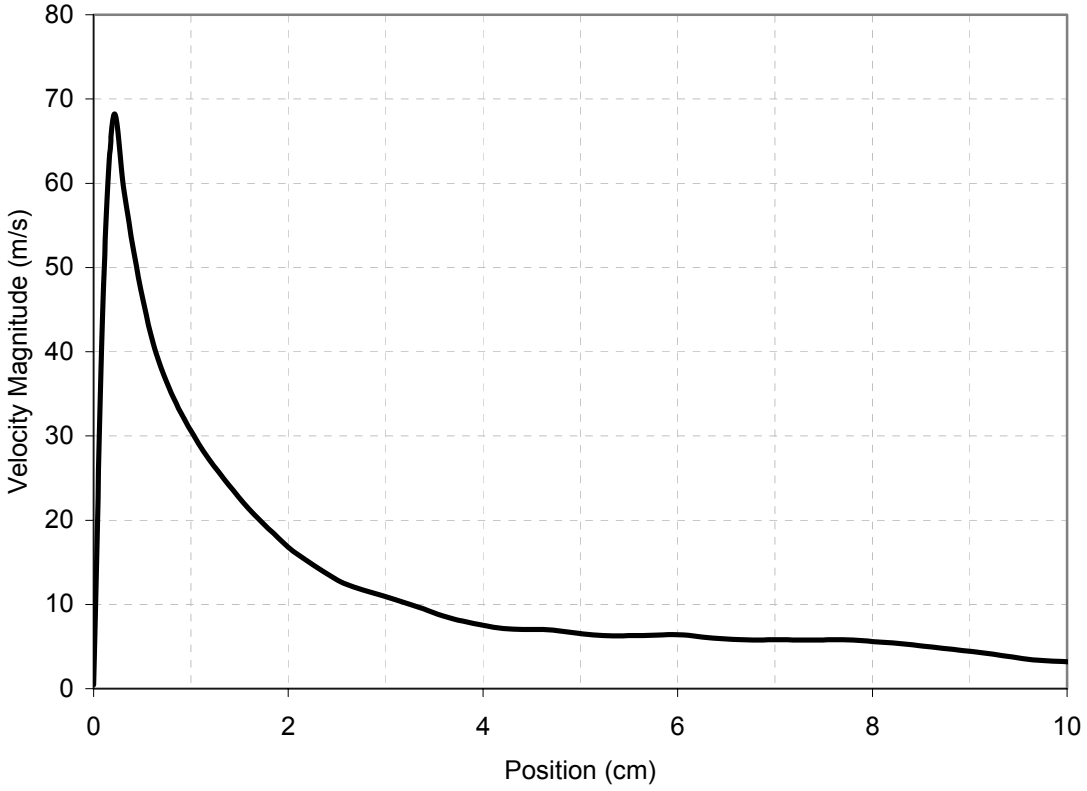


Figure 5.1 Time-averaged centerline velocity with a 30° included angle between channels.

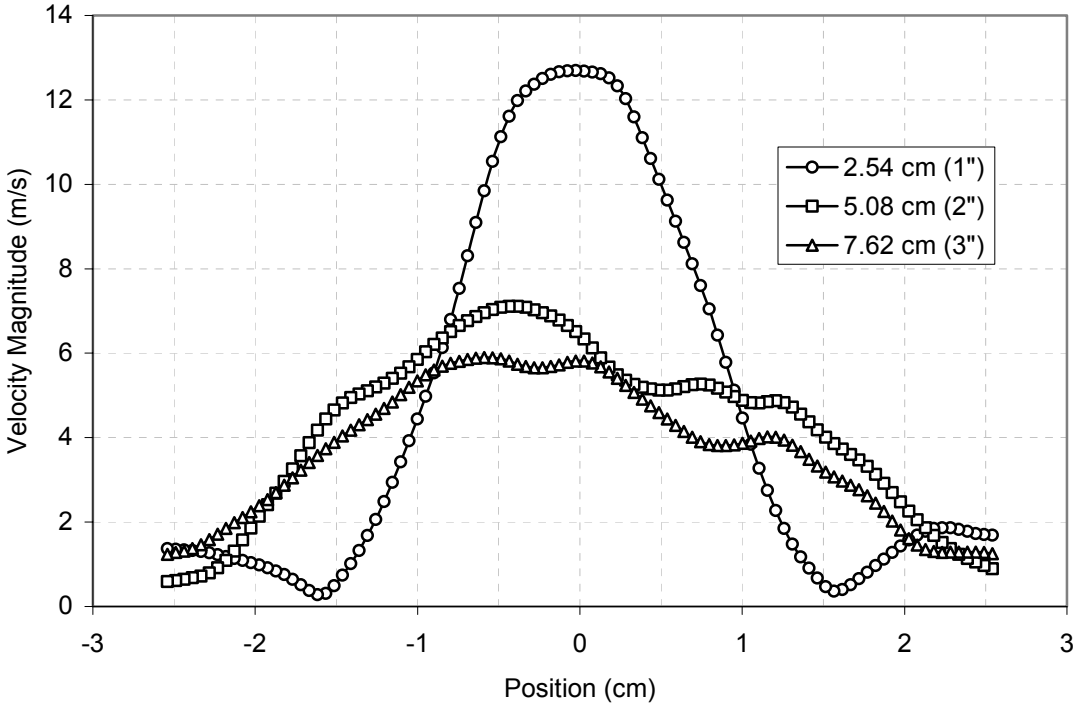


Figure 5.2 Time-averaged velocity profiles located at different positions downstream of the channel exit planes, which are oriented with a 30° included angle.

downstream. The other two velocity profiles, which were located further downstream, were very similar in shape and magnitude. This result indicated that the average velocity experienced very little change this far downstream, which was also inferred from Figure 5.1. When all three profiles were compared, an interesting observation was made concerning the smoothness to the curves. Unlike the one-inch profile, which was smooth and symmetrical, the other two profiles appeared to be more jagged and less symmetrical in nature. Since all three profiles were averaged over the same time period, it seemed possible that these differences were caused by random eddies in the flow. If this theory was correct, it meant that the time-averaging feature might have required more data collection in order to produce smoother velocity profiles in the latter region of the flow domain. Another possibility was that the periodic nature of the flow would never permit the time-averaged velocities to steady out. In any case, neither theory could be supported without further computational time averaging. In addition to time-averaged line plots, the mean velocity contours were plotted over the entire domain (Figure 5.3). The contour lines illustrated the basic shape of expansion that occurred inside the flow domain. In this figure, each contour line represented a change in velocity of 3.4 m/s. Similar to the observations in previous figures, the contour lines appeared to lose their smoothness and symmetry as they neared the exit boundaries. In Figure 5.4, the top region was magnified to illustrate the line monitor that was placed one inch (2.54 cm) downstream of the channel exits. This represented the line in which data was averaged for the first velocity profile in Figure 5.2. The contour lines in this figure represented a change in velocity of 1.4 m/s.

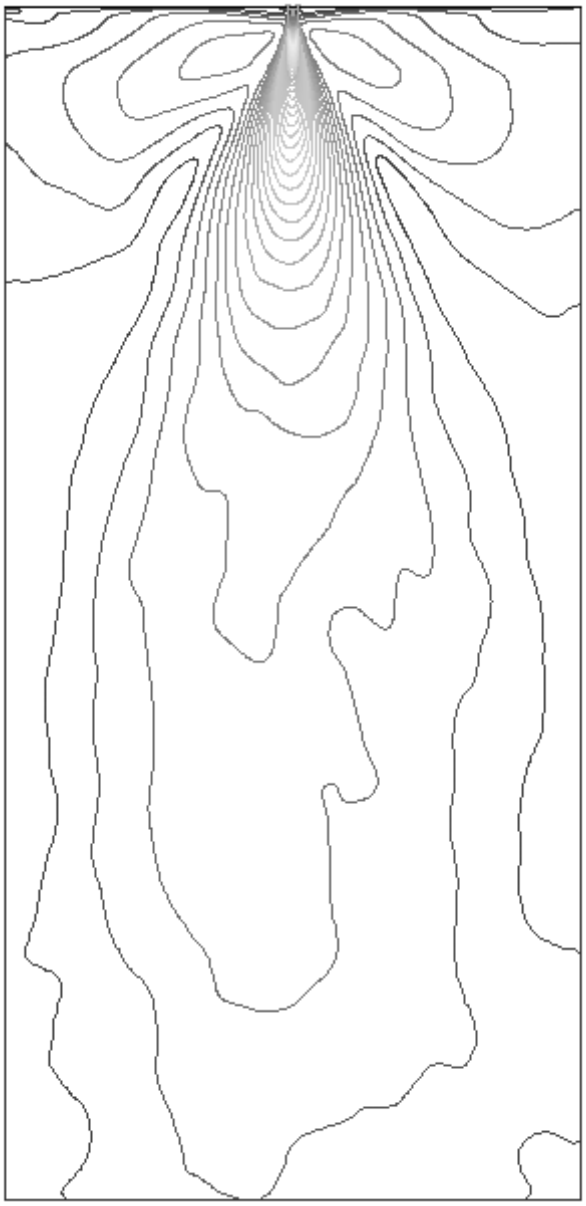


Figure 5.3 Contours of time-averaged velocity magnitude with a 30° included angle between channels. Each contour line represents a change in velocity of 3.4 m/s.

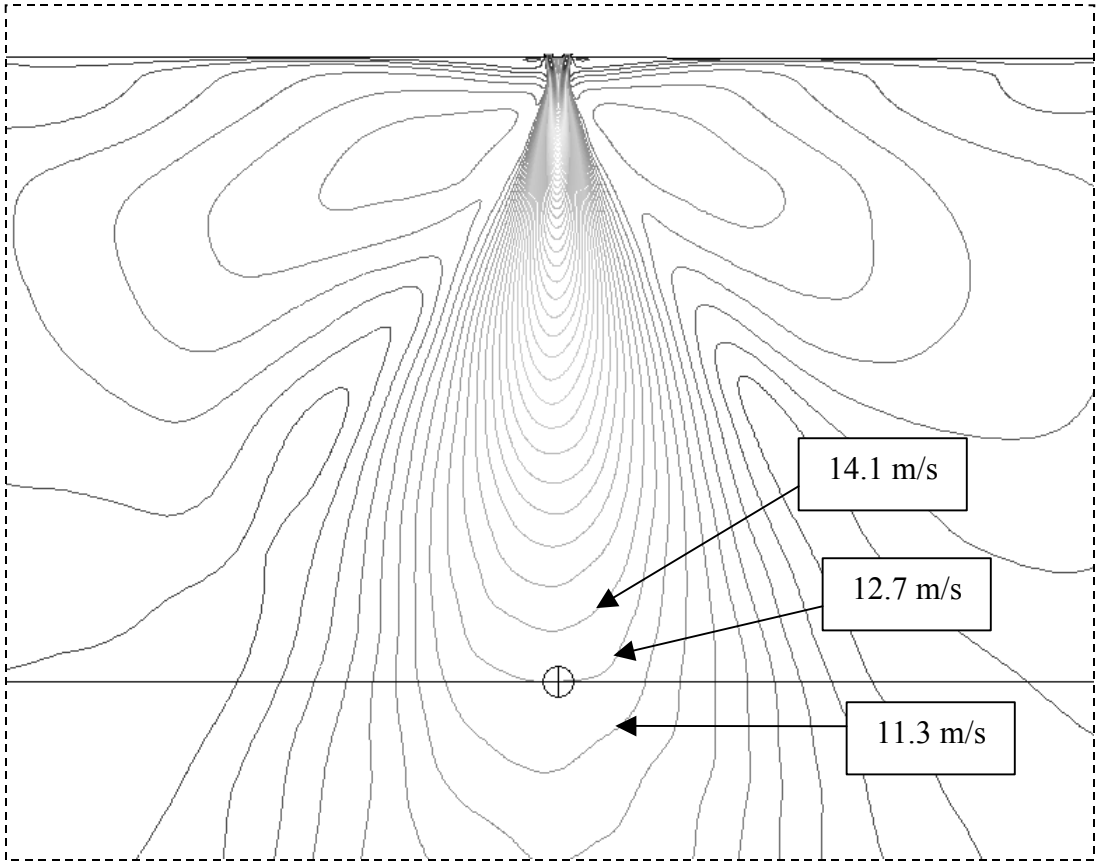


Figure 5.4 Magnified contours of time-averaged velocity magnitude with a 30° included angle between channels. Each contour line represents a change in velocity of 1.4 m/s.

60° Model

The mean centerline velocity for the 60° model (Figure 5.5) exhibited another rapid deceleration inside the first four centimeters of the flow domain. There was a sharp spike in the velocity curve near 0.2 cm, where the centerline velocity peaked near 73 m/s. After four centimeters, the centerline velocity experienced a relatively steady decline to approximately 4 m/s at the exit boundary. In Figure 5.6, three velocity profiles were plotted at different positions in the downstream direction. The line monitor that was positioned one inch (2.54 cm) into the flow domain recorded a fairly sharp velocity profile, which peaked near 14.5 m/s. The other two profiles, located at 2 inches and 3 inches downstream, seemed wavy with random changes in slope. As mentioned in the previous section, it seemed possible that these profiles would smooth out with an increased amount of simulation time. In Figure 5.7, the mean velocity contours were plotted over the entire domain and illustrated the general shape of flow expansion. The upper portion of the domain was magnified to show the line monitor that was located one inch from the channel exits (Figure 5.8). In this figure, the contours represented a change in velocity of 1.2 m/s. Upon closer examination of area near the line monitor's center, it seemed that the contours were shaped inconsistently down the centerline of the domain. Again, this indicated that more data were needed to develop a smoother, average flow field.

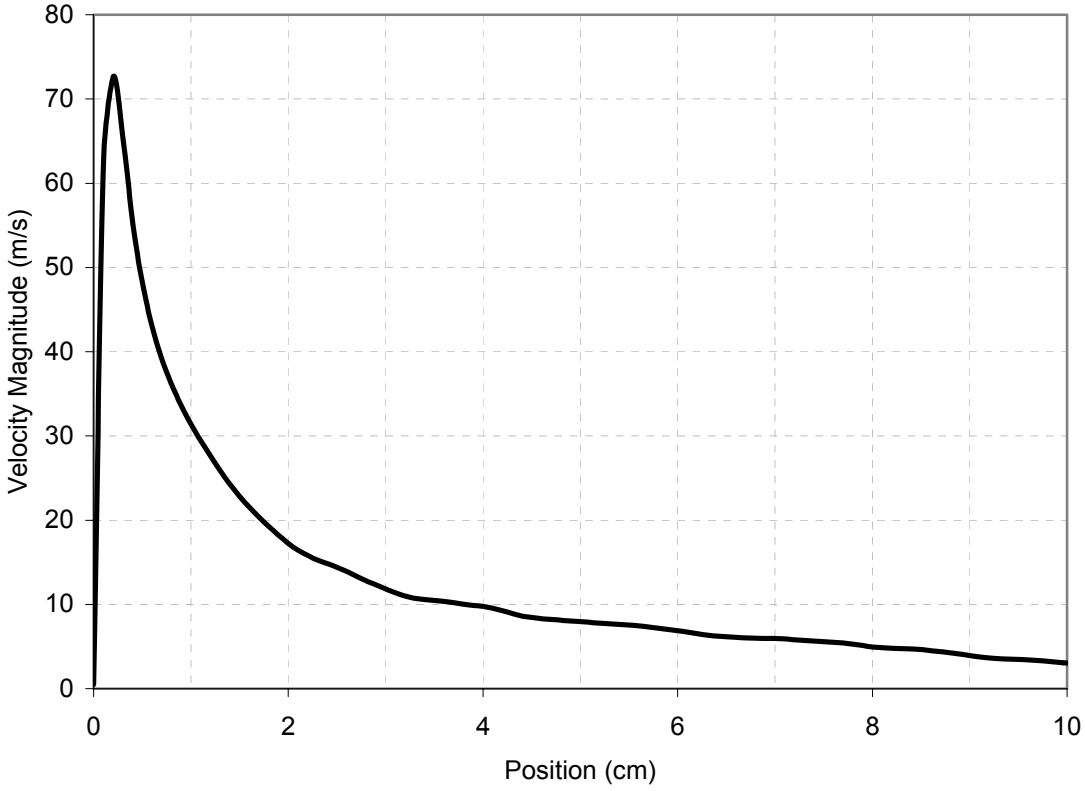


Figure 5.5 Time-averaged centerline velocity with a 60° included angle between channels.

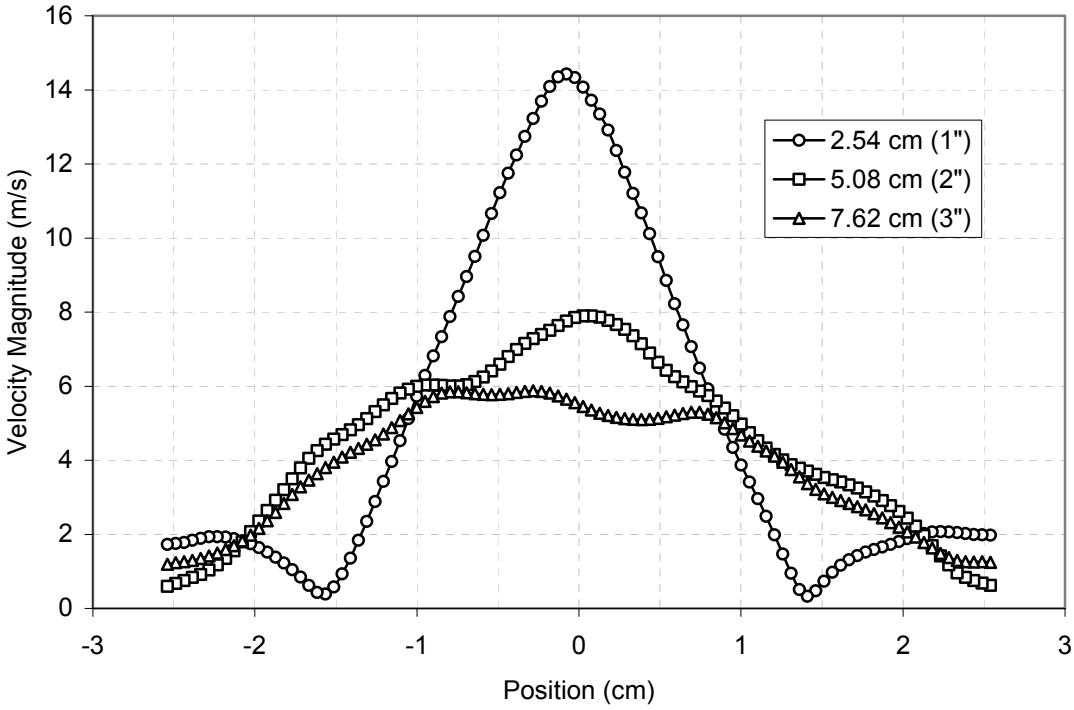


Figure 5.6 Time-averaged velocity profiles located at different positions downstream of the channel exit planes, which are oriented with a 60° included angle.

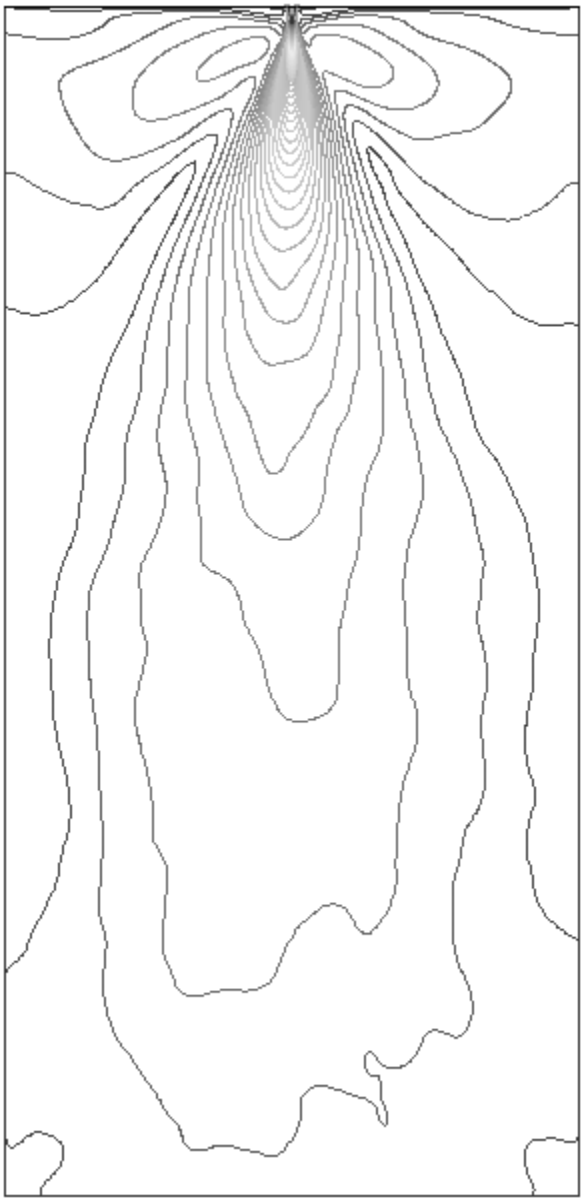


Figure 5.7 Contours of time-averaged velocity magnitude with a 60° included angle between channels. Each contour line represents a change in velocity of 3.4 m/s.

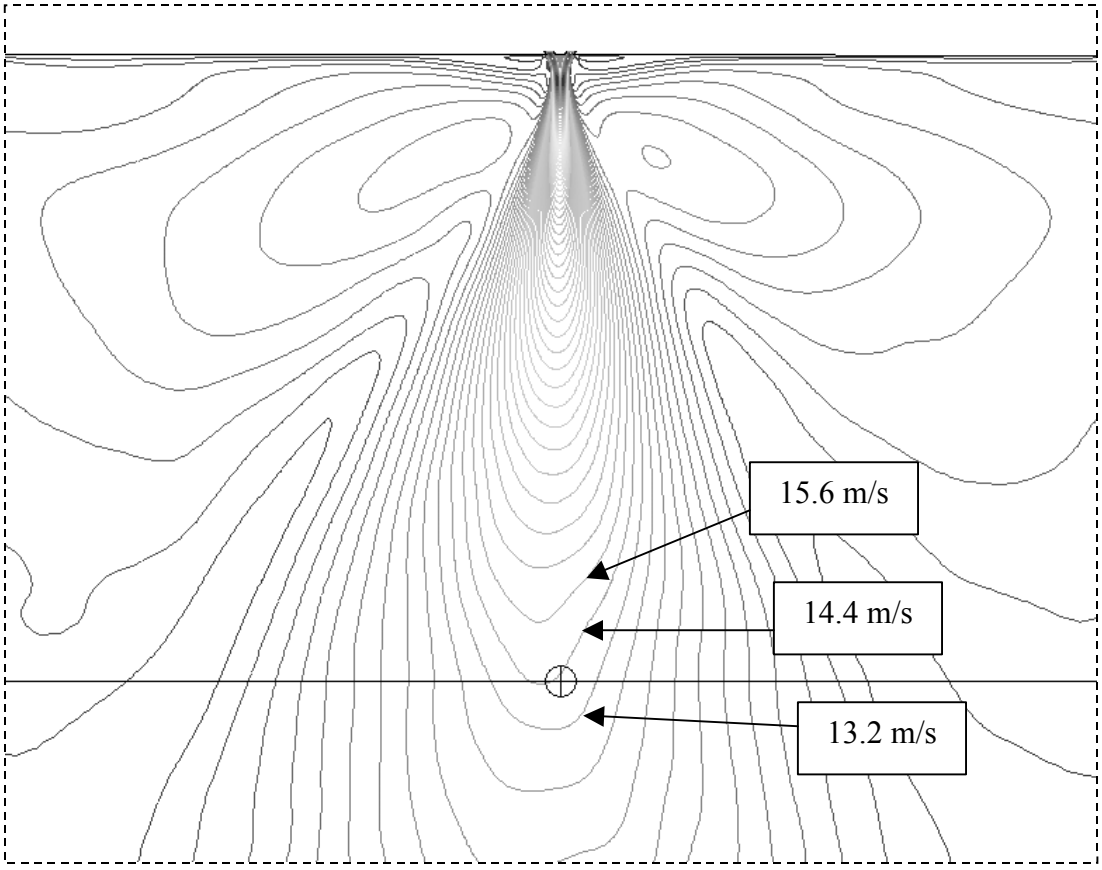


Figure 5.8 Magnified contours of time-averaged velocity magnitude with a 60° included angle between channels. Each contour line represents a change in velocity of 1.2 m/s.

Comparison Between 30° and 60° Models

A comparison between the 30° and 60° models indicated very little difference in time-averaged centerline velocity curves (Figure 5.9). Because of the increased angle, the 60° jets converged at a slightly earlier position than the 30° jets. This caused the 60° centerline velocity to increase more rapidly than the 30° centerline velocity. In addition, the 60° jets achieved a higher maximum centerline velocity near 0.2 centimeters. From this point forth, it seemed that the 60° jets did not decelerate as rapidly as the 30° jets. It was unclear if the difference in deceleration rate was a meaningful result, or the consequence of insufficient time-averaged data. As a final comparison, the one-inch velocity profiles were plotted together in Figure 5.10. Not only was the 60° centerline magnitude higher, but the 60° profile was shaped more sharply. Both dissimilarities seemed to be attributed to the difference in convergence angle. Although, as mentioned previously, it remained unclear how much of these differences would decrease with longer run times.

Time-Dependent Results

The time-dependent results in this section were collected over the span of 20,000 time steps of $1x10^{-5}$ seconds each. Velocity vs. time data were collected at three locations in the flow domain using point monitors. These monitors were placed downstream of the channel exits at one inch, two inches, and three inches along the domain centerline. As a supplementary visual aid, velocity contours were plotted to

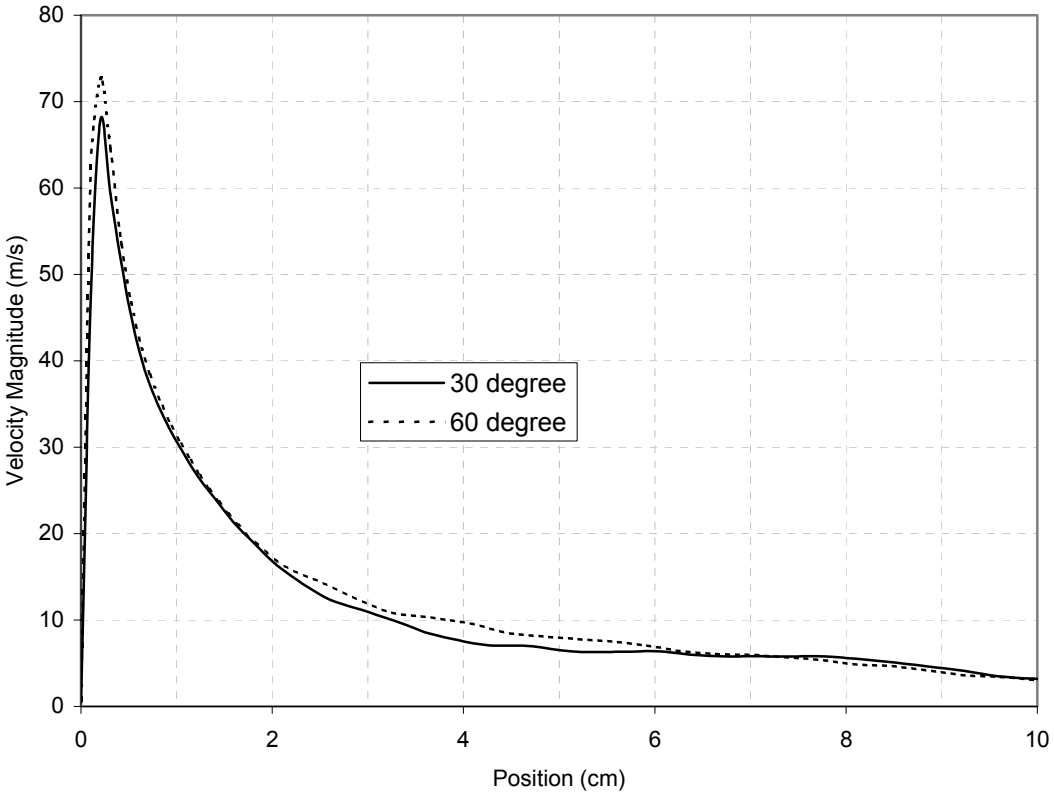


Figure 5.9 Comparison of time-averaged centerline velocity for the 30° and 60° models.

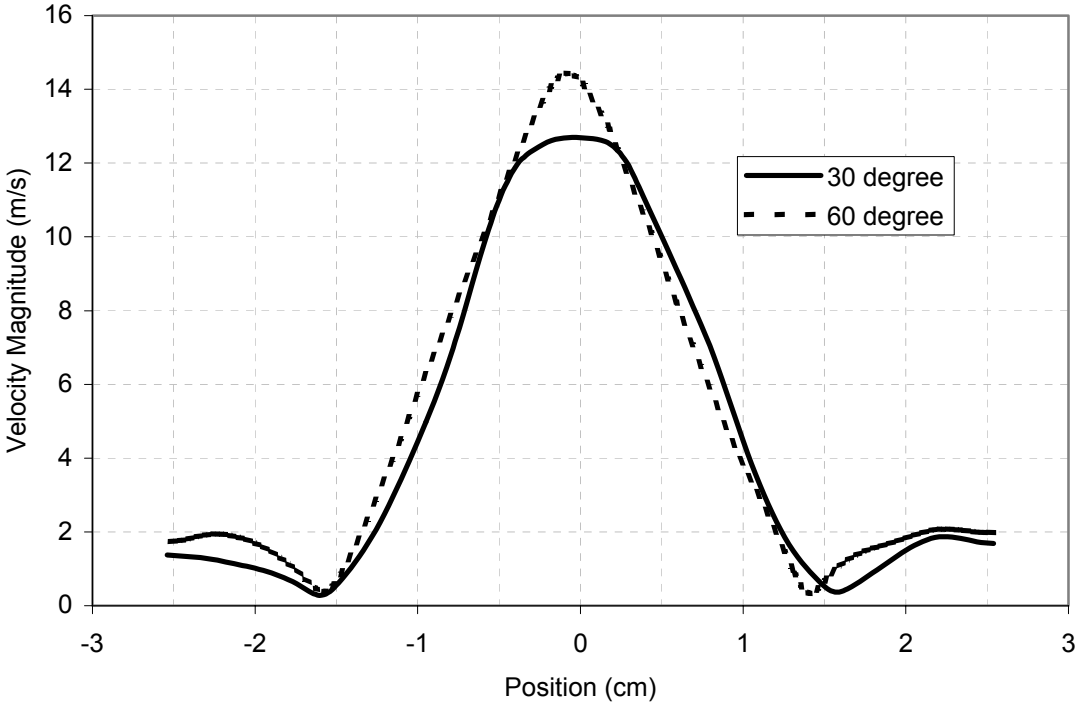


Figure 5.10 Comparison of time-averaged velocity profiles at 2.54 cm (1") downstream of the channel exits for the 30° and 60° models.

show the position of eddy structures relative to the point monitors. The purpose of analyzing time-dependent, velocity data was to identify any repeating patterns in magnitude or frequency of eddies that passed through the data monitors. In addition, the velocity contours were used to confirm the presence of vortices that appeared in the time plots.

30° Model

In Figure 5.11, the velocity magnitude was plotted as a function of time at a centerline distance of 2.54 cm (1") from the channel exits. At one inch, the time-averaged velocity was approximately 13 m/s (Figure 5.2). The velocity magnitude at this position fluctuated as high as 120 m/s, nearly 10 times the average value. The velocity fluctuations decreased in both frequency and magnitude for positions further downstream (Figure 5.12 and Figure 5.13). As the large, vortex structures traveled downstream, they dissipated energy to the smaller scales of motion. This energy dissipation caused a reduction in both rotational velocity and translational velocity. The reduction in rotational velocity resulted in lower spikes of velocity magnitude, while the reduction in translational velocity caused the reduction in frequency.

Other than the energy dissipation, the random nature of the fluctuations made it difficult to distinguish any obvious natural frequencies in the system. However, in Figure 5.13, there seemed to be a cluster of velocity peaks with consistent spacing beginning around 1.09 seconds. A quick measurement of these spaces indicated that the spikes recurred with an approximate frequency of 120 Hz. As a short comparison, the same

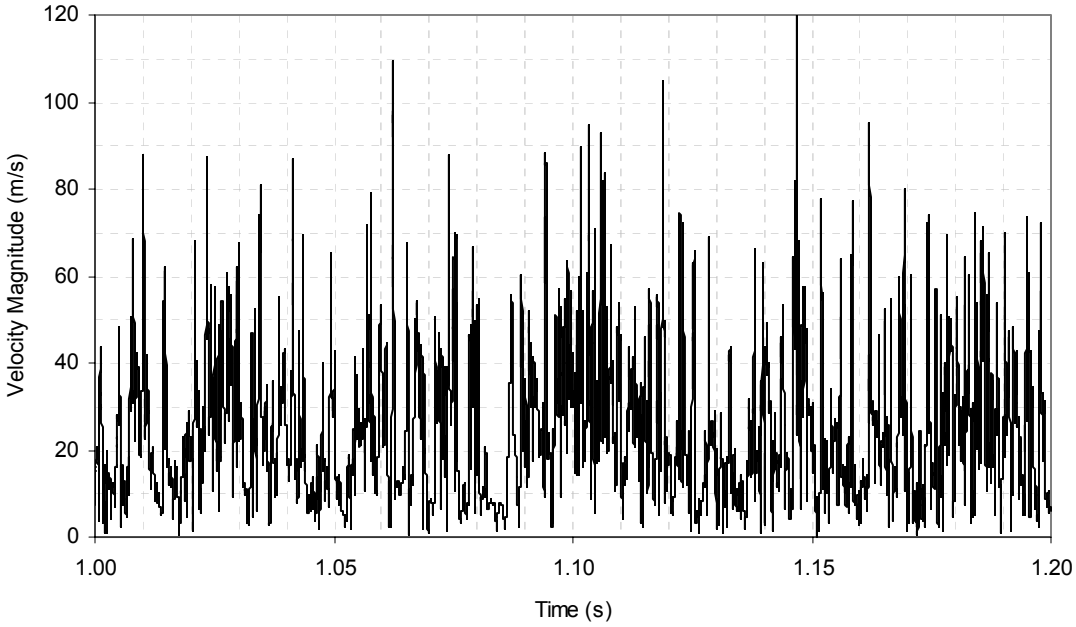


Figure 5.11 Time-dependent velocity at 2.54 cm (1") downstream of the channel exits for the 30° model, shown with 0.2 total seconds of run time.

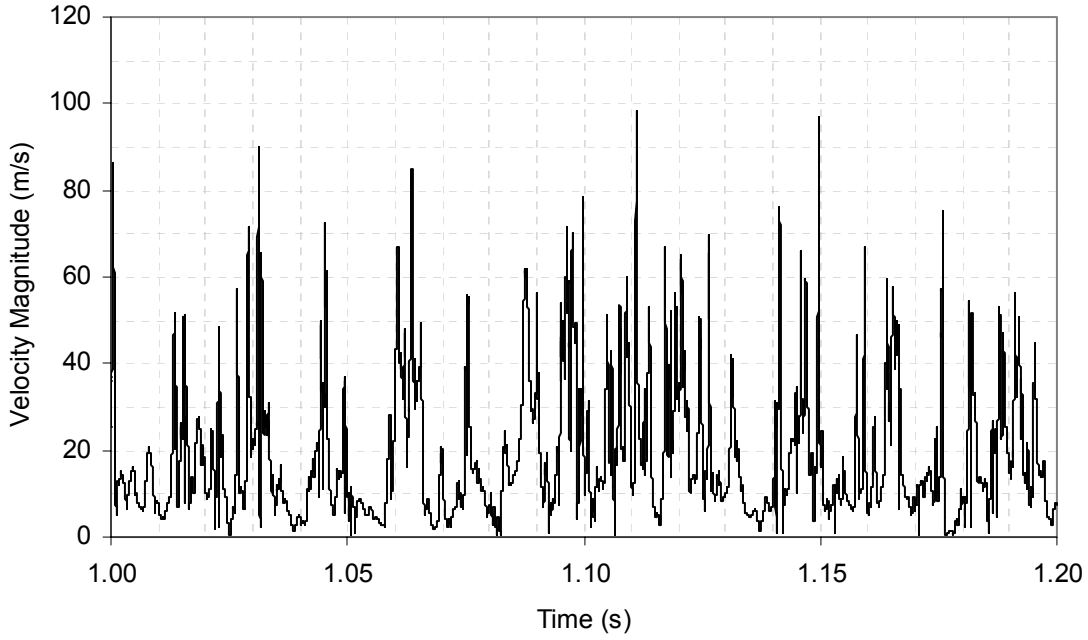


Figure 5.12 Time-dependent velocity at 5.08 cm (2") downstream of the channel exits for the 30° model, shown with 0.2 total seconds of run time.

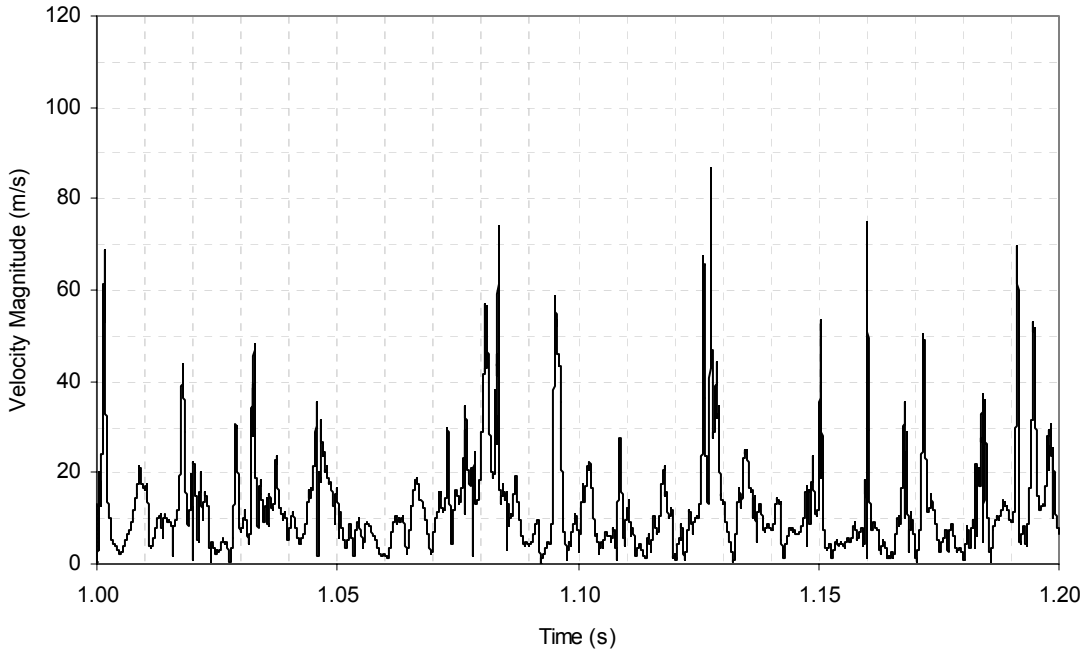


Figure 5.13 Time-dependent velocity at 7.62 cm (3") downstream of the channel exits for the 30° model, shown with 0.2 total seconds of run time.

approach was applied to the data collected from a point further upstream, where the frequencies were expected to be higher due to higher centerline velocities. For easier viewing, Figure 5.11 was magnified to only show data between 1.15 seconds and 1.20 seconds (Figure 5.14). Once again, there seemed to be clusters of repeatable velocity spikes separated by time periods of reduced activity. A quick analysis of these clusters indicated a possible trend of velocity spikes occurring at about 670 Hz. This result indicated that not only did the magnitude of the fluctuations decrease in the downstream positions, but the frequency did as well. It should be noted that the frequencies measured at these two positions were adequate only for qualitative, comparison purposes. Since only small clusters of data were measured, the results would not be appropriate for quantitative predictions.

The characteristics of these results were partially contributed to the random dispersion of the vortex structures. A velocity contour (Figure 5.15) illustrated how the vortices dispersed in all directions, instead of passing through the point monitors with any orderly fashion. This contour was produced at a run time of 1.01 seconds, and represented the instantaneous velocity field at that time. At this particular time, a vortex structure was seen passing through the first point monitor. The presence of this structure was verified by locating a local maximum in Figure 5.11 at a time of 1.01 seconds.

60° Model

For the 60° model, the point monitors recorded similar unpredictable, random velocity fluctuations. At the one-inch monitor (Figure 5.16), the velocity fluctuated as

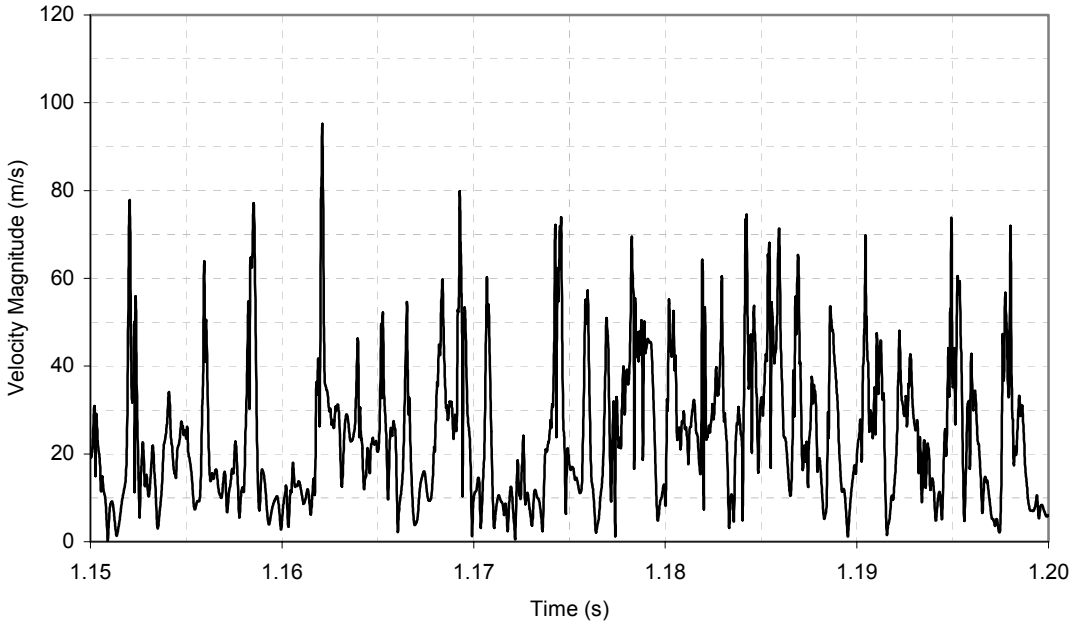


Figure 5.14 Time-dependent velocity at 2.54 cm (1") downstream of the channel exits for the 30° model, shown with 0.05 total seconds of run time.

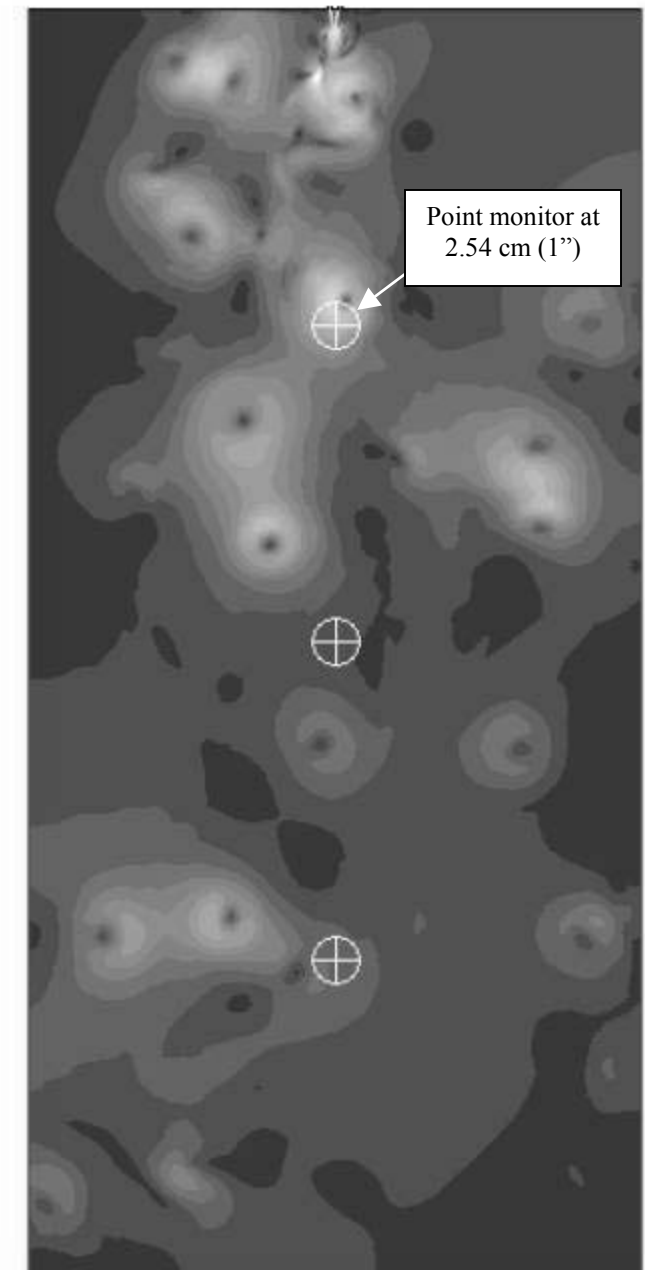


Figure 5.15 Contour of instantaneous velocity after a run time of 1.01 seconds for the 30° model.

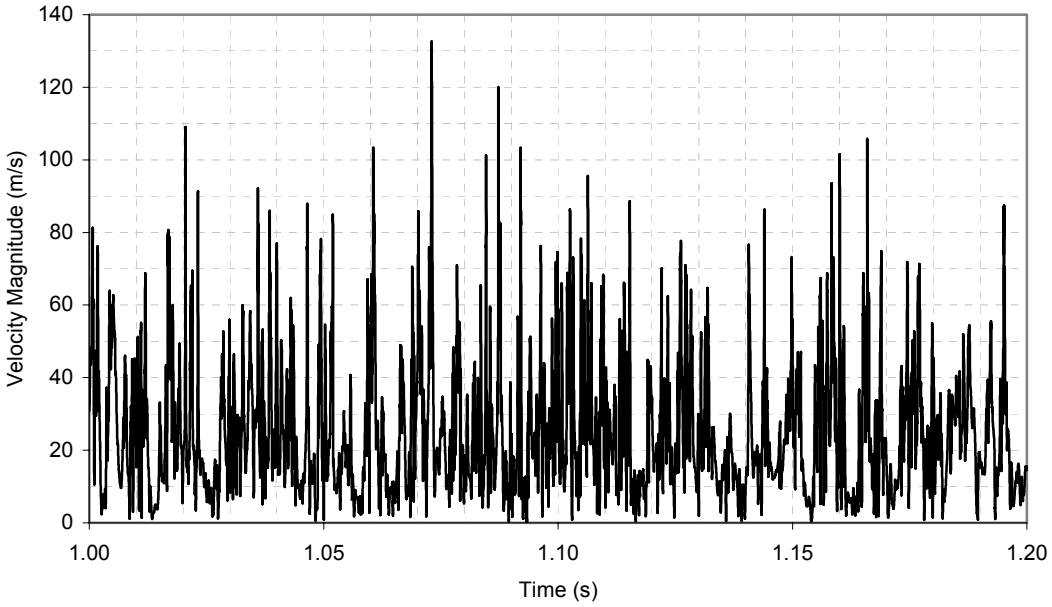


Figure 5.16 Time-dependent velocity at 2.54 cm (1") downstream of the channel exits for the 60° model, shown with 0.2 total seconds of run time.

high as 132 m/s, which was nearly 10 times the time-averaged value at that location. Further downstream, the velocity fluctuations reduced in magnitude and frequency, yet were still sporadic in nature (Figures 5.17 and 5.18). The reductions in magnitude and frequency were the result of energy dissipation. As the large vortex structures traveled further downstream, they lost energy to smaller scales of motion. For equal time intervals, fewer peaks occurred at each subsequent point monitor, which indicated a reduction in the translational velocity of the vortices. Similarly, as the monitor position moved further downstream, the velocity peaks reduced in magnitude. This trend indicated a reduction in the rotational velocity of the vortices, which was closely related to their overall strength.

As performed previously with the data from the 30° model, a cluster of velocity spikes were analyzed in Figure 5.18 to make a rough estimation of the governing frequency. The velocity spikes at the three-inch downstream position recurred at approximately 240 Hz. A comparative analysis was performed for the one-inch position further upstream (Figure 5.19) using a magnified section from Figure 5.16. These spikes recurred with a frequency near 730 Hz. The frequency was higher in the upstream position due to higher translational velocities of the vortex structures. As mentioned previously, these measurements were only used for a qualitative comparison. A quantitative prediction could not be substantiated by the methods described here.

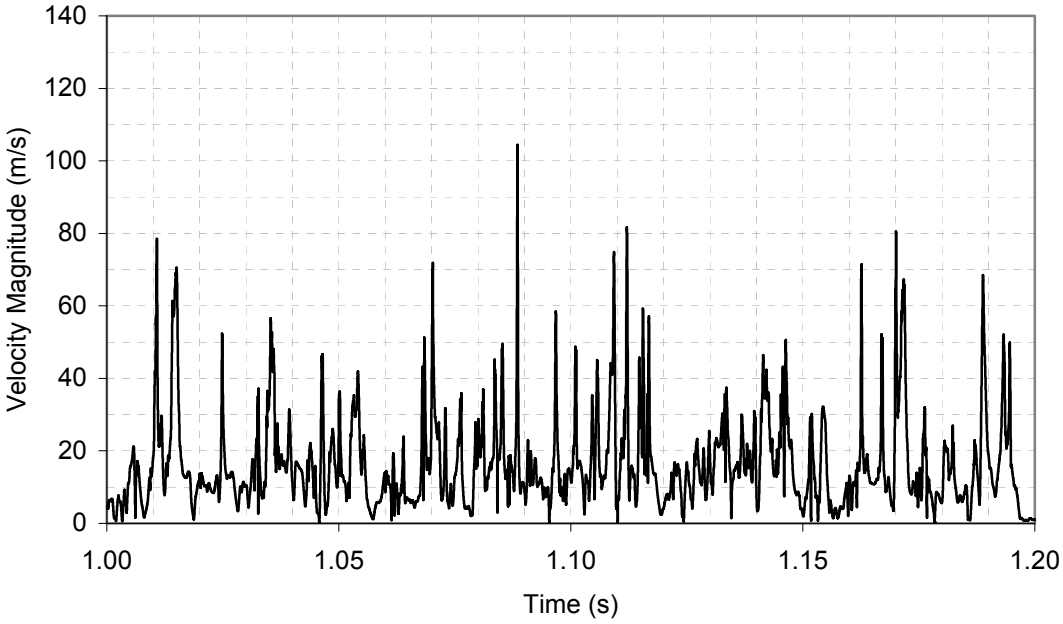


Figure 5.17 Time-dependent velocity at 5.08 cm (2") downstream of the channel exits for the 60° model, shown with 0.2 total seconds of run time.

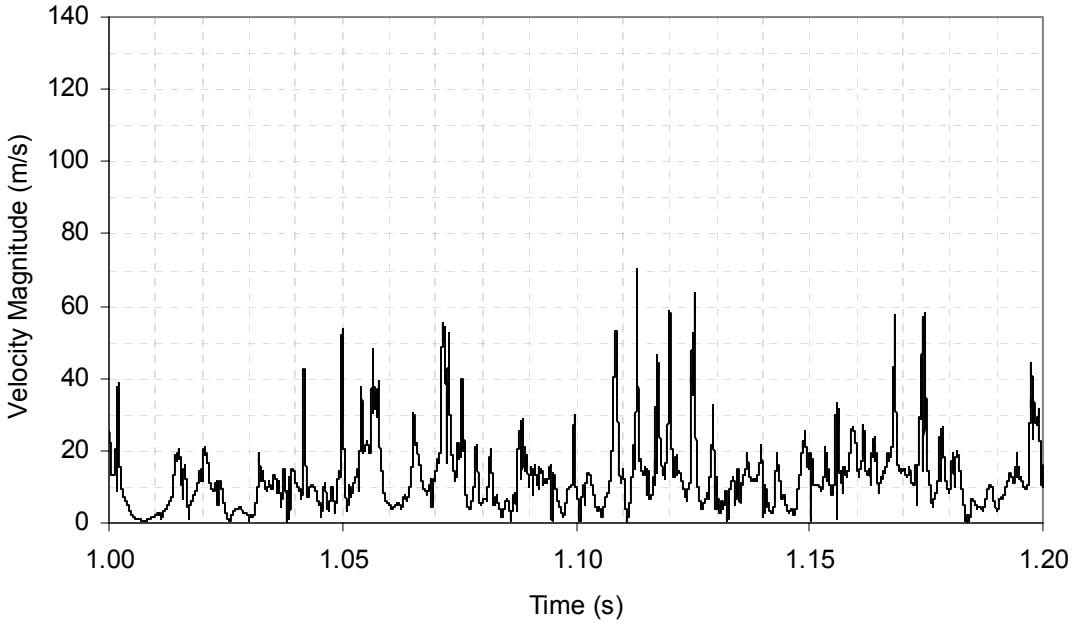


Figure 5.18 Time-dependent velocity at 7.62 cm (3") downstream of the channel exits for the 60° model, shown with 0.2 total seconds of run time.

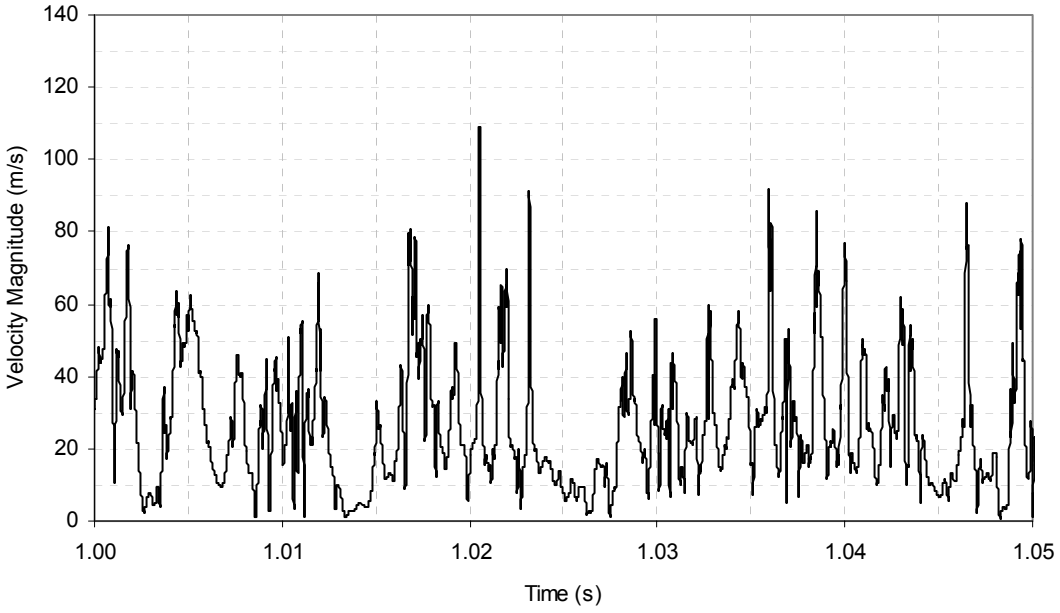


Figure 5.19 Time-dependent velocity at 2.54 cm (1") downstream of the channel exits for the 60° model, shown with 0.05 total seconds of run time.

Comparison Between 30° and 60° Models

A simple method was used to compare the relative intensity of vortex structures between the different models. In this method, the number of times that a peak surpassed 80 m/s was counted in both Figure 5.11 and Figure 5.16, which plotted the velocity data at one inch downstream. For an additional comparison, the count was repeated for peaks that surpassed 100 m/s. Over the span of 0.2 seconds, the figures indicated that the velocity spiked over 80 m/s a total of 16 times for the 30° model and 22 times for the 60° model. Similarly, the velocity spiked over 100 m/s a total of 3 times for the 30° model and 8 times for the 60° model. Consequently, the larger angle between jets caused more of the high-magnitude vortices to pass through the point monitor. At this point, it was unclear if the higher velocity peaks were caused directly by the increased jet angle, or if they were related to the increased mean velocities along the centerline of the free jet. This correlation could be tested by running higher jet velocities with a 30° angle until the mean centerline velocities of the free jet matched those from the 60° jets. Due to time constraints, this type of testing was not practical for the current investigation. Instead, a new non-dimensional parameter was created to incorporate a relationship between the magnitudes of the velocity spikes relative to the maximum mean velocity from the one-inch y-position in the domain. The non-dimensional parameter was called a "relative intensity," and was calculated by

$$RI = \frac{u}{u_{max\ (y=1")}} \qquad 5.1$$

where u represented the magnitude of a velocity peak, and u_{max} represented the maximum mean velocity from the transverse profile in Figure 5.10. Although Equation 5.1 resembled the calculation for turbulence intensity from chapter four, it differed in the sense that u was not a fluctuation and that u_{max} did not occur at the exact x-position where the time-dependent data were recorded. Nevertheless, the relative intensity at the one-inch downstream position was plotted for both the 30° and 60° jets (Figure 5.20 and Figure 5.21). The analysis consisted of counting the peaks of relative intensity that surpassed two reference values of 6 and 8. The relative intensity spiked over a value of 8 a total of 3 times for the 30° jets, but only twice for the 60° jets. Similarly, the relative intensity spiked over a value of 6 a total of 20 times for the 30° jets, but only 15 times for the 60° jets. In this case, the results indicated that the smaller jet angle produced higher fluctuations of velocity relative to the mean values. Although more data point would be required to determine a correlation between the jet angle and relative intensity, it seemed that the higher mean velocity in Figure 5.16 contributed more to the higher velocity spikes than the increased jet angle.

From the rough measurements of the velocity peak spacing, it seemed that velocity fluctuations occurred at higher frequencies for the 60° jets. At the one-inch downstream position for the 60° jets, the frequency was measured to be about 730 Hz, as opposed to 670 Hz for the 30° jets. Similarly, the peak frequencies at the three-inch downstream position were 240 Hz for the 60° model and 120 Hz for the 30° model. Neither the consistency of the data nor the method of analysis provided substantial

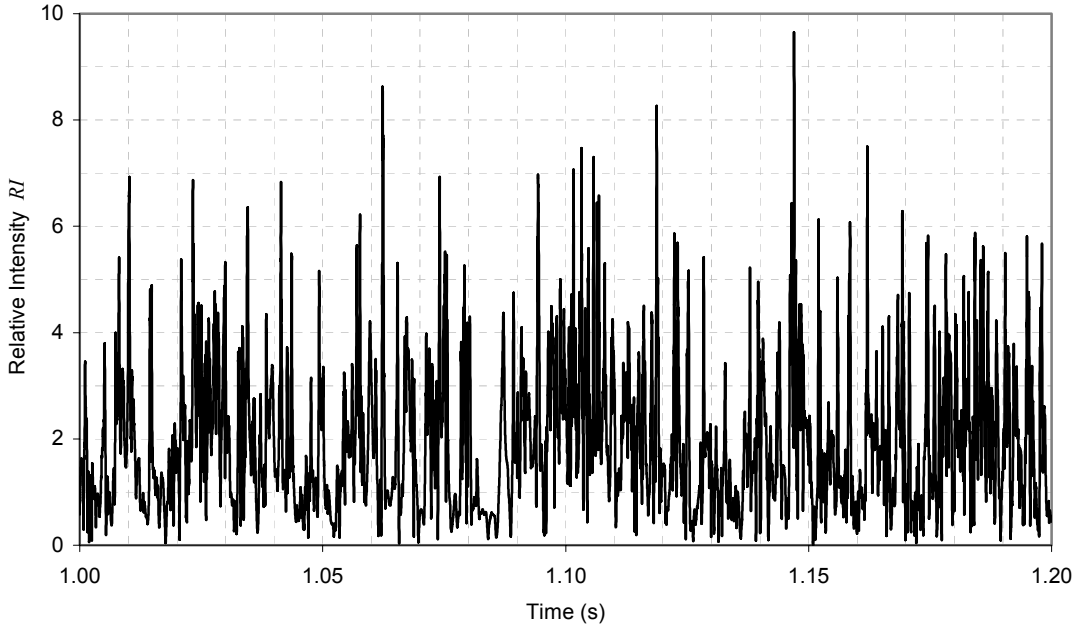


Figure 5.20 Time-dependent relative intensity at 2.54 cm (1") downstream of the channel exits for the 30° model, shown with 0.2 total seconds of run time.

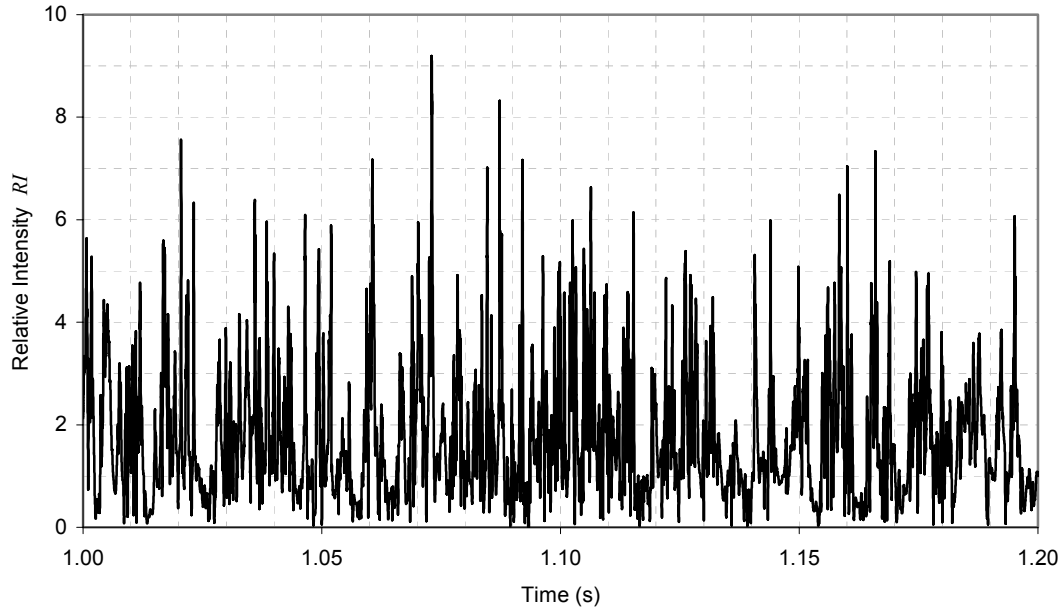


Figure 5.21 Time-dependent relative intensity at 2.54 cm (1") downstream of the channel exits for the 60° model, shown with 0.2 total seconds of run time.

quantitative conclusions. However, the comparisons indicated a positive relationship between the jet angle and the frequency of turbulent fluctuations. This relationship was tested again with the non-dimensional Strouhal number St given by

$$St = \frac{fd}{u_{max}} \qquad 5.2$$

where f was the frequency of velocity spikes, d was the y-distance from the die wall to the point monitor, and u_{max} was the maximum mean velocity from the transverse profile at each centerline position. At the one-inch downstream position, the Strouhal number was calculated to be about 1.3 for both jet angles. The values of St at the three-inch downstream position were 3.1 for the 60° model and 1.6 for the 30° model. The non-dimensional parameter indicated that the differences in fluctuation frequency at the one-inch position were insignificant. However, at the three-inch downstream position, the Strouhal number for the 60° jets was almost twice that of the 30° jets, which agreed with the previous frequency analysis. Several more data points would be necessary to make any quantitative conclusions; however, these results indicated a positive relationship between the jet angle and the frequency of velocity fluctuations beyond the one-inch downstream position.

CFD Comparison With Experimental Measurements

For the purpose of having comparable results between a numerical solution and experimental measurements, the plan originally involved running the experiment while matching the centerline velocity at a distance of 2.54 cm (1") downstream of the channel exits. For reasons unknown, the experimental data from this procedure were not available for the current investigation. Instead, experimental measurements were made using the designated geometry (Figure 4.20) with a similar but unmatched centerline velocity field. Both the numerical and experimental centerline velocity magnitudes were plotted together in Figure 5.22. Even though the velocity magnitudes were not matched at 2.54 cm, they were equal to each other at a downstream position of 1.78 cm. Since the position of 2.54 cm was chosen arbitrarily, there was no harm in using the matched position of 1.78 cm instead. In both the numerical solution and the experimental measurements, the centerline velocity was approximately 58 m/s at a downstream position of 1.78 cm. This value was used to nondimensionalize the plots of centerline velocity in Figure 5.23. The trend of the centerline velocity from the LES solution varied significantly from the experimental data, especially at further positions downstream. While the numerical results became questionable near the exit boundary, they still indicated a higher rate of velocity decay than the actual measurements for positions far upstream of the boundary. In Figures 5.24, 5.25, 5.26, and 5.27, velocity profiles from different positions along the centerline were normalized with respect to their maximum values. These figures indicated that the LES solution accurately predicted the width and

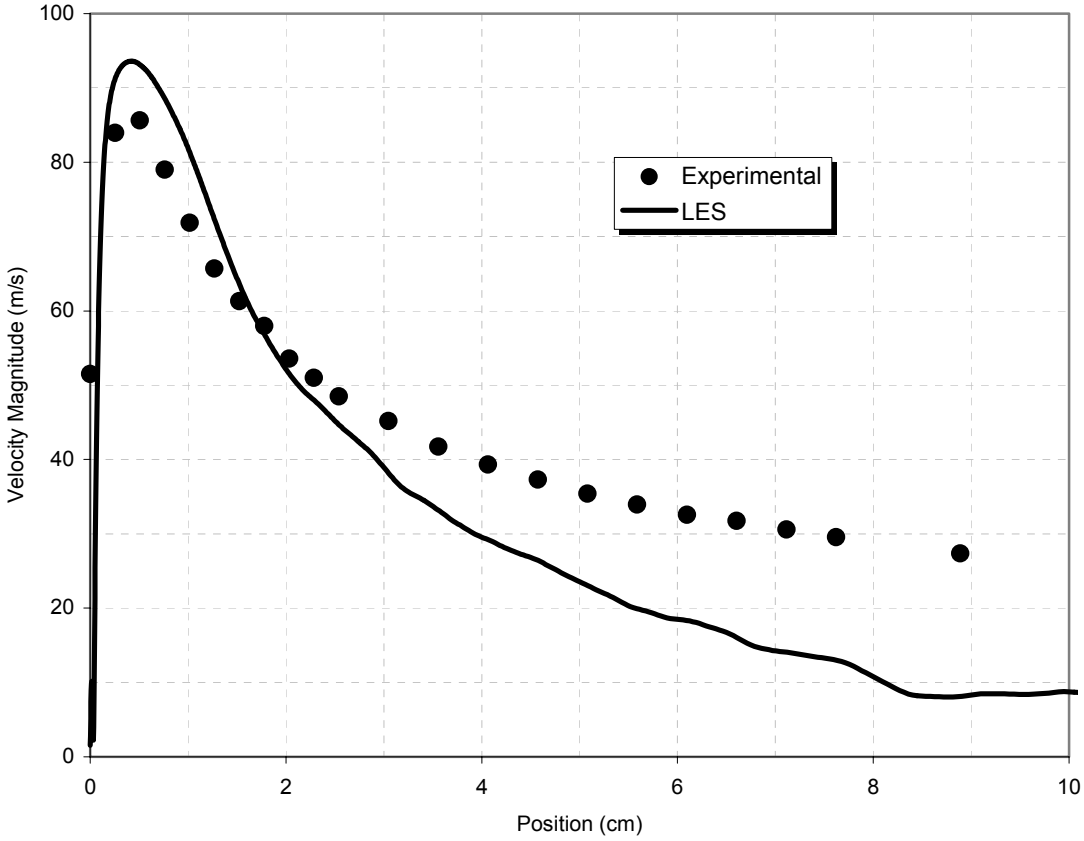


Figure 5.22 Comparison of centerline velocity between a time-averaged LES solution and experimental measurements. Matching velocities are located at 1.78 cm downstream of the channel exits.

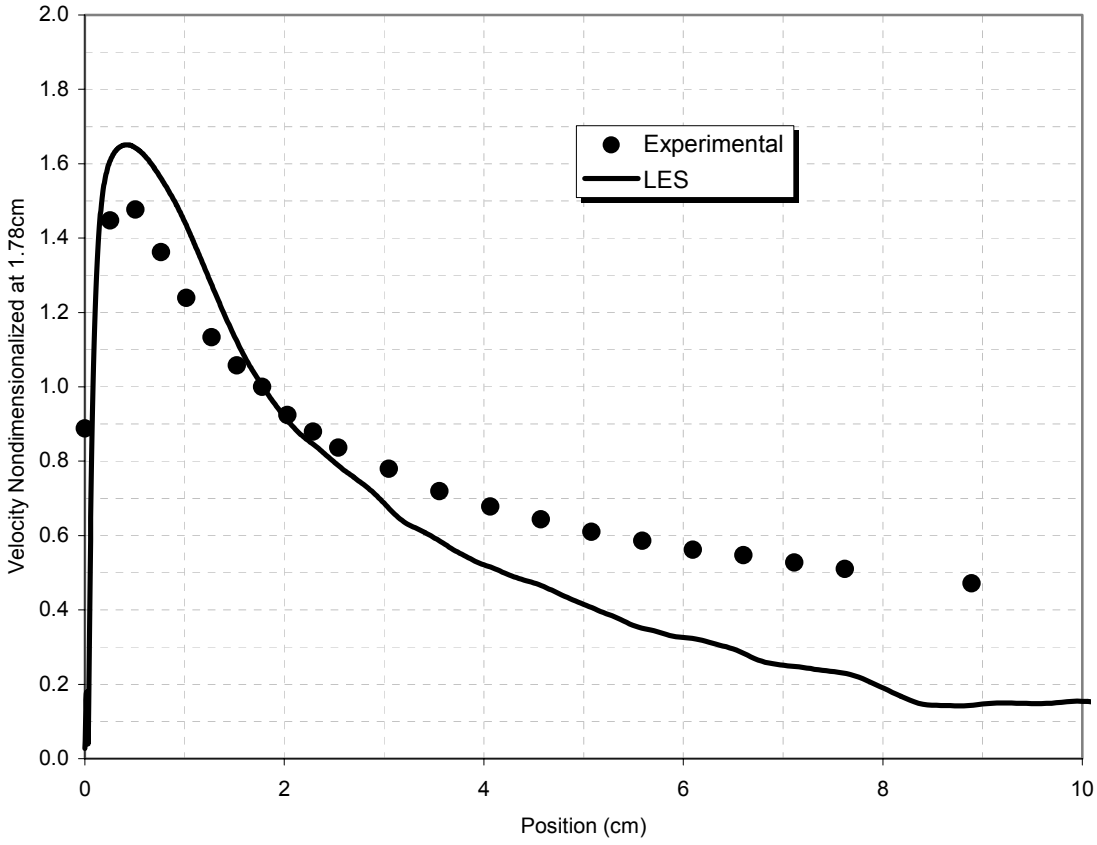


Figure 5.23 Comparison of centerline velocity between a time-averaged LES solution and experimental measurements. Velocities were non-dimensionalized with respect to the matching value of 58 m/s located at 1.78 cm in Figure 5.18.

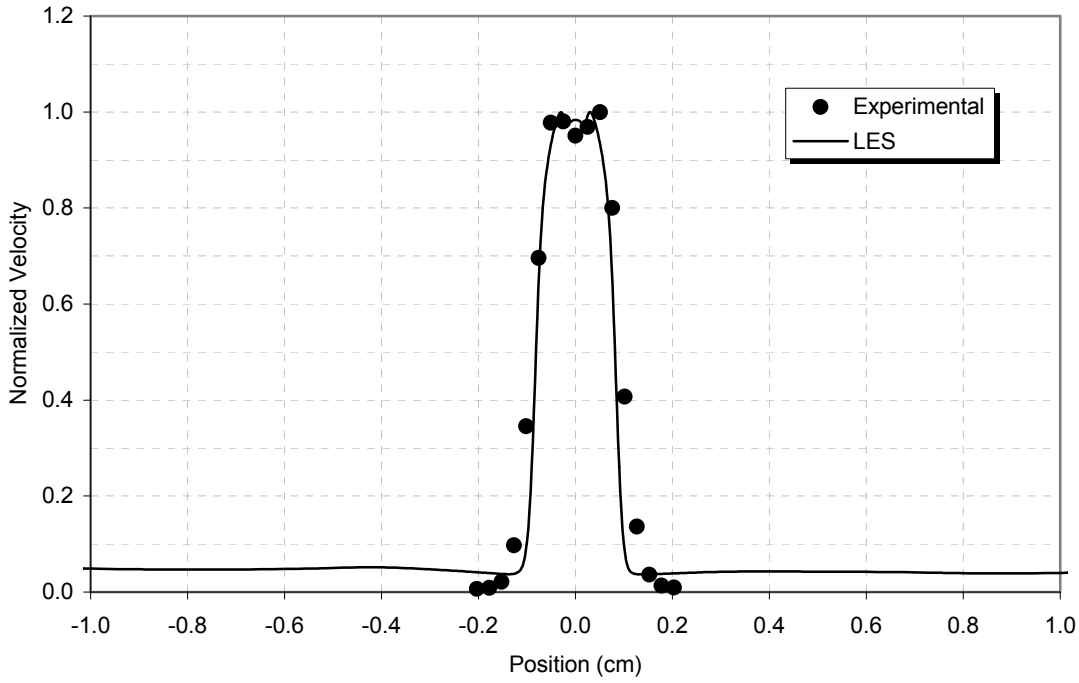


Figure 5.24 Comparison of velocity profiles in the 0.254 cm (0.1") downstream position, between a time-averaged LES solution and experimental measurements. Velocities were normalized with respect to their maximum values.

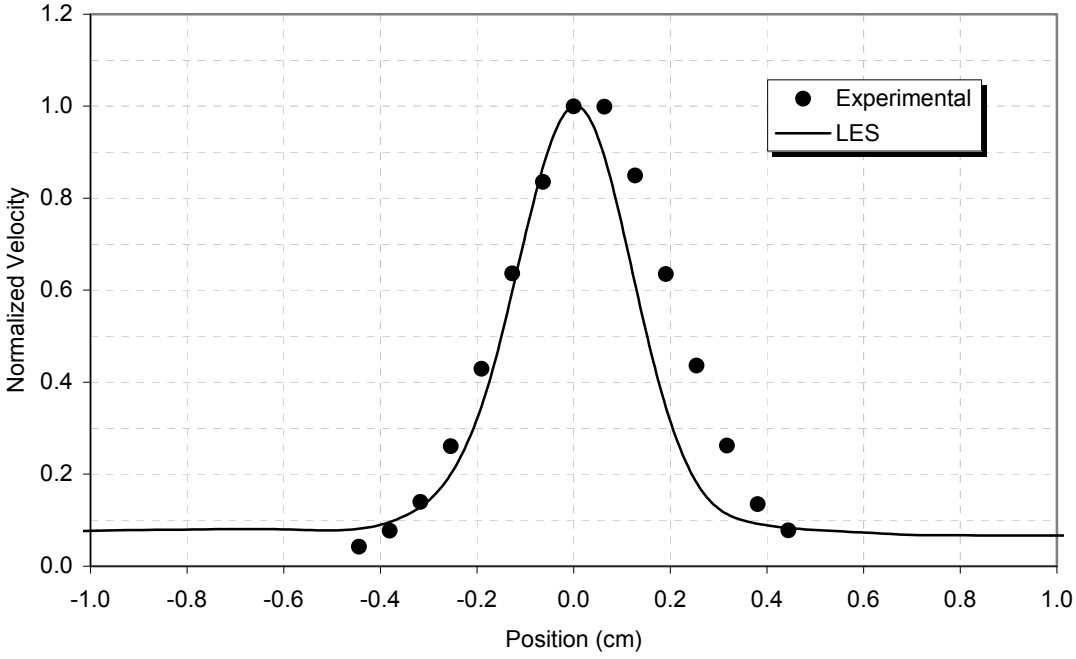


Figure 5.25 Comparison of velocity profiles in the 1.27 cm (0.5") downstream position, between a time-averaged LES solution and experimental measurements. Velocities were normalized with respect to their maximum values.

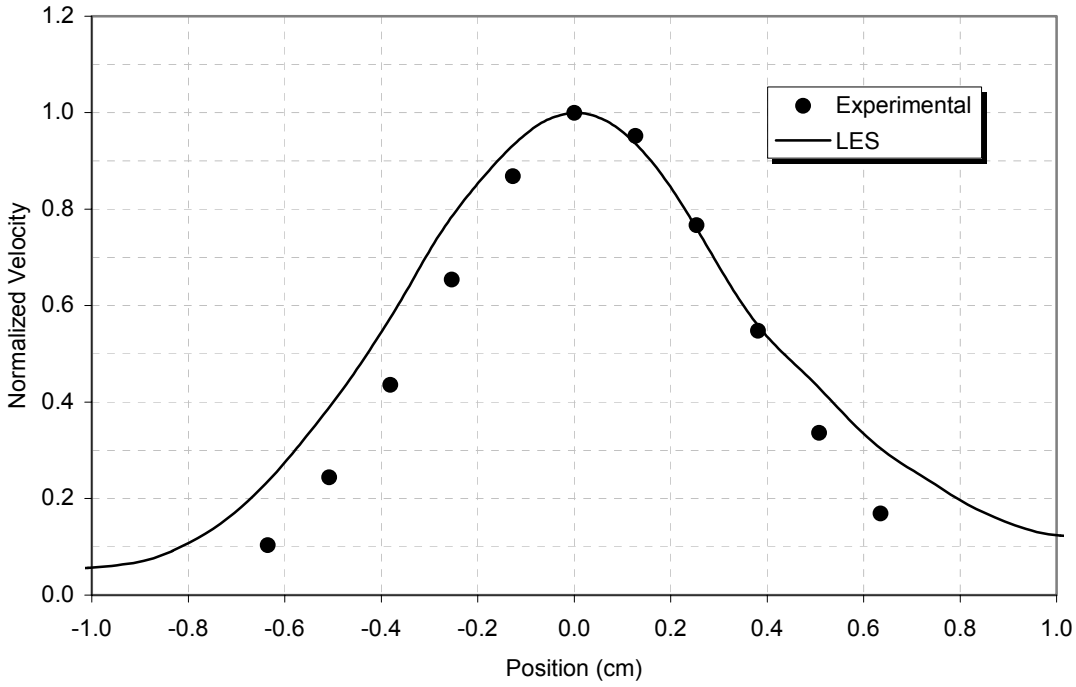


Figure 5.26 Comparison of velocity profiles in the 2.54 cm (1") downstream position, between a time-averaged LES solution and experimental measurements. Velocities were normalized with respect to their maximum values.

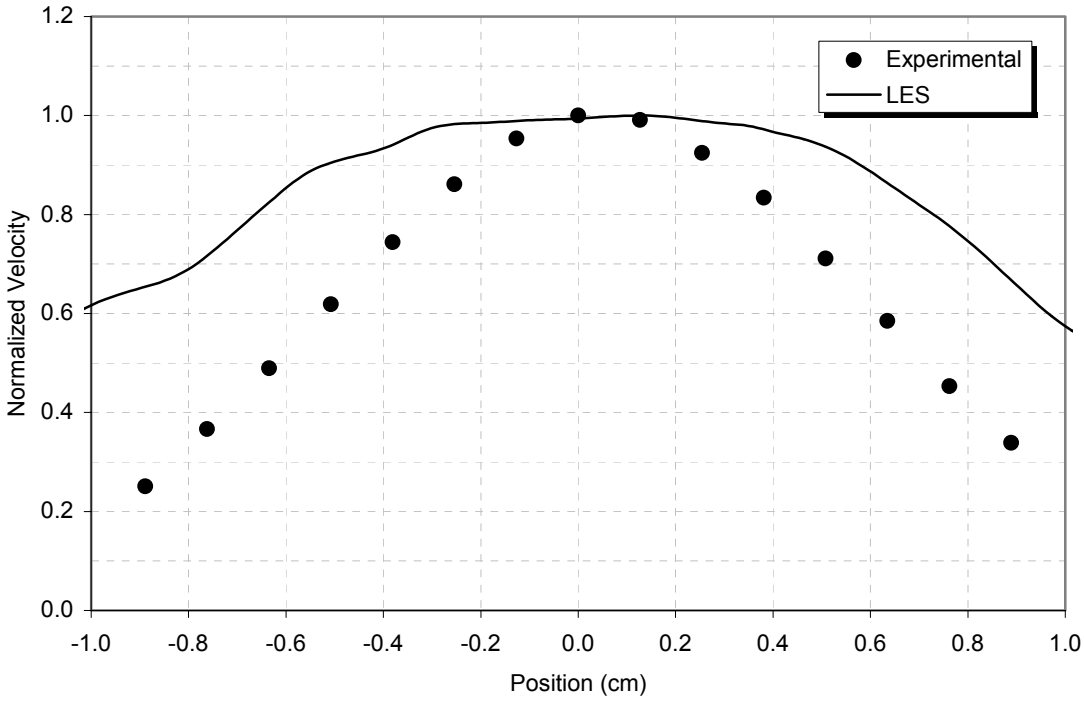


Figure 5.27 Comparison of velocity profiles in the 5.08 cm (2") downstream position, between a time-averaged LES solution and experimental measurements. Velocities were normalized with respect to their maximum values.

overall shape of the jet for positions close to the channel exit. However, the numerical solution predicted the flow to expand away from the centerline much sooner than was measured in the laboratory. This agreed with the rapid decay in the centerline velocity. It seemed that the CFD solution predicted more turbulent mixing, which made the jet set wider and its velocity decay quicker.

Animations of Velocity Contours

Additional post-processing capabilities were utilized in FLUENT, in which frames of velocity contours were saved at each time step. After the computations were complete, these frames were converted into animations using a separate software package. These movies provided a better understanding of how the vortex structures traveled throughout the flow domain.

Viewing an animation of the velocity contours indicated that the flow field was filled with unorganized, vortex structures moving in various directions. The vortices seemed to disperse from the centerline much earlier in the flow than anticipated. This accounted for the increased spreading rate of the jet and rapid decay in centerline velocity that was observed in the previous results. Another interesting observation from these movies was that most of the vortex structures traveled in pairs, appearing to influence each other as they moved downstream. However, when one of these paired vortices exited the boundary of the domain, the other vortex did not follow it. Instead, it traveled along the domain boundary, or in some cases, moved back towards the center of the

domain where it could influence other parts of the flow (Figure 5.28). Clearly, this was an error caused by limitations of boundary conditions. The lack of numerical information beyond the boundaries caused these vortex pairs to separate in an unrealistic manner.

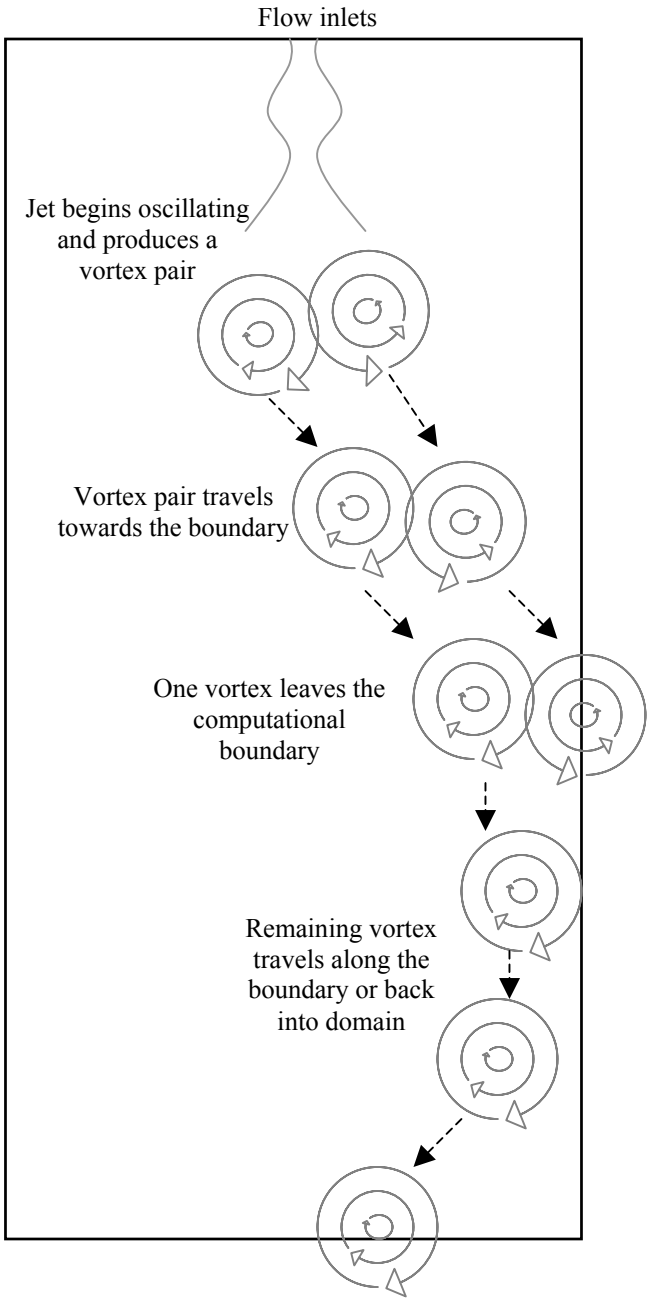


Figure 5.28 Schematic diagram of the flow domain illustrating the undesired impact that the boundary conditions have on vortex pairs, as observed in animations of the velocity contours.

CHAPTER VI

CONCLUSIONS AND RECOMMENDATIONS

Conclusions

The following conclusions are based upon the findings presented in this thesis.

1. When using a pressure inlet boundary, the LES model predicted a laminar velocity profile inside the air channels, even when the Reynolds number was well into the turbulent region. The k-epsilon turbulence model provided better results for this type of wall-bounded flow.
2. For the k-epsilon turbulence model, both the initialized flow field and computational domain size had a direct effect on the final solution. The initialized velocity field had the greatest influence on the final solution; however, this effect was minimized with larger computational domains.
3. For the k-epsilon solution inside the channel, a near-wall mesh refinement improved the calculation of shear forces at the walls, which resulted in a flattened velocity profile.
4. For the k-epsilon model, the amount of turbulence intensity at the pressure inlet boundary had no significant effect on the solution for the geometry studied.
5. The computational time for LES was reduced by initializing the flow field with a steady-state, k-epsilon solution.

6. According to the LES model with time-averaging statistics, the 60° jets produced a higher peak centerline velocity than the 30° jets.
7. The use of time-dependent point monitors along the centerline indicated that there was a positive relationship between the jet angle and the frequency of turbulent fluctuations beyond the one-inch downstream position.
8. The LES model predicted a mean flow field that compared well with experimental data in regions close to the die (less than 2-3 cm). However, the model became much less accurate further downstream. Overall, the LES model seemed to expand the jet profile away from the centerline much sooner than shown by experiments.
9. Many of the vortices traveled in pairs and seemed to influence each other throughout the flow domain.
10. Vortex pairs were separated by the pressure outlets due to the lack of numerical information beyond the exit boundaries. This was an unrealistic flow characteristic that resulted from the limitations of the boundary conditions.

Recommendations

The following studies are recommended in order to validate the findings in this thesis and to further the progression of modeling more complicated flows.

1. A thorough analysis should be performed using LES to model two-dimensional, turbulent channel flow. The investigation should explore the limitations of LES

through the use of different grid densities, boundary conditions, and channel geometries.

2. Through the use of parallel processing or supercomputing, the size of the computational domain should be increased drastically to quantify the errors imposed by the boundary conditions.
3. New investigations should include higher velocities and temperatures to study the effects of compressibility on the flow regime.
4. Advanced simulations should be performed to include the third spatial dimension, which is a typical standard for using LES.
5. A multiphase model should be set up to simulate the attenuation and solidification of molten fibers as they travel through turbulent flow.

LIST OF REFERENCES

[1] Krutka, H.M., Papavassiliou, D.V., and Shambaugh, R.L., "Analysis of a Melt-Blowing Die: Comparison of CFD and Experiments," Industrial and Engineering Chemistry Research, Vol. 41, No. 20, Oct. 2002, pp. 5125-5138.

[2] Utsman, F.M., An Experimental Investigation on the Production of Microfibers and the Web Defects Known as Shot for the Melt Blowing Process, Thesis, University of Tennessee, Knoxville, 1995.

[3] Krutka, H.M., Papavassiliou, D.V., and Shambaugh, R.L., "Effects of Die Geometry on the Flow Field of the Melt-Blowing Process," Industrial and Engineering Chemistry Research, Vol. 42, No. 22, Oct. 2003, pp. 5541-5553.

[4] Haynes, B.D., An Experimental and Analytical Investigation on the Production of Microfibers Using a Single Hole Melt Blowing Process, Ph. D. Dissertation, University of Tennessee, Knoxville, 1991.

[5] Hatcher, G.W., Computational Aerodynamic Analysis of Converging Free Jets, Thesis, University of Tennessee, Knoxville, 2004.

[6] Grald, E., "Performance Analysis of Melt-Blown Dies Using Computational Fluid Dynamics," 2nd INTC Conference, Baltimore, 2001.

[7] Sagaut, P., Large Eddy Simulation for Incompressible Flows: An Introduction, 3rd Edition, Springer, New York City, 2005.

[8] Moin, P., Pitsch, H., and Schluter, J., "Large Eddy Simulation Inflow Conditions for Coupling with Reynolds-Averaged Flow Solvers," AIAA Journal, Vol. 42, No. 3, Mar. 2004, pp. 478-484.

[9] Baritaud, T., Direct Numerical Simulation for Turbulent Reacting Flows, Editions Technip, Paris, 1996.

[10] Grinstein, F.F., "Introduction: Boundary Conditions for Large Eddy Simulation," AIAA Journal, Vol. 42, No. 3, Mar. 2004, p. 437.

[11] Grinstein, F.F., "Vortex Dynamics and Entrainment in Rectangular Free Jets," Journal of Fluid Mechanics, Vol. 437, June 2001, pp. 69-101.

[12] Shen, L., and Yue, D.K.P., "Large-Eddy Simulation of Free-Surface Turbulence," Journal of Fluid Mechanics, Vol. 440, Aug. 2001, pp. 75-116.

[13] Fureby, C., and Grinstein, F.F., "Monotonically Integrated Large Eddy Simulation of Free Shear Flows," AIAA Journal, Vol. 37, No. 5, May 1999, pp. 544-556.

[14] Hussaini, M.Y., Seiner, J.M., and Woodruff, S.L., "Grid-Size Dependence in the Large-Eddy Simulation of Kolmogorov Flow," AIAA Journal, Vol. 38, No. 4, Apr. 2000, pp. 600-604.

[15] Balaras, E., Piomelli, U., and Wallace, J.M., "Self-Similar States in Turbulent Mixing Layers," Journal of Fluid Mechanics, Vol. 446, Nov. 2001, pp. 1-24.

[16] Kunkel, G.J., Marusic, I., and Porte-Agel, F., "Experimental Study of Wall Boundary Conditions for Large-Eddy Simulation," Journal of Fluid Mechanics, Vol. 446, Nov. 2001, pp. 302-320.

[17] Alin, N., Fureby, C., and Wilkstrom, N., "Large-Eddy Simulation of High-Reynolds-Number Wall-Bounded Flows," AIAA Journal, Vol. 42, No. 3, Mar. 2004, pp. 457-468.

[18] Friedrich, R., Su, M.D., "Investigation of Fully Developed Turbulent Flow in a Straight Duct with Large Eddy Simulation," Journal of Fluids Engineering, Vol. 116, Dec. 1994, pp. 677-684.

[19] Bonnet, J.P., Druault, P., and Lardeau, S., "Generation of Three-Dimensional Turbulent Inlet Conditions for Large-Eddy Simulation," AIAA Journal, Vol. 42, No. 3, Mar. 2004, pp. 447-456.

[20] Garnier, E., Sagaut, P., and Tromeur, E., "Turbulent Inflow Conditions for Large-Eddy Simulation of Compressible Wall-Bounded Flows," AIAA Journal, Vol. 42, No. 3, Mar. 2004, pp. 469-477.

[21] Batten, P., Chakravarthy, S., and Goldberg, U., "Interfacing Statistical Turbulence Closures with Large-Eddy Simulation," AIAA Journal, Vol. 42, No. 3, Mar. 2004, pp. 485-492.

[22] "FLUENT 6.2 Users Guide", *www.fluentusers.com,* 2006.

[23] White, F.M., Viscous Fluid Flow, 2nd Edition, McGraw-Hill, Singapore, 1991.

[24] Lilly, D.K., "A Proposed Modification of the Germano Subgrid-Scale Closure Model," Physics of Fluids, Vol. 4, 1992, pp. 633-635.

[25] "Best Practices for Large Eddy Simulations (LES) in FLUENT," *www.fluentusers.com*, 2006.

APPENDIX A

BATCH MODE COMMANDS

When a model required a large number of computational iterations, FLUENT was executed in a batch or background mode. This feature allowed FLUENT commands to be executed via journal files and a calculation history to be reported with an output file. Typically, all of the problem setup, initial calculations, and post-processing commands were performed interactively with the graphical user interface. The journal files were used only to initiate and to terminate the computational iterations.

Batch execution command line

```
jhaynes@par:~> /sw/Fluent.6.2/bin/fluent 2ddp -g < journal.txt >&
               output.txt &
```

Example content of a journal.txt file

```
file
read-case-data
les30
q

file
auto-save
case-frequency
1000
data-frequency
1000
root-name
les30_
q
q

solve
dual-time-iterate
20000
50
q

exit
```

APPENDIX B

VELOCITY PROFILE DATA

User-defined velocity profiles were imported into FLUENT in order to specify a velocity magnitude for each cell of a velocity inlet boundary. FLUENT required an x-coordinate and y-coordinate to be specified for each velocity magnitude. This information was imported through a ".prof" file. The data were entered using SI units (m, m/s).

Left inlet

```
((inlet-left point 36)
(x
-0.000572978
-0.000568705
-0.000564431
-0.000560158
-0.000555884
-0.000551611
-0.000547337
-0.000543063
-0.000536653
-0.000528106
-0.000519559
-0.000511012
-0.000498191
-0.000481097
-0.000464003
-0.000446909
-0.000429814
-0.00041272
-0.000395626
-0.000378532
-0.000361438
-0.000344343
-0.000327249
-0.000310155
-0.000297334
-0.000288787
-0.00028024
-0.000271693
-0.000265283
-0.000261009
-0.000256736
-0.000252462
```

```
-0.000248188
-0.000243915
-0.000239641
-0.000235368
)

(y
0.000159474
0.000159474
0.000159474
0.000159474
0.000159474
0.000159474
0.000159474
0.000159474
0.000159474
0.000159474
0.000159474
0.000159474
0.000159474
0.000159474
0.000159474
0.000159474
0.000159474
0.000159474
0.000159474
0.000159474
0.000159474
0.000159474
0.000159474
0.000159474
0.000159474
0.000159474
0.000159474
0.000159474
0.000159474
0.000159474
0.000159474
0.000159474
0.000159474
0.000159474
0.000159474
0.000159474
0.000159474
0.000159474
0.000159474
0.000159474
0.000159474
0.000159474
0.000159474
0.000159474
0.000159474
0.000159474
0.000159474
0.000159474
0.000159474
0.000159474
0.000159474
0.000159474
)

(left-vel-mag
5.2408719
15.50524
25.363516
34.423157
42.281719
48.759487
53.97374
58.148376
63.073925
67.897652
71.468819
74.193962
77.304367
80.102974
81.926659
```

```
83.070786
83.717552
83.992668
83.992668
83.717552
83.070786
81.926659
80.102974
77.304367
74.193962
71.468819
67.897652
63.073925
58.148376
53.97374
48.759487
42.281719
34.423157
25.363516
15.50524
5.2408719
)
)
```

Right inlet

```
((inlet-right point 36)

(x
0.000235368
0.000239641
0.000243915
0.000248188
0.000252462
0.000256736
0.000261009
0.000265283
0.000271693
0.00028024
0.000288787
0.000297334
0.000310155
0.000327249
0.000344343
0.000361438
0.000378532
0.000395626
0.00041272
0.000429814
0.000446909
0.000464003
0.000481097
0.000498191
0.000511012
0.000519559
0.000528106
0.000536653
0.000543063
```

```
0.000547337
0.000551611
0.000555884
0.000560158
0.000564431
0.000568705
0.000572978
)

(y
0.000159474
0.000159474
0.000159474
0.000159474
0.000159474
0.000159474
0.000159474
0.000159474
0.000159474
0.000159474
0.000159474
0.000159474
0.000159474
0.000159474
0.000159474
0.000159474
0.000159474
0.000159474
0.000159474
0.000159474
0.000159474
0.000159474
0.000159474
0.000159474
0.000159474
0.000159474
0.000159474
0.000159474
0.000159474
0.000159474
0.000159474
0.000159474
0.000159474
0.000159474
0.000159474
0.000159474
)

(right-vel-mag
5.2408719
15.50524
25.363516
34.423157
42.281719
48.759487
53.97374
58.148376
63.073925
67.897652
71.468819
74.193962
```

```
77.304367
80.102974
81.926659
83.070786
83.717552
83.992668
83.992668
83.717552
83.070786
81.926659
80.102974
77.304367
74.193962
71.468819
67.897652
63.073925
58.148376
53.97374
48.759487
42.281719
34.423157
25.363516
15.50524
5.2408719
)
)
```

VITA

Jared Michael Haynes was born in Johnson City, Tennessee on February 14, 1980. He grew up in Jefferson County and graduated from Jefferson County High School in 1998. In August that same year, he entered the University of Tennessee, Knoxville, to study Aerospace Engineering. During his undergraduate career, Mr. Haynes worked as an engineering intern at the Arnold Engineering Development Center (AEDC) over the course of four years. In May of 2004, he received dual Bachelor of Science degrees in Aerospace Engineering and Mechanical Engineering. Before entering postgraduate studies at the University of Tennessee, Knoxville, he married the former Miss Rebecca Christine Evans in Sparta, Tennessee. In August of 2006, Jared received his Master of Science degree in Aerospace Engineering from the University of Tennessee, Knoxville.